

Magnetically levitated planar actuator with moving magnets

Citation for published version (APA):

Lierop, van, C. M. M. (2008). *Magnetically levitated planar actuator with moving magnets*. [Phd Thesis 1 (Research TU/e / Graduation TU/e), Electrical Engineering]. Technische Universiteit Eindhoven.
<https://doi.org/10.6100/IR631971>

DOI:

[10.6100/IR631971](https://doi.org/10.6100/IR631971)

Document status and date:

Published: 01/01/2008

Document Version:

Publisher's PDF, also known as Version of Record (includes final page, issue and volume numbers)

Please check the document version of this publication:

- A submitted manuscript is the version of the article upon submission and before peer-review. There can be important differences between the submitted version and the official published version of record. People interested in the research are advised to contact the author for the final version of the publication, or visit the DOI to the publisher's website.
- The final author version and the galley proof are versions of the publication after peer review.
- The final published version features the final layout of the paper including the volume, issue and page numbers.

[Link to publication](#)

General rights

Copyright and moral rights for the publications made accessible in the public portal are retained by the authors and/or other copyright owners and it is a condition of accessing publications that users recognise and abide by the legal requirements associated with these rights.

- Users may download and print one copy of any publication from the public portal for the purpose of private study or research.
- You may not further distribute the material or use it for any profit-making activity or commercial gain
- You may freely distribute the URL identifying the publication in the public portal.

If the publication is distributed under the terms of Article 25fa of the Dutch Copyright Act, indicated by the "Taverne" license above, please follow below link for the End User Agreement:

www.tue.nl/taverne

Take down policy

If you believe that this document breaches copyright please contact us at:

openaccess@tue.nl

providing details and we will investigate your claim.

Magnetically levitated planar actuator with moving magnets: Dynamics, commutation and control design

PROEFSCHRIFT

ter verkrijging van de graad van doctor aan de
Technische Universiteit Eindhoven, op gezag van de
Rector Magnificus, prof.dr.ir. C.J. van Duijn, voor een
commissie aangewezen door het College voor
Promoties in het openbaar te verdedigen
op dinsdag 15 januari 2008 om 16.00 uur

door

Cornelis Martinus Maria van Lierop

geboren te Eindhoven

Dit proefschrift is goedgekeurd door de promotoren:

prof.dr.ir. P.P.J. van den Bosch

en

prof.dr.ir. A.J.A. Vandenput

Copromotor:

dr.ir. A.A.H. Damen



This work is part of the IOP-EMVT program (Innovatiegerichte onderzoeksprogramma's - Elektromagnetische vermogenstechniek). This program is funded by SenterNovem, an agency of the Dutch Ministry of Economic Affairs.



This dissertation has been completed in fulfillment of the requirements of the Dutch Institute of Systems and Control DISC.

Copyright ©2008 by C.M.M. van Lierop

Coverdesign by AtelJ van Lierop Bladel and Studio Interpoint Netersel

CIP-DATA LIBRARY TECHNISCHE UNIVERSITEIT EINDHOVEN

Lierop, Cornelis M.M. van

Magnetically levitated planar actuator with moving magnets : dynamics, commutation and control design / by Cornelis Martinus Maria van Lierop. - Eindhoven : Technische Universiteit Eindhoven, 2008.

Proefschrift. - ISBN 978-90-386-1704-6

NUR 959

Trefw.: magnetische levitatie / elektrische machines ; regelingen / lineaire elektromotoren / elektrische aandrijvingen ; regelen.

Subject headings: commutation / magnetic levitation / machine control / linear motors.

Aan Chantal, Els, John en Willem

Abstract

Magnetically levitated planar actuator with moving magnets: Dynamics, commutation and control design

Mechanical systems with multiple degrees of freedom typically consist of several one degree-of-freedom electromechanical actuators. Most of these electromechanical actuators have a standard, often integrated, commutation (i.e. linearization and decoupling) algorithm deriving the actuator inputs which result in convenient control properties and relatively simple actuator constraints. Instead of using several one degree-of-freedom actuators, it is sometimes advantageous to combine multiple degrees of freedom in one actuator to meet the ever more demanding performance specifications. Due to the integration of the degrees of freedom, the resulting commutation and control algorithms are more complex. Therefore, the involvement of control engineering during an early stage of the design phase of this class of actuators is of paramount importance. One of the main contributions of this thesis is a novel commutation algorithm for multiple degree-of-freedom actuators and the analysis of its design implications.

A magnetically levitated planar actuator is an example of a multiple degree of freedom electromechanical actuator. This is an alternative to xy -drives, which are constructed of stacked linear motors, in high-precision industrial applications. The translator of these planar actuators is suspended above the stator with no support other than magnetic fields. Because of the active magnetic bearing the translator needs to be controlled in all six mechanical degrees of freedom. This thesis presents the dynamics, commutation and control design of a contactless, magnetically levitated, planar actuator with moving magnets. The planar actuator consists of a stationary coil array, above which a translator consisting of an array of permanent magnets is levitated. The main advantage of this actuator is that no cables from

the stator to the translator are required. Only coils below the surface of the magnet array effectively contribute to its levitation and propulsion. Therefore, the set of active coils is switched depending on the position of the translator in the xy -plane. The switching in combination with the contactless translator, in principle, allows for infinite stroke in the xy -plane.

A model-based commutation and control approach is used throughout this thesis using a real-time analytical model of the ironless planar actuator. The real-time model is based on the analytical solutions to the Lorentz force and torque integrals. Due to the integration of propulsion in the xy -plane with an active magnetic bearing, standard decoupling schemes for synchronous machines cannot be applied to the planar actuator to linearize and decouple the force and the torque components. Therefore, a novel commutation algorithm has been derived which inverts the fully analytical mapping of the force and torque exerted by the set of active coils as a function of the coil currents and the position and orientation of the translator. Additionally, the developed commutation algorithm presents an optimal solution in the sense that it guarantees minimal dissipation of energy. Another important contribution of this thesis is the introduction of smooth position dependent weighing functions in the commutation algorithm. These functions enable smooth switching between different active coil sets, enabling, in principle, an unlimited stroke in the xy -plane. The resulting current waveform through each individually excited active coil is non-sinusoidal.

The model-based approach, in combination with the novel commutation algorithm, resulted in a method to evaluate/design controllable topologies. Using this method several stator coil topologies are discussed in this thesis. Due to the changing amount of active coils when switching between active coil sets, the actuator constraints (i.e. performance) depend on the xy -position of the translator. An analysis of the achievable acceleration as a function of the position of the translator and the current amplifier constraints is given. Moreover, the dynamical behavior of the decoupled system is analyzed for small errors and a stabilizing control structure has been derived.

One of the derived coil topologies called the Herringbone Pattern Planar Actuator (HPPA) has been analyzed into more detail and it has been manufactured. The stator of the actuator consists of a total of 84 coils, of which between 15 and 24 coils are simultaneously used for the propulsion and levitation of the translator. The real-time model, the dynamic behavior and the commutation algorithm have been experimentally verified using this fully-operational actuator. The 6-DOF contactless, magnetically levitated, planar actuator with moving magnets (HPPA) has been designed and tested and is now operating successfully according to all initial design and performance specifications.

Contents

1	Introduction	1
1.1	Background	2
1.2	Research objectives	4
1.3	Organization of the thesis	5
2	Commutation of basic forcer topologies using $dq0$ transformation	7
2.1	Introduction	7
2.2	Rotating machines	8
2.3	Linear actuators	12
2.4	Basic forcer topologies for planar motion	16
3	Linearization and decoupling of the wrench	21
3.1	Introduction	21
3.2	Real-time analytical six degree-of-freedom coil model	22
3.3	Direct wrench-current decoupling	29
3.3.1	Switching	32
3.4	Force and torque decomposition	45
4	Design of controllable topologies	49
4.1	Introduction	49
4.2	State controllability conditions of a planar actuator	49
4.3	Error sensitivity of weighted minimal norm inverses and solutions	53
4.4	Controllable 6 DOF basic topologies	55
4.5	Worst-case force components	62
5	Experiments	67
5.1	Introduction	67

5.2	Experimental setup	67
5.2.1	HPPA prototype	67
5.2.2	Test bench	68
5.3	Control structure	76
5.4	Measurement results	82
5.4.1	Closed-loop identification	82
5.4.2	Tracking performance	89
6	Conclusions and recommendations	95
6.1	Model based commutation algorithm	95
6.2	Linking control to the design proces	96
6.3	Realization and test of the prototype	96
6.4	Outlook towards future developments	97
6.4.1	Full rotation about the z-axis	97
6.4.2	Planar actuators with non-holonomic constraints	97
6.4.3	Fault tolerant planar actuator commutation	97
6.4.4	Wireless power transfer, data communication and control	97
6.4.5	Multiple translators above one stator	98
A	Schur complement	99
B	Proof of theorem 4.7	101
C	List of symbols	103
	Bibliography	105
	Samenvatting - Dutch abstract	111
	Dankwoord - Acknowledgements	115
	Curriculum Vitae	117

Chapter 1

Introduction

The field of control engineering is often only involved at the final stage of a project. This can sometimes lead to problems when the design is not optimal with respect to the control objectives which are necessary for obtaining the desired functionality. The design of electromechanical machines is no exception to this observation since they are often designed first and the control issues are dealt with later. To be able to control the machine, often a non-linear decoupling called the $dq0$ - or Park's transformation [33, 34] is applied to linearize the machine properties which are necessary for control. This commutation method works fine for most electrical machines because the non-linear mapping has very convenient properties like orthonormality and power invariance. Moreover, most electromechanical machines only actuate a single degree-of-freedom. However, when more mechanical degrees-of-freedom (DOF) are combined in the electromechanical design of the actuator, the sequential approach described above is not valid anymore. Due to the multiple degrees-of-freedom, concepts like directionality, linearization by feedback, controllability, and the resulting complex actuator constraints start to play a major role in the design process. Moreover, in some cases even the traditional $dq0$ -transformation cannot be applied effectively. Consequently, the traditional assumptions about control which are made during the design phase of the machine do not hold anymore, resulting in the need for a larger involvement of control engineering aspects during the design process. This thesis focusses on the design aspects of planar actuators with integrated magnetic bearing related to the controllability. Nevertheless, the theory derived is not limited to this class of actuators. The planar actuators discussed in this thesis consist of a translator with permanent magnets which is levitated above

an array of coils. The translator has an, in principle, unlimited stroke in the horizontal plane.

The main focus is on how to obtain a suitable commutation algorithm which both exploits the possibilities of the actuator as well as obtaining an implementable control solution. In order to achieve better understanding of the mechanisms involved in creating a planar actuator and its controller, a model based approach is used.

1.1 Background

Accurate positioning of objects in a plane is required in many industrial apparatus, e.g. semiconductor lithography scanners, pick-and-place machines and inspection systems. Usually, these multi-degree-of-freedom (DOF) positioning systems are constructed of stacked long- and short-stroke single-degree-of-freedom linear and rotary drives, which are supported by roller or air bearings. Instead of stacking one-degree-of-freedom drives, multiple degrees-of-freedom can be combined in one actuator. Consequently, the moving mass and, therefore, the necessary force levels to obtain the required acceleration, can be reduced. An example of such a drive is a planar actuator, which has a single translator that can be levitated and can move in the xy -plane over the stator surface (figures 1.1 and 1.2).

In recent years, planar actuators became of interest to the semiconductor industry, which is constantly striving for smaller devices, which contain more functionality for a lower price. A shorter wavelength of the light, which is used in the lithographical steps, allows for smaller features on the chips. Currently, lithography systems are developed and tested which have an extreme-ultraviolet light source. To prevent contamination of optical elements and absorption of the extreme-ultraviolet light by air, the wafers (silicon substrates) are exposed in a high-vacuum environment [27]. To accurately position the wafers in vacuum, magnetically levitated planar drives have been studied [28, 4, 5, 15, 30, 6]. Because of the magnetic bearing, the vacuum is not contaminated by lubricants and there is no mechanical wear. The planar actuators have a planar coil array and a planar magnet array. As any permanent-magnet machine, planar actuators can be constructed in two ways. They have either moving coils and stationary magnets, or moving magnets and stationary coils. Figures 1.1 and 1.2 show artists impressions of these two respective actuator types. Although only a two degree-of-freedom planar motion is desired, these actuators need to be controlled in six degree-of-freedom to obtain a stable active magnetic bearing (stabilizing the three rotations and the levitation). Contrary to other magnetically levitated systems, such as active magnetic bearings for rotary

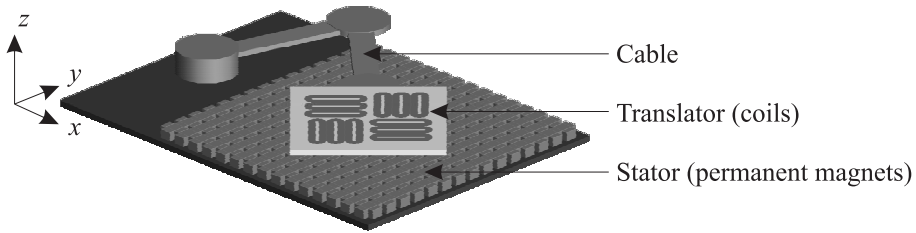


Figure 1.1. *Moving-coil planar actuator.*

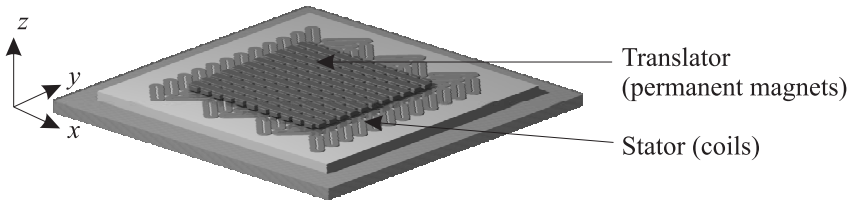


Figure 1.2. *Moving-magnet planar actuator.*

machine shafts and magnetically levitated trains, there is no physical decoupling of the levitation and the propulsion functions. These functions are controlled by the same coils and magnets, therefore, these planar actuators can be considered as a special class of multi-phase synchronous permanent-magnet motors.

The main advantage of a moving-coil planar actuator over a moving-magnet planar actuator is that less coils, and their amplifiers, are needed because the stroke in the xy -plane can be simply increased by adding extra magnets to the magnet array. Moreover, design constraints can be derived which allow for control of the torque exerted on the translator using the $dq0$ -transformation [4]. A clear disadvantage of the moving-coil planar actuator is that the coils need power and cooling which require a cable slab to the translator.

A big advantage of the moving-magnet configuration is that there is no contact between the translator and the fixed world because no cable to the moving part is necessary, since the coils, which require power and cooling, are on the stationary part of the actuator. This drastically reduces the amount of disturbances to the

translator. A disadvantage of the moving-magnet planar actuator, however, is the increased complexity of the torque decoupling as a function of position. Various proposals to control the moving-magnet torque using the $dq0$ -decomposition have been made in patent literature [41, 40, 1, 2]. However, the resulting disturbance torque remains significant. Moreover, in a moving-magnet planar actuator, only the coils below and near the edges of the magnet array can exert force and torque on the magnet array. Therefore, when long-stroke motion in the xy -plane is desired, the set of active coils has to be switched. No literature on the design and control aspects of switching the set of active coils, without influencing the force and torque decoupling, has been found.

1.2 Research objectives

Using traditional synchronous electrical machine theory to design/control long-stroke moving-magnet planar actuators with integrated magnetic bearing does not lead to practical results (see section 1.1). However, this class of actuators has the advantage of contactless levitation and propulsion, resulting in small translator disturbances. Therefore, the need for new electromechanical design and control theories arises to study and design this class of actuators. Consequently, research into obtaining both an efficient as well as a real-time controllable electromechanical design calls for the combination of the electromechanical design and control disciplines. The research into the control and electromechanical design aspects has, therefore, been carried out in parallel by two PhD students and the results are described in two theses. This thesis focusses on the commutation, the controllability of planar actuator designs and the control of the realized planar actuator, whereas the thesis of Jansen [17] focusses on the modeling and design of the planar actuator. To validate the derived theory, and to assure that all critical design aspects are covered, a proof-of-principle device has been created. The general project objectives discussed in this thesis, therefore, can be summarized by the following three sub-objectives:

- Research of model-based commutation algorithms which linearize and decouple the system. Due to the nature of long-stroke moving-magnet planar actuators the classical machine theory which is used to derive a suitable commutation algorithm cannot be applied effectively. The main reasons creating this problem are the larger influence of the "disturbance" torque when using sinusoidal currents and the need to switch active coil sets when long-stroke movement is applied. (chapters 2 and 3)
- Research the link between the commutation algorithm and the design pro-

cess. Since the commutation algorithms need to be both fast and accurate, the complexity of the (real-time) model and the commutation algorithm needs to be low but still sufficiently accurate to represent the system behavior. Moreover, the desired motion-profiles, the influence of the location of the mass-center-point and the noise-distribution over the degrees-of-freedom also play an important role in both the electromechanical as well as the control design. (chapters 3 and 4)

- Research the effectiveness of the derived theory by using a proof-of-principle device. Because of the large amount of parameters in combination with the non-linear behavior of the system, a proof-of-principle device is realized to validate the models and the decoupling algorithm. (chapter 5)

1.3 Organization of the thesis

Although the work presented in this thesis heavily depends on the theory derived in [17] it can be read independently. Consequently, there are some overlapping parts.

Chapter 2 focusses on the $dq0$ - or Park's transformation which is traditionally used to decouple and control synchronous actuators. The transformation is adapted to create basic planar forcer topologies (a stator-coil layout which can be used to produce position independent forces). These forcer topologies are the building blocks of the examples which are used throughout this thesis. A new direct wrench-current decoupling algorithm is derived in chapter 3 (where the wrench is defined as a vector which consists of both force and torque components). Using this new algorithm it is possible to decouple the force and torque components of ironless moving-magnet planar actuators with integrated magnetic bearing. Only coils below the magnet array effectively contribute to the levitation and propulsion of the translator. Therefore, the decoupling algorithm is adapted to include switching between active coil sets enabling the design and control of long-stroke actuators. Furthermore, conditions are derived which have to be met for decoupling to function. At the end of this chapter it is shown that, in the case of ironless planar actuators, the $dq0$ transformation can be seen as a subclass of the new commutation strategy. Chapter 4 focusses on how to design controllable topologies, using the derived commutation algorithm of chapter 3. The theory discussed throughout both this thesis as well as the thesis of Jansen [17] has been used to create a fully functioning prototype called the Herringbone Pattern Planar Actuator (HPPA). Measurements on the controlled HPPA are presented in chapter 5. Conclusions and recommendations for future work are given in chapter 6.

Chapter 2

Commutation of basic forcer topologies using $dq0$ transformation

2.1 Introduction

Generally, an electromechanical actuator can be described using non-linear differential equations. There are, however, methods to simplify the dynamical system. Figure 2.1 shows a simplification which is often used. The actuator model is simpli-

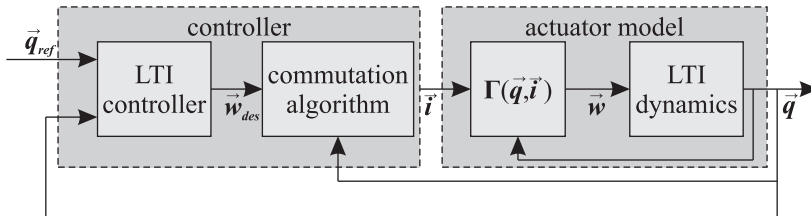


Figure 2.1. Basic control configuration.

fied by splitting it into two parts. The first non-linear part $\Gamma(\vec{q}, \vec{i})$ maps the current vector \vec{i} , containing the currents through each coil, and the position and/or orientation vector of the translator/rotor \vec{q} onto the wrench vector \vec{w} (which is a vector containing force and/or torque components). When hysteresis effects are neglected the mapping can usually be considered memoryless. The second part contains the LTI (Linear-Time-Invariant) dynamics of the actuator. The main challenge in controlling these actuators lies in finding a suitable inverse mapping or commutation

algorithm which linearizes and decouples the system by feedback. Classically, for most rotating (and linear) actuators this inverse mapping is achieved using the $dq0$ or Park's transformation which will be discussed in more detail in sections 2.2 and 2.3. Section 2.4 shows how (parts of) the $dq0$ transformation can be expanded towards planar actuators. Moreover, section 2.4 also shows some basic coil configurations which can be used as building blocks for planar actuators.

2.2 Rotating machines

Classically the $dq0$ transformation was derived for rotating machines. However, the theory is not restricted to this class of machines. In order to understand the adapted versions of the $dq0$ transformation this section summarizes the classical theory applied to permanent-magnet synchronous machines.

Figure 2.2 shows a schematic representation of an idealized rotating three-phase synchronous permanent-magnet machine. The flux-linkage vector ${}^{abc}\vec{\lambda}$ is

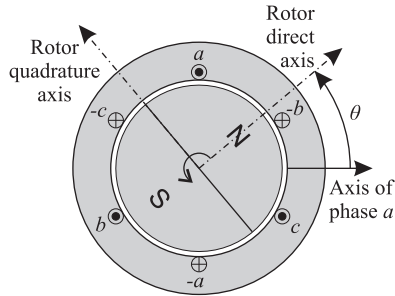


Figure 2.2. Schematic representation of an ideal two-pole three-phase synchronous permanent-magnet machine.

given by

$${}^{abc}\vec{\lambda} = {}^{abc}\mathbf{L}(\theta_e) {}^{abc}\vec{i} + {}^{abc}\vec{\lambda}_{pm}(\theta_e), \quad (2.1)$$

where ${}^{abc}\vec{i} = [i_a \ i_b \ i_c]^\top$ is the current-vector and the superscript abc is used to indicate that the vector contains the three stator phase quantities,

$${}^{abc}\vec{\lambda}_{pm}(\theta_e) = \lambda_{pm} \begin{bmatrix} \cos(\theta_e) \\ \cos(\theta_e - \frac{2}{3}\pi) \\ \cos(\theta_e + \frac{2}{3}\pi) \end{bmatrix}, \quad (2.2)$$

is the permanent-magnet flux-linkage vector (the magnets are modeled as ideal flux sources) and

$${}^{abc}\mathbf{L}(\theta_e) = \begin{bmatrix} L_{aa}(\theta_e) & L_{ab}(\theta_e) & L_{ac}(\theta_e) \\ L_{ba}(\theta_e) & L_{bb}(\theta_e) & L_{bc}(\theta_e) \\ L_{ca}(\theta_e) & L_{cb}(\theta_e) & L_{cc}(\theta_e) \end{bmatrix}, \quad (2.3)$$

is the matrix containing the self and mutual inductances of the stator coils. Ideally, the self and mutual inductances can be written as,

$$\begin{aligned} L_{aa} &= L_{self} + L_{salient} \cos(2\theta_e), \\ L_{bb} &= L_{self} + L_{salient} \cos\left(2\theta_e + \frac{2}{3}\pi\right), \\ L_{cc} &= L_{self} + L_{salient} \cos\left(2\theta_e - \frac{2}{3}\pi\right), \\ L_{ab} &= L_{ba} = L_{mutual} + L_{salient} \cos\left(2\theta_e - \frac{2}{3}\pi\right), \\ L_{bc} &= L_{cb} = L_{mutual} + L_{salient} \cos(2\theta_e), \\ L_{ca} &= L_{ac} = L_{mutual} + L_{salient} \cos\left(2\theta_e + \frac{2}{3}\pi\right), \end{aligned} \quad (2.4)$$

(resulting in diagonal, θ_e independent, inductances after applying the $dq0$ -transformation which will be explained later in this section) where L_{self} and L_{mutual} are the constant parts of the self and mutual inductances, respectively, and $L_{salient}$ is an inductance term which is caused by saliency of the rotor depending on the electrical rotor angle θ_e

$$\theta_e = \frac{\#poles}{2}\theta, \quad (2.5)$$

(e.g. in figure 2.2 the $\#poles = 2$). The voltage equations are

$${}^{abc}\vec{u} = R {}^{abc}\vec{i} + \frac{d {}^{abc}\vec{\lambda}(\theta_e)}{dt}. \quad (2.6)$$

A useful method to analyze these machines is to make use of the direct- and quadrature-axis ($dq0$) theory. The theory uses the concept of resolving synchronous-machine armature quantities into two rotating components: The first component is called the direct-axis component, which is aligned with the direction of the rotor magnetization (in the case of permanent-magnet machines). The second component is called the quadrature component, which is in quadrature with (i.e. orthogonal to) the direct axis. Both components are shown in figure 2.2. The original idea behind this transformation (the Blondel two-reaction method) is derived from the work of A.E. Blondel in France. The transformation was further developed by R.E. Doherty and C.A. Nickle [8, 9, 10, 11] and by R.H. Park [33, 34]. The vector/matrix notations of the $dq0$ transformation used in this section are in accordance with [13]. A few assumptions have been made for this method to be valid. The following is

quoted from [33]: "Attention is restricted to symmetrical three-phase machines with field structure symmetrical about the axes of the field winding and inter-polar space, but salient poles and an arbitrary number of rotor circuits is considered. Idealization is resorted to, to the extent that saturation and hysteresis in every magnetic circuit and eddy currents in the armature iron are neglected, and in the assumption that, as far as concerns effects depending on the position of the rotor, each armature winding may be regarded as, in effect, sinusoidally distributed." The power-invariant transformation is given by

$$\begin{bmatrix} S_d \\ S_q \\ S_0 \end{bmatrix} = \frac{2}{3} \begin{bmatrix} \cos(\theta_e) & \cos(\theta_e - \frac{2}{3}\pi) & \cos(\theta_e + \frac{2}{3}\pi) \\ -\sin(\theta_e) & -\sin(\theta_e - \frac{2}{3}\pi) & -\sin(\theta_e + \frac{2}{3}\pi) \\ \frac{1}{2} & \frac{1}{2} & \frac{1}{2} \end{bmatrix} \begin{bmatrix} S_a \\ S_b \\ S_c \end{bmatrix}, \quad (2.7)$$

where S represents an instantaneous stator quantity to be transformed (e.g. current, voltage or flux), the subscripts a , b and c represent the three stator phases, respectively, the subscripts d and q represent the direct and quadrature axes, respectively, and θ_e is the electrical angle given by (2.5). The inverse $dq0$ transformation is given by

$$\begin{bmatrix} S_a \\ S_b \\ S_c \end{bmatrix} = \begin{bmatrix} \cos(\theta_e) & -\sin(\theta_e) & 1 \\ \cos(\theta_e - \frac{2}{3}\pi) & -\sin(\theta_e - \frac{2}{3}\pi) & 1 \\ \cos(\theta_e + \frac{2}{3}\pi) & -\sin(\theta_e + \frac{2}{3}\pi) & 1 \end{bmatrix} \begin{bmatrix} S_d \\ S_q \\ S_0 \end{bmatrix}. \quad (2.8)$$

The third component, indicated by subscript 0, is added to the d and q components to create a unique transformation of the three stator phase components. For notational simplicity (2.7) and (2.8) are written as

$$dq0 \vec{s} = dq0 \mathbf{T}_{abc}(\theta_e) abc \vec{s}, \quad (2.9)$$

and

$$abc \vec{s} = abc \mathbf{T}_{dq0}(\theta_e) dq0 \vec{s}, \quad (2.10)$$

respectively.

When applying the transformation to the flux linkages described by (2.1) the following result is obtained

$$dq0 \vec{\lambda} = dq0 \mathbf{L} dq0 \vec{i} + dq0 \vec{\lambda}_{pm}, \quad (2.11)$$

where

$$dq0 \mathbf{L} = dq0 \mathbf{T}_{abc}(\theta_e) abc \mathbf{L}(\theta_e) abc \mathbf{T}_{dq0}(\theta_e) = \begin{bmatrix} L_d & 0 & 0 \\ 0 & L_q & 0 \\ 0 & 0 & L_0 \end{bmatrix}, \quad (2.12)$$

and

$$dq^0 \vec{\lambda}_{pm} = dq^0 \mathbf{T}_{abc}(\theta_e) \mathbf{abc} \vec{\lambda}_{pm}(\theta_e) = \begin{bmatrix} \lambda_{pm} \\ 0 \\ 0 \end{bmatrix}, \quad (2.13)$$

are now independent of the electrical rotor angle θ_e . The direct-axis and quadrature-axis synchronous inductances L_d and L_q , and the zero-sequence inductance L_0 are equal to

$$\begin{aligned} L_d &= L_{self} - L_{mutual} + \frac{3}{2} L_{salient}, \\ L_q &= L_{self} - L_{mutual} - \frac{3}{2} L_{salient}, \\ L_0 &= L_{self} + 2L_{mutual}. \end{aligned} \quad (2.14)$$

Transformation of the voltage equations (2.6) results in

$$\begin{aligned} dq^0 \vec{u} &= dq^0 \mathbf{T}_{abc}(\theta_e) \left(R \mathbf{abc} \mathbf{T}_{dq^0}(\theta_e) dq^0 \vec{i} + \frac{d \mathbf{abc} \mathbf{T}_{dq^0}(\theta_e) dq^0 \vec{\lambda}}{dt} \right) \\ &= R dq^0 \vec{i} + dq^0 \mathbf{L} \frac{dq^0 \vec{i}}{dt} + \frac{\partial \theta_e}{\partial t} \begin{bmatrix} 0 & -1 & 0 \\ 1 & 0 & 0 \\ 0 & 0 & 0 \end{bmatrix} dq^0 \vec{\lambda}, \end{aligned} \quad (2.15)$$

where

$$dq^0 \vec{u}_{sv} = \frac{\partial \theta_e}{\partial t} \begin{bmatrix} 0 & -1 & 0 \\ 1 & 0 & 0 \\ 0 & 0 & 0 \end{bmatrix} dq^0 \vec{\lambda}, \quad (2.16)$$

is the speed-voltage term. The instantaneous power p_s then becomes

$$\begin{aligned} p_s &= \mathbf{abc} \vec{u}^T \mathbf{abc} \vec{i} = dq^0 \vec{u}^T \mathbf{abc} \mathbf{T}_{dq^0}(\theta_e)^T \mathbf{abc} \mathbf{T}_{dq^0}(\theta_e) dq^0 \vec{i} \\ &= \frac{3}{2} dq^0 \vec{u}^T \begin{bmatrix} 1 & 0 & 0 \\ 0 & 1 & 0 \\ 0 & 0 & 2 \end{bmatrix} dq^0 \vec{i}. \end{aligned} \quad (2.17)$$

The electromagnetic torque, T_{mech} , is obtained by dividing the power output corresponding to the speed-voltage term by the mechanical speed $\frac{d\theta}{dt}$

$$\begin{aligned} T_{mech} &= \frac{3}{2} \left(\frac{d\theta}{dt} \right)^{-1} \frac{\partial \theta_e}{\partial t} dq^0 \vec{\lambda}^T \begin{bmatrix} 0 & 1 & 0 \\ -1 & 0 & 0 \\ 0 & 0 & 0 \end{bmatrix} dq^0 \vec{i} \\ &= \frac{3}{2} \left(\frac{\#poles}{2} \right) (\lambda_{pm} i_q + (L_d - L_q) i_d i_q). \end{aligned} \quad (2.18)$$

For three-phase two-pole synchronous permanent-magnet machines without saliency ($L_d = L_q$ and $\theta_e = \theta$) as in figure 2.2, equation 2.18 can be simplified to

$$\boxed{T_{mech} = \frac{3}{2} \lambda_{pm} i_q}. \quad (2.19)$$

2.3 Linear actuators

In this section the classical $dq0$ transformation (see section 2.2) is adapted towards linear actuators. Figure 2.3 shows a schematic representation of an idealized linear three-phase synchronous permanent-magnet actuator. The linear actuator can be interpreted as an unrolled version of the rotating actuator shown in figure 2.2. A pole-pitch τ is introduced which is the distance between the magnet poles as indicated in figure 2.3. However, there are differences. Firstly, the coils have been

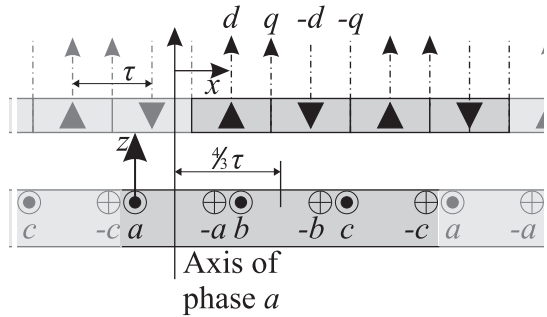


Figure 2.3. Schematic representation of an ideal linear three-phase synchronous permanent-magnet actuator.

placed at a distance of $\frac{4\tau}{3}$ m instead of $\frac{2\tau}{3}$ m to prevent overlap of the coil-windings. Secondly, the distance between the c and a stator coils is different from the distances between the a and b, and the b and c coils which destroys the symmetry of the mutual inductances between the coils. Although this constraint is removed later in this section, the symmetry is restored first by deriving the force of one three-phase group, while assuming a stator containing an infinite set of balanced three-phase coil groups with the same i_a, i_b and i_c currents and an infinitely large magnet array. The flux linkage in stator phase quantities then becomes

$${}^{abc}\vec{\lambda}_l = {}^{abc}\mathbf{L}_l(x, z) {}^{abc}\vec{i} + {}^{abc}\vec{\lambda}_{pm,l}(x, z), \quad (2.20)$$

where the translator position $x = \frac{\tau}{\pi}\theta$ replaces the rotor angle, and the air-gap distance z is included as an additional degree-of-freedom. In chapter 3 the rotations are also included in the analysis. However, in this section and section 2.4 the rotations of the translator are neglected. The permanent-magnet flux now becomes

[17]

$${}^{abc}\vec{\lambda}_{pm,l}(x, z) = \lambda_{pm} \exp\left(-\frac{\pi}{\tau}z\right) \begin{bmatrix} \cos\left(\frac{\pi}{\tau}x\right) \\ \cos\left(\frac{\pi}{\tau}x + \frac{2}{3}\pi\right) \\ \cos\left(\frac{\pi}{\tau}x - \frac{2}{3}\pi\right) \end{bmatrix}. \quad (2.21)$$

Ideally, the self and mutual inductances of the three stator coils then become

$$\begin{aligned} L_{aa,l} &= L_{self,l}(z) + L_{salient,l}(z) \cos\left(2\frac{\pi}{\tau}x\right), \\ L_{bb,l} &= L_{self,l}(z) + L_{salient,l}(z) \cos\left(2\frac{\pi}{\tau}x - \frac{2}{3}\pi\right), \\ L_{cc,l} &= L_{self,l}(z) + L_{salient,l}(z) \cos\left(2\frac{\pi}{\tau}x + \frac{2}{3}\pi\right), \\ L_{ab,l} &= L_{ba,l} = L_{mutual,l}^*(z) + L_{salient,l}(z) \cos\left(2\frac{\pi}{\tau}x + \frac{2}{3}\pi\right), \\ L_{bc,l} &= L_{cb,l} = L_{mutual,l}^*(z) + L_{salient,l}(z) \cos\left(2\frac{\pi}{\tau}x\right), \\ L_{ca,l} &= L_{ac,l} = L_{mutual,l}^*(z) + L_{salient,l}(z) \cos\left(2\frac{\pi}{\tau}x - \frac{2}{3}\pi\right), \end{aligned} \quad (2.22)$$

where $L_{mutual,l}^*(z)$ is the effective mutual inductance including the mutual inductances of the neighboring balanced three-phase groups operating at the same currents (to maintain the same symmetry as with the rotating machine).

The following derivation is comparable to the work of Won-Jon Kim [29]. The $dq0$ transformation ${}^{dq0}\mathbf{T}_{abc,l}(x)$ and its inverse transformation ${}^{abc}\mathbf{T}_{dq0,l}(x)$ have been adapted to match the linear actuator as follows

$${}^{dq0}\mathbf{T}_{abc,l}(x) = \frac{2}{3} \begin{bmatrix} \cos\left(\frac{\pi}{\tau}x\right) & \cos\left(\frac{\pi}{\tau}x + \frac{2}{3}\pi\right) & \cos\left(\frac{\pi}{\tau}x - \frac{2}{3}\pi\right) \\ -\sin\left(\frac{\pi}{\tau}x\right) & -\sin\left(\frac{\pi}{\tau}x + \frac{2}{3}\pi\right) & -\sin\left(\frac{\pi}{\tau}x - \frac{2}{3}\pi\right) \\ \frac{1}{2} & \frac{1}{2} & \frac{1}{2} \end{bmatrix}, \quad (2.23)$$

$${}^{abc}\mathbf{T}_{dq0,l}(x) = \begin{bmatrix} \cos\left(\frac{\pi}{\tau}x\right) & -\sin\left(\frac{\pi}{\tau}x\right) & 1 \\ \cos\left(\frac{\pi}{\tau}x + \frac{2}{3}\pi\right) & -\sin\left(\frac{\pi}{\tau}x + \frac{2}{3}\pi\right) & 1 \\ \cos\left(\frac{\pi}{\tau}x - \frac{2}{3}\pi\right) & -\sin\left(\frac{\pi}{\tau}x - \frac{2}{3}\pi\right) & 1 \end{bmatrix}. \quad (2.24)$$

When applying the transformations given by (2.23) and (2.24) to the linear actuator, comparable results are obtained as with the rotating actuator described in section 2.2. The main differences are that after transformation the inductance matrix ${}^{dq0}\mathbf{L}_l$ and the permanent magnet flux ${}^{dq0}\vec{\lambda}_{pm,l}$ have become z dependent, as follows

$$\begin{aligned} L_d(z) &= L_{self,l}(z) - L_{mutual,l}^*(z) + \frac{3}{2}L_{salient,l}(z), \\ L_q(z) &= L_{self,l}(z) - L_{mutual,l}^*(z) - \frac{3}{2}L_{salient,l}(z), \\ L_0(z) &= L_{self,l}(z) + 2L_{mutual,l}^*(z), \end{aligned} \quad (2.25)$$

$${}^{dq0}\vec{\lambda}_{pm,l}(z) = \exp\left(-\frac{\pi}{\tau}z\right) \begin{bmatrix} \lambda_{pm} \\ 0 \\ 0 \end{bmatrix}. \quad (2.26)$$

The z dependency results in an additional speed-voltage term. The speed-voltage terms in $dq0$ coordinates are

$$dq0 \vec{u}_{sv,x} = \frac{\pi}{\tau} \frac{\partial x}{\partial t} \begin{bmatrix} 0 & -1 & 0 \\ 1 & 0 & 0 \\ 0 & 0 & 0 \end{bmatrix} dq0 \vec{\lambda}(z), \quad (2.27)$$

and

$$dq0 \vec{u}_{sv,z} = \frac{\partial z}{\partial t} \left(\frac{\partial dq0 L_l(z)}{\partial z} dq0 \vec{i}_l + \frac{\partial dq0 \vec{\lambda}_{pm,l}(z)}{\partial z} \right). \quad (2.28)$$

The electromagnetic forces, $F_{x,l}$ and $F_{z,l}$, are again obtained by dividing the power output corresponding to the speed-voltage term by the mechanical speeds $\frac{dx}{dt}$ and $\frac{dz}{dt}$, respectively

$$F_{x,l} = \frac{3}{2} \frac{\pi}{\tau} dq0 \vec{\lambda}_l^T(z) \begin{bmatrix} 0 & 1 & 0 \\ -1 & 0 & 0 \\ 0 & 0 & 0 \end{bmatrix} dq0 \vec{i} \quad (2.29)$$

$$= \frac{3}{2} \frac{\pi}{\tau} (\lambda_{pm,l} \exp(-\frac{\pi}{\tau} z) i_q + (L_d(z) - L_q(z)) i_d i_q),$$

$$F_{z,l} = \frac{3}{2} \left(dq0 \vec{i}_l^T \frac{\partial dq0 L_l^T(z)}{\partial z} + \frac{\partial dq0 \vec{\lambda}_{pm,l}(z)}{\partial z} \right) \begin{bmatrix} 1 & 0 & 0 \\ 0 & 1 & 0 \\ 0 & 0 & 2 \end{bmatrix} dq0 \vec{i}_l \quad (2.30)$$

$$= \frac{3}{2} \left(\frac{\partial L_d(z)}{\partial z} i_d^2 + \frac{\partial L_q(z)}{\partial z} i_q^2 + 2 \frac{\partial L_0(z)}{\partial z} i_0^2 - \frac{\pi}{\tau} \lambda_{pm,l} \exp(-\frac{\pi}{\tau} z) i_d \right).$$

Without saliency of the translator ($L_d = L_q$), the force in the x -direction $F_{x,l}$ simplifies to:

$$F_{x,l} = \frac{3}{2} \frac{\pi}{\tau} \lambda_{pm,l} \exp\left(-\frac{\pi}{\tau} z\right) i_q. \quad (2.31)$$

When all materials are considered to have a relative permeability μ_r equal to one (no reluctance forces) the force in the z -direction $F_{z,l}$ simplifies to

$$F_{z,l} = -\frac{3}{2} \frac{\pi}{\tau} \lambda_{pm,l} \exp\left(-\frac{\pi}{\tau} z\right) i_d. \quad (2.32)$$

Moreover, when assuming all materials to have $\mu_r = 1$ and ideal current amplifiers, it is not only possible to analyze the linear actuator as a Lorentz actuator (since the force calculation through the flux linkage and the Lorentz force are equivalent for a current loop in an external magnetic field [12]), but the need for symmetry

is also removed. The $dq0$ -transformation can still be effectively applied to linearize and decouple the permanent-magnet flux linkage ${}^{abc}\vec{\lambda}_{pm,l}(x, z)$. When (2.20) is applied to the voltage equations and (2.24) is applied to the permanent magnet flux linkage ${}^{abc}\vec{\lambda}_{pm,l}(x, z)$ the following result is obtained

$${}^{abc}\vec{u}_l = R {}^{abc}\vec{i}_l + {}^{abc}L_l \frac{d {}^{abc}\vec{i}_l}{dt} + {}^{abc}\vec{u}_{sv,x} + {}^{abc}\vec{u}_{sv,z}, \quad (2.33)$$

where ${}^{abc}L_l$ is position independent and where ${}^{abc}\vec{u}_{sv,x}$ and ${}^{abc}\vec{u}_{sv,z}$ are given by

$${}^{abc}\vec{u}_{sv,x} = \frac{\partial x}{\partial t} \frac{\partial {}^{abc}\mathbf{T}_{dq0,l}(x)}{\partial x} {}^{dq0}\vec{\lambda}_{pm,l}(z), \quad (2.34)$$

$${}^{abc}\vec{u}_{sv,z} = \frac{\partial z}{\partial t} {}^{abc}\mathbf{T}_{dq0,l}(x) \frac{\partial {}^{dq0}\vec{\lambda}_{pm,l}(z)}{\partial z}. \quad (2.35)$$

The electromagnetic forces, $F_{x,l}$ and $F_{z,l}$, then become equal to (2.31) and (2.32), respectively. It is then possible to linearize and decouple the forces by feedback using the inverse mapping of (2.31) and (2.32)

$${}^{dq0}\vec{i}_{des,l} = \frac{2}{3} \frac{\tau}{\pi} \frac{1}{\lambda_{pm,l}} \exp\left(\frac{\pi}{\tau} z\right) \begin{bmatrix} 0 & -1 \\ 1 & 0 \\ 0 & 0 \end{bmatrix} \begin{bmatrix} F_{desx,l} \\ F_{desz,l} \end{bmatrix}, \quad (2.36)$$

or in the real abc stator frame currents

$$\boxed{{}^{abc}\vec{i}_{des,l} = \frac{2}{3} \frac{\tau}{\pi} \frac{1}{\lambda_{pm,l}} \exp\left(\frac{\pi}{\tau} z\right) {}^{abc}\mathbf{T}_{dq0,l}(x) \begin{bmatrix} 0 & -1 \\ 1 & 0 \\ 0 & 0 \end{bmatrix} \begin{bmatrix} F_{desx,l} \\ F_{desz,l} \end{bmatrix}}. \quad (2.37)$$

The current on the zero axis i_0 can have an arbitrary value since it does not contribute to the force production. In (2.36), however, i_0 is set to zero in order to minimize the power dissipation (which can be seen from (2.17)).

The transformation described above is not limited to three-phase systems. Figure 2.4 shows a semi-four-phase actuator (a four-phase actuator of which only the first and the second or fourth phase are used). The transformation matrices then become

$${}^{dq}\mathbf{T}_{ab,l}(x) = {}^{ab}\mathbf{T}_{dq,l}(x) = \begin{bmatrix} \cos\left(\frac{\pi}{\tau} x\right) & -\sin\left(\frac{\pi}{\tau} x\right) \\ -\sin\left(\frac{\pi}{\tau} x\right) & -\cos\left(\frac{\pi}{\tau} x\right) \end{bmatrix}, \quad (2.38)$$

where there is no 0-axis anymore because the matrix is already uniquely defined. The currents can then be derived equivalent to the derivation of (2.37), resulting in

$${}^{ab}\vec{i}_{des,l} = \frac{\tau}{\pi} \frac{1}{\lambda_{pm,l}} \exp\left(\frac{\pi}{\tau} z\right) {}^{ab}\mathbf{T}_{dq,l}(x) \begin{bmatrix} 0 & -1 \\ 1 & 0 \end{bmatrix} \begin{bmatrix} F_{desx,l} \\ F_{desz,l} \end{bmatrix}. \quad (2.39)$$

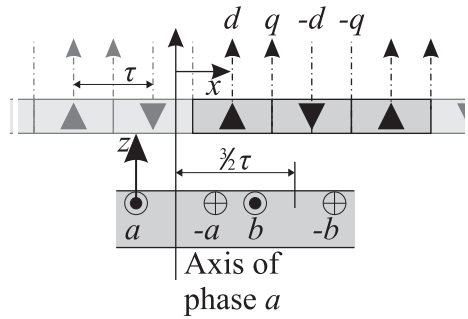


Figure 2.4. Schematic representation of an ideal linear ironless semi-four-phase synchronous permanent-magnet actuator.

2.4 Basic forcer topologies for planar motion

In this section the $dq0$ transformation is extended to cope with ironless planar actuators without overlapping coils in the stator plane. A more extensive treatise of various planar-machine topologies can be found in [17]. The first configuration consists of four round or square coils distanced according to a semi-four-phase system but in two orthogonal directions x and y (as shown in figure 2.5). The topology is based on a patent of Hazelton [15] and the $dq0$ transformation for this topology, derived in this thesis, is similar to [41, 40]. The basic principle is an expansion

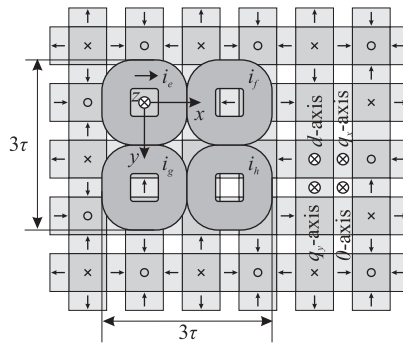


Figure 2.5. Basic forcer using square coils.

of the semi-four-phase linear actuator explained in section 2.3. The magnet array

shown in figure 2.5 is called a Halbach magnet array which is used to increase and concentrate the magnetic flux density near the coils. The topology has two q -axes: One axis belonging to the x -direction and one belonging to the y -direction, called q_x and q_y , respectively. The $dq_x dq_y 0$ transformation matrices belonging to figure 2.5 are given by

$$dq_x dq_y 0 \mathbf{T}_{efgh} = efgh \mathbf{T}_{dq_x dq_y 0} = \begin{bmatrix} c\left(\frac{\pi x}{\tau}\right) c\left(\frac{\pi y}{\tau}\right) & -s\left(\frac{\pi x}{\tau}\right) c\left(\frac{\pi y}{\tau}\right) & -c\left(\frac{\pi x}{\tau}\right) s\left(\frac{\pi y}{\tau}\right) & s\left(\frac{\pi x}{\tau}\right) s\left(\frac{\pi y}{\tau}\right) \\ -s\left(\frac{\pi x}{\tau}\right) c\left(\frac{\pi y}{\tau}\right) & -c\left(\frac{\pi x}{\tau}\right) c\left(\frac{\pi y}{\tau}\right) & s\left(\frac{\pi x}{\tau}\right) s\left(\frac{\pi y}{\tau}\right) & c\left(\frac{\pi x}{\tau}\right) s\left(\frac{\pi y}{\tau}\right) \\ -c\left(\frac{\pi x}{\tau}\right) s\left(\frac{\pi y}{\tau}\right) & s\left(\frac{\pi x}{\tau}\right) s\left(\frac{\pi y}{\tau}\right) & -c\left(\frac{\pi x}{\tau}\right) c\left(\frac{\pi y}{\tau}\right) & s\left(\frac{\pi x}{\tau}\right) c\left(\frac{\pi y}{\tau}\right) \\ s\left(\frac{\pi x}{\tau}\right) s\left(\frac{\pi y}{\tau}\right) & c\left(\frac{\pi x}{\tau}\right) s\left(\frac{\pi y}{\tau}\right) & s\left(\frac{\pi x}{\tau}\right) c\left(\frac{\pi y}{\tau}\right) & c\left(\frac{\pi x}{\tau}\right) c\left(\frac{\pi y}{\tau}\right) \end{bmatrix}, \quad (2.40)$$

which are orthonormal matrices (where for notational simplicity sin and cos have been replaced by s and c, respectively). The three speed-voltage terms then become

$$efgh \vec{u}_{sv,x} = \frac{\partial x}{\partial t} \frac{\partial efgh \mathbf{T}_{dq_x dq_y 0}(x, y)}{\partial x} dq_0 \vec{\lambda}_{pm,pl}(z), \quad (2.41)$$

$$efgh \vec{u}_{sv,y} = \frac{\partial y}{\partial t} \frac{\partial efgh \mathbf{T}_{dq_x dq_y 0}(x, y)}{\partial y} dq_0 \vec{\lambda}_{pm,pl}(z), \quad (2.42)$$

and

$$efgh \vec{u}_{sv,z} = \frac{\partial z}{\partial t} efgh \mathbf{T}_{dq_x dq_y 0}(x, y) \frac{\partial dq_0 \vec{\lambda}_{pm,pl}(z)}{\partial z}, \quad (2.43)$$

with their respective force components

$$F_x = \frac{\pi}{\tau} \lambda_{pm} \exp\left(-\frac{\sqrt{2}\pi}{\tau} z\right) i_{q_x}, \quad (2.44)$$

$$F_y = \frac{\pi}{\tau} \lambda_{pm} \exp\left(-\frac{\sqrt{2}\pi}{\tau} z\right) i_{q_y}, \quad (2.45)$$

$$F_z = -\frac{\sqrt{2}\pi}{\tau} \lambda_{pm} \exp\left(-\frac{\sqrt{2}\pi}{\tau} z\right) i_d. \quad (2.46)$$

$$(2.47)$$

The currents which can be used to linearize and decouple the system then become

$${}^{efgh}\vec{i}_{des} = \frac{\tau}{\pi} \frac{1}{\lambda_{pm}} \exp\left(\frac{\sqrt{2}\pi}{\tau} z\right) {}^{efgh}\mathbf{T}_{dq_0q_y0}(x, y) \begin{bmatrix} 0 & 0 & -\frac{\sqrt{2}}{2} \\ 1 & 0 & 0 \\ 0 & 1 & 0 \\ 0 & 0 & 0 \end{bmatrix} \begin{bmatrix} F_{desx} \\ F_{desy} \\ F_{desz} \end{bmatrix}. \quad (2.48)$$

The second configuration discussed in this thesis uses rectangular coils and is shown in figure 2.6. The rectangular coils are optimized [4, 17] in such a way that they only produce force in either the xz -plane (light-grey coils) or the yz -plane (dark-grey coils). Consequently, the $dq0$ -decomposition derived for linear actuators in section 2.3 can be almost directly applied to this planar topology. The only difference is that, since the magnet array is rotated $\frac{\pi}{4}$ rad, a new effective pole-pitch

$$\tau_n = \frac{\tau}{\sqrt{2}}, \quad (2.49)$$

is introduced, which is also shown in figure 2.6. The inverse d_xq_x0 matrix belonging

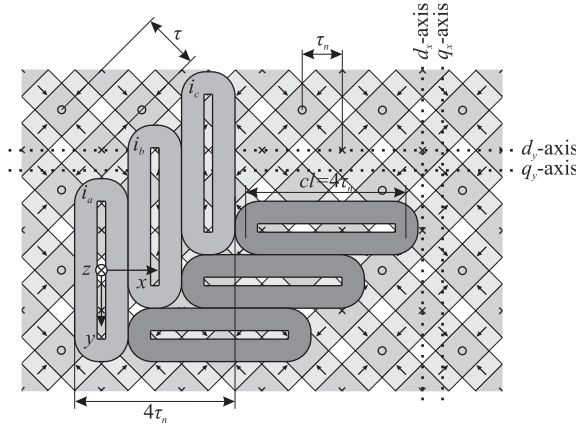


Figure 2.6. Basic forcers using rectangular coils.

to the light-grey coils then becomes

$${}^{abc}\mathbf{T}_{d_xq_x0,pl}(x) = \begin{bmatrix} \cos\left(\frac{\pi}{\tau_n} x\right) & -\sin\left(\frac{\pi}{\tau_n} x\right) & 1 \\ \cos\left(\frac{\pi}{\tau_n} x + \frac{2}{3}\pi\right) & -\sin\left(\frac{\pi}{\tau_n} x + \frac{2}{3}\pi\right) & 1 \\ \cos\left(\frac{\pi}{\tau_n} x - \frac{2}{3}\pi\right) & -\sin\left(\frac{\pi}{\tau_n} x - \frac{2}{3}\pi\right) & 1 \end{bmatrix}, \quad (2.50)$$

which results in the following currents for the light-grey coils

$$\boxed{abc\vec{i}_{des,pl} = \frac{2}{3} \frac{\tau_n}{\pi} \frac{1}{\lambda_{pm,l}} \exp\left(\frac{\pi}{\tau_n} z\right) abc\mathbf{T}_{d_x q_x 0, l}(x) \begin{bmatrix} 0 & -1 \\ 1 & 0 \\ 0 & 0 \end{bmatrix} \begin{bmatrix} F_{desx,pl} \\ F_{desz,pl} \end{bmatrix}}. \quad (2.51)$$

A similar solution can be obtained for the dark-grey coils (where x is substituted by y).

Chapter 3

Linearization and decoupling of the wrench

3.1 Introduction

Contrary to chapter 2, where the $dq0$ transformation was used to derive a decoupling strategy of the force components, this chapter focusses on a six degree-of-freedom approach towards solving the commutation algorithm. Classical $dq0$ transformation can only be used directly to derive a commutation which decouples the force components of linear/planar actuators. In moving-coil planar actuators such as [5] it is possible to use design symmetries which reduce the complexity of the torque equations, therefore, additional transformations can be derived which allow for decoupling of the torque [4]. Moving-magnet planar actuators with integrated magnetic bearing have complex torque equations. The result of these complex torque equations is that the classical $dq0$ -transformation, which focusses on the force components (when applied to planar actuators), is not practical to use since it does not directly include torque decoupling. In literature, attempts have been made to include decoupling of the torque by using additional transformations after applying $dq0$ -transformation [41, 40]. However, the resulting disturbance torque remained significant. In patent literature some improvements to the algorithms have been made by Binnard et al. [1, 2] resulting in a six DOF algorithm which still does not include the full torque equations. Moreover, since only the coils underneath or near the edges of the translator significantly produce force and torque, the set of active coils which are used to control the translator needs to change as a function of position. There are no explicit solutions given in [1, 2] which allow for switching of active coil sets without disturbing the decoupling.

The approach which is proposed in section 3.3 uses the six degree-of-freedom model derived in section 3.2 to achieve a direct wrench-current decoupling which, in contrast to the $dq0$ transformation, directly decouples the force and torque components. Moreover, section 3.3.1 expands the algorithm to include switching of active coil sets. The method presented in this thesis has also been published [44, 42, 43, 25]. The commutation algorithms and the real-time model derived in this chapter are the results of common research work of project partner ir. J.W. Jansen and the author of this thesis. As a result, these subjects are described in both theses. This thesis summarizes the real-time modeling results. A more extensive treatise on the electromechanical analysis and design, including more accurate models of the system, can be found in [17]. The models discussed in both theses were also published [24, 26, 22, 18, 23]. Section 3.4 uses the Schur complement to split the direct wrench-current decoupling into several components. Under certain assumptions, one of these components can be made equivalent to the sum of multiple $dq0$ transformations which were presented in section 2.4 (also published in [45, 46]).

3.2 Real-time analytical six degree-of-freedom coil model

The $dq0$ decomposition explained in chapter 2 can only be used directly to decouple forces (when applied to planar actuators). The reason for this is that the force distribution of the planar actuator is not taken into account. However, to accurately stabilize a platform in six degrees of freedom it is also necessary to control the torque about the center of mass. To do so a real-time six degree-of-freedom single coil model is derived in this section.

When assuming ideal magnets, quasi-static magnetic fields, negligible eddy currents, a wire diameter smaller than the skin depth, rigid body dynamics of the translator and no reluctance forces, the voltage equations can be simplified to

$$\vec{u} = \mathbf{R}\vec{i} + \mathbf{L}\frac{d\vec{i}}{dt} + \mathbf{J}_{\bar{\Lambda}_m}(\vec{q})\frac{d\vec{q}}{dt}, \quad (3.1)$$

where $\mathbf{J}_{\bar{\Lambda}_m}(\vec{q})$ is the Jacobian of the flux of the permanent-magnet array linked by the respective coils, \vec{q} is the 6-DOF vector consisting of the three position and three orientation components of the translator and \mathbf{R} and \mathbf{L} are the coils resistance and inductance matrices, respectively. Moreover, when assuming ideal current amplifiers, having an infinitely large internal resistance and bandwidth, and no cogging forces, the wrench vector (containing all force and torque components) is then given by

$$\vec{w}_{tot} = \mathbf{J}_{\bar{\Lambda}_m}(\vec{q})\vec{i}. \quad (3.2)$$

Since the force calculation through the flux linkage and the Lorentz force are equivalent for a current loop in an external magnetic field [12], the voltage equations can be solved with the force and torque calculated using magnetostatic models (i.e. using the Lorentz force and torque).

To obtain a fully analytical model, the coil is modeled by either four surfaces or four filaments, where the assumption is made that all coil currents and their effects can be represented as if the current was flowing through either four filaments or through four sheets with constant current density. Figure 3.1 shows the two coil models. Two coordinate systems are defined in the 3-D Euclidian space to model

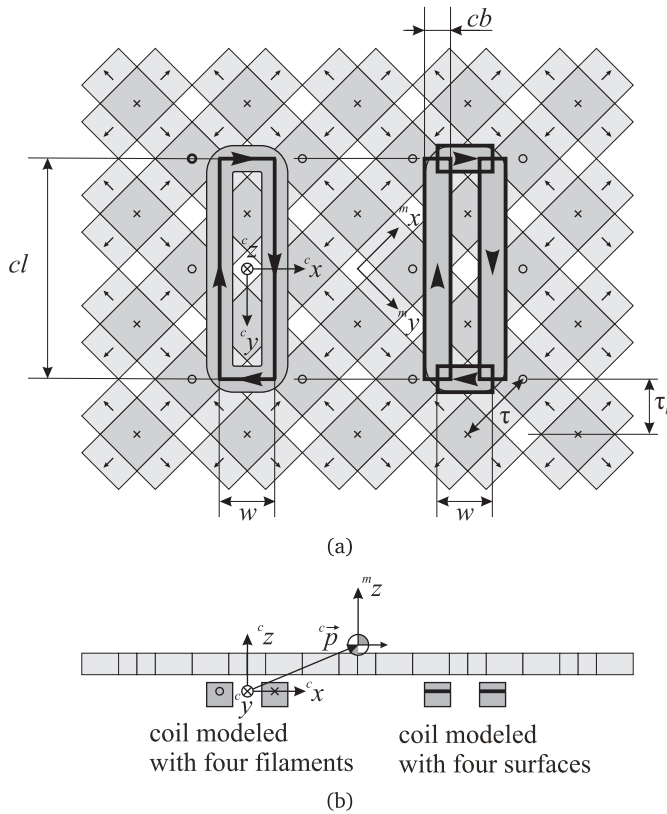


Figure 3.1. Filament (left) and sheet surface (right) model of a single rectangular coil: a) bottom view, b) cross section.

the actuator. Figure 3.1 shows a partial planar actuator, i.e. a Halbach permanent-magnet array and a single coil. A coordinate system is located at the stationary part of the actuator. In this coordinate system the stator coils are defined. For that reason it is denoted with the superscript c (of coils)

$${}^c\vec{x} = [{}^c x \quad {}^c y \quad {}^c z]^\top. \quad (3.3)$$

Another coordinate system is fixed to the mass center point of the total translator (although figure 3.1 only shows the permanent magnets). In this coordinate system the magnets are defined. This coordinate frame is denoted with the superscript m (of magnets)

$${}^m\vec{x} = [{}^m x \quad {}^m y \quad {}^m z]^\top. \quad (3.4)$$

The vector

$${}^c\vec{p} = [{}^c p_x \quad {}^c p_y \quad {}^c p_z]^\top, \quad (3.5)$$

is the position of the magnet coordinate system m , i.e. the mass center point of the translator, in the coil coordinate system c .

Coordinates are transformed from one system to the other with an orientation transformation and afterwards a translation. The transformation matrix ${}^c\mathbf{T}_m$ for a position from the magnet to the coil coordinate system is equal to [31]

$${}^c\mathbf{T}_m = \begin{bmatrix} {}^c\mathbf{R}_m & {}^c\vec{p} \\ 0 & 1 \end{bmatrix}. \quad (3.6)$$

For convenience, the orientation transformation matrix is defined as

$${}^c\mathbf{R}_m = \mathbf{Rot}({}^c y, \theta)\mathbf{Rot}({}^c x, \psi)\mathbf{Rot}({}^c z, \phi), \quad (3.7)$$

where

$$\mathbf{Rot}({}^c y, \theta) = \begin{bmatrix} \cos(\theta) & 0 & \sin(\theta) \\ 0 & 1 & 0 \\ -\sin(\theta) & 0 & \cos(\theta) \end{bmatrix}, \quad (3.8)$$

$$\mathbf{Rot}({}^c x, \psi) = \begin{bmatrix} 1 & 0 & 0 \\ 0 & \cos(\psi) & -\sin(\psi) \\ 0 & \sin(\psi) & \cos(\psi) \end{bmatrix}, \quad (3.9)$$

$$\mathbf{Rot}({}^c z, \phi) = \begin{bmatrix} \cos(\phi) & -\sin(\phi) & 0 \\ \sin(\phi) & \cos(\phi) & 0 \\ 0 & 0 & 1 \end{bmatrix}, \quad (3.10)$$

and where ψ , θ and ϕ are the (Euler) rotation angles about the ${}^c x$ -, ${}^c y$ -, and ${}^c z$ -axes, respectively. Thus, the position and orientation of the translator can be described in six degrees-of-freedom. The transformation matrix ${}^m \mathbf{T}_c$ for a position from the global to the local coordinate system is equal to

$$\begin{aligned} {}^m \mathbf{T}_c &= {}^c \mathbf{T}_m^{-1} = \begin{bmatrix} {}^c \mathbf{R}_m^\top & -{}^c \mathbf{R}_m^\top {}^c \vec{p} \\ 0 & 1 \end{bmatrix} \\ &= \begin{bmatrix} {}^m \mathbf{R}_c & -{}^m \mathbf{R}_c {}^c \vec{p} \\ 0 & 1 \end{bmatrix}, \end{aligned} \quad (3.11)$$

because ${}^c \mathbf{T}_m$ is orthonormal.

Applying the appropriate transformation matrix, a position is transferred between the coordinate systems, according to

$$\begin{bmatrix} {}^m \vec{x} \\ 1 \end{bmatrix} = {}^m \mathbf{T}_c \begin{bmatrix} {}^c \vec{x} \\ 1 \end{bmatrix}, \quad (3.12)$$

$${}^m \vec{x} = {}^m \mathbf{R}_c ({}^c \vec{x} - {}^c \vec{p}), \quad (3.13)$$

and a free vector as defined in [31], e.g. the spatial current vector \vec{i} (consisting of the directional components of the current along the x , y and z directions), according to

$$\begin{bmatrix} {}^m \vec{i} \\ 0 \end{bmatrix} = {}^m \mathbf{T}_c \begin{bmatrix} {}^c \vec{i} \\ 0 \end{bmatrix}, \quad (3.14)$$

$${}^m \vec{i} = {}^m \mathbf{R}_c {}^c \vec{i}. \quad (3.15)$$

The analytical model, applied here, only takes the first harmonic of the magnetic flux density distribution of the permanent-magnet array into account. The simplified magnetic flux density expression (assuming the coils are located underneath the permanent-magnet array) is given by

$${}^m \vec{B}_3 ({}^m \vec{x}) = -\exp\left(\frac{\pi\sqrt{2}}{\tau} {}^m z\right) \begin{bmatrix} B_{xy} \cos\left(\frac{\pi^m x}{\tau}\right) \sin\left(\frac{\pi^m y}{\tau}\right) \\ B_{xy} \sin\left(\frac{\pi^m x}{\tau}\right) \cos\left(\frac{\pi^m y}{\tau}\right) \\ B_z \sin\left(\frac{\pi^m x}{\tau}\right) \sin\left(\frac{\pi^m y}{\tau}\right) \end{bmatrix}, \quad (3.16)$$

where B_{xy} and B_z are derived from the amplitudes of the mean value of the first harmonic of the magnetic flux density components over the cross section of the coil at ${}^m z = 0$. Transformation of this expression into the coordinate system of the coils

$${}^c \vec{B}_3 ({}^c \vec{x}, {}^c \vec{p}) = {}^c \mathbf{R}_m {}^m \vec{B}_3 ({}^m \mathbf{R}_c ({}^c \vec{x} - {}^c \vec{p})), \quad (3.17)$$

results for ($\phi = -\pi/4$ rad and $\psi = \theta = 0$ rad) in

$${}^c\vec{\mathbf{B}}_3({}^c\vec{\mathbf{x}}, {}^c\vec{\mathbf{p}}) \Big|_{\substack{\psi=\theta=0 \\ \psi=-\pi/4}} = \left[\begin{array}{c} -\frac{B_{xy}}{\sqrt{2}} \exp\left(\frac{\pi}{\tau_n}(cz - cp_z)\right) \sin\left(\frac{\pi}{\tau_n}(cx - cp_x)\right) \\ \frac{B_{xy}}{\sqrt{2}} \exp\left(\frac{\pi}{\tau_n}(cz - cp_z)\right) \sin\left(\frac{\pi}{\tau_n}(cy - cp_y)\right) \\ \frac{1}{2}B_z \exp\left(\frac{\pi}{\tau_n}(cz - cp_z)\right) \left(\cos\left(\frac{\pi}{\tau_n}(cx - cp_x)\right) - \cos\left(\frac{\pi}{\tau_n}(cy - cp_y)\right)\right) \end{array} \right], \quad (3.18)$$

where a new pole pitch τ_n is introduced, which is indicated in figure 3.1

$$\tau_n = \frac{\tau}{\sqrt{2}}. \quad (3.19)$$

The Lorentz force on the filaments is calculated by solving a line integral. The force exerted on the translator ${}^c\vec{\mathbf{F}} = [{}^cF_x \quad {}^cF_y \quad {}^cF_z]^\top$, expressed in the coil coordinate system, by one coil, which is located at ${}^c\vec{\mathbf{x}} = [{}^cx \quad {}^cy \quad 0]^\top$, is equal to

$$\begin{aligned} {}^c\vec{\mathbf{F}} &= -\oint_C {}^c\vec{\mathbf{i}} \times {}^c\vec{\mathbf{B}}_3 dl = \\ &= -\int_{{}^cx-w/2}^{{}^cx+w/2} [i \ 0 \ 0]^\top \times {}^c\vec{\mathbf{B}}_3 \left([{}^cx' \quad {}^cy - cl/2 \ 0]^\top, {}^c\vec{\mathbf{p}} \right) d{}^cx' \\ &= -\int_{{}^cy-cl/2}^{{}^cy+cl/2} [0 \ i \ 0]^\top \times {}^c\vec{\mathbf{B}}_3 \left([{}^cx + w/2 \quad {}^cy' \ 0]^\top, {}^c\vec{\mathbf{p}} \right) d{}^cy' \\ &= -\int_{{}^cx-w/2}^{{}^cx+w/2} [-i \ 0 \ 0]^\top \times {}^c\vec{\mathbf{B}}_3 \left([{}^cx' \quad {}^cy + cl/2 \ 0]^\top, {}^c\vec{\mathbf{p}} \right) d{}^cx' \\ &= -\int_{{}^cy-cl/2}^{{}^cy+cl/2} [0 \ -i \ 0]^\top \times {}^c\vec{\mathbf{B}}_3 \left([{}^cx - w/2 \quad {}^cy' \ 0]^\top, {}^c\vec{\mathbf{p}} \right) d{}^cy', \end{aligned} \quad (3.20)$$

where w and cl are the sizes of the filament coil along the cx - and cy -directions, respectively, and i is the current through the coil in Ampere-turns.

The torque exerted on the translator ${}^c\vec{\mathbf{T}} = [{}^cT_x \quad {}^cT_y \quad {}^cT_z]^\top$, expressed in the global coordinate system, by the same coil is equal to

$$\begin{aligned} {}^c\vec{\mathbf{T}} &= -\oint_C ({}^c\vec{\mathbf{x}} - {}^c\vec{\mathbf{p}}) \times \left({}^c\vec{\mathbf{i}} \times {}^c\vec{\mathbf{B}}_3 \right) dl = \\ &= -\int_{{}^cx-w/2}^{{}^cx+w/2} ({}^c\vec{\mathbf{x}} - {}^c\vec{\mathbf{p}}) \times \left([i \ 0 \ 0]^\top \times {}^c\vec{\mathbf{B}}_3 \left([{}^cx' \quad {}^cy - cl/2 \ 0]^\top, {}^c\vec{\mathbf{p}} \right) \right) d{}^cx' \\ &= -\int_{{}^cy-cl/2}^{{}^cy+cl/2} ({}^c\vec{\mathbf{x}} - {}^c\vec{\mathbf{p}}) \times \left([0 \ i \ 0]^\top \times {}^c\vec{\mathbf{B}}_3 \left([{}^cx + w/2 \quad {}^cy' \ 0]^\top, {}^c\vec{\mathbf{p}} \right) \right) d{}^cy' \\ &= -\int_{{}^cx-w/2}^{{}^cx+w/2} ({}^c\vec{\mathbf{x}} - {}^c\vec{\mathbf{p}}) \times \left([-i \ 0 \ 0]^\top \times {}^c\vec{\mathbf{B}}_3 \left([{}^cx' \quad {}^cy + cl/2 \ 0]^\top, {}^c\vec{\mathbf{p}} \right) \right) d{}^cx' \\ &= -\int_{{}^cy-cl/2}^{{}^cy+cl/2} ({}^c\vec{\mathbf{x}} - {}^c\vec{\mathbf{p}}) \times \left([0 \ -i \ 0]^\top \times {}^c\vec{\mathbf{B}}_3 \left([{}^cx - w/2 \quad {}^cy' \ 0]^\top, {}^c\vec{\mathbf{p}} \right) \right) d{}^cy'. \end{aligned} \quad (3.21)$$

The force and torque exerted on the translator (here expressed in coil coordinates c) are modeled as the reaction force and torque of the force and torque exerted on the coil. Hence, the minus signs in (3.21) and (3.20). If the length of the coil $cl = 2n\tau_n$, where n is an integer, and if $\phi = -\pi/4$ rad and $\psi = \theta = 0$ rad, the coil only produces force in the c_x - and c_z -directions and the force is independent on the c_{p_y} -position of the magnet array. The force and torque expressions for a coil with $w = \tau_n$ and $cl = 4\tau_n$ are given by

$${}^c F_x = -2\sqrt{2}B_z i\tau \exp\left(-\frac{\pi}{\tau_n} c_{p_z}\right) \sin\left(\frac{\pi}{\tau_n}(c_{p_x} - c_x)\right), \quad (3.22)$$

$${}^c F_y = 0, \quad (3.23)$$

$${}^c F_z = -4B_{xy} i\tau \exp\left(-\frac{\pi}{\tau_n} c_{p_z}\right) \cos\left(\frac{\pi}{\tau_n}(c_{p_x} - c_x)\right), \quad (3.24)$$

$${}^c T_x = (c_y - c_{p_y}) {}^c F_z - B_{xy} i\tau^2 \exp\left(-\frac{\pi}{\tau_n} c_{p_z}\right) \sin\left(\frac{\pi}{\tau_n}(c_{p_y} - c_y)\right), \quad (3.25)$$

$${}^c T_y = (c_{p_x} - c_x) {}^c F_z - c_{p_z} {}^c F_x, \quad (3.26)$$

$${}^c T_z = {}^c F_x (c_{p_y} - c_y). \quad (3.27)$$

In [17] it is derived that

$$B_z = \sqrt{2}B_{xy}, \quad (3.28)$$

which results in equal amplitudes of the c_x - and c_z -components of the force. The torque component ${}^c T_x$ cannot be expressed as an arm multiplied by a force. Therefore, a single attaching point of the force in the c_y -direction cannot be defined. Hence, for accurate torque calculation, the distribution of the force over the coil should be taken into account. Note that the cross-product with the arm, which is added in the line integral of the torque equation of the filament coil model (3.21), is inside the integral in order to include the force distribution over the coil. The coil model with four filaments assumes that the force can be modeled to act on the center of the conductor bundle. In reality, the distribution of the force over the conductor bundle changes with the relative position of the coil with respect to the magnet array. This can be shown by modeling the conductor bundle with a sheet or surface current. The obtained force and torque expressions for a coil with $w = \tau_n$, $cl = 4\tau_n$ and a conductor bundle width $cb = \tau_n/2$ and ($\phi = -\pi/4$ rad and $\psi = \theta = 0$ rad) are similar to the expressions for the coil modeled with four filaments, except for the ${}^c T_y$ term

$${}^c T_y = (c_{p_x} - c_x) {}^c F_z - c_{p_z} {}^c F_x + {}^c F_x \frac{B_{xy}(\pi - 4)\tau}{4B_z\pi}, \quad (3.29)$$

cT_y contains an extra term proportional to cF_x , which represents the torque caused by the change of the attaching point of the force in the conductor bundle of the coil. In further analyses in this thesis and in the controller of the realized planar actuator, the model based on the sheet currents is used. The reason for this is the higher accuracy of the torque model (as can be seen from the difference between (3.26) and (3.29)).

For notational simplicity the force and torque components are combined in a single wrench vector ${}^l\vec{w}_n = [{}^cF_x \quad {}^cF_y \quad {}^cF_z \quad {}^cT_x \quad {}^cT_y \quad {}^cT_z]^T$. The wrench vector ${}^l\vec{w}_n$ of a single coil n can then be described by

$${}^l\vec{w}_n = \vec{\gamma}_n ({}^l\vec{q}, {}^l\vec{r}_n) {}^l i_n, \quad (3.30)$$

where i_n is the current through the n^{th} coil, $\vec{\gamma}_n$ is the vector mapping the current to the wrench vector, ${}^l\vec{q} = [{}^c p_x \quad {}^c p_y \quad {}^c p_z \quad \psi \quad \theta \quad \phi]^T$ is the vector containing the position and orientation of the mass center point of the translator with respect to its reference frame in local coil coordinates (indicated by superscript l which is properly defined in section 3.3.1) and ${}^l\vec{r}_n = [{}^c x \quad {}^c y \quad \phi]^T$ is the location and orientation of the n^{th} coil in the xy -plane with respect to the origin of the local coil coordinates (where from this point ${}^c z = 0$). Since the model neglects the edge effects of the magnet array it is only valid when the coil is underneath the translator. Let \mathcal{S}_n be the set of admissible coordinates ${}^l\vec{q}$ for the model of the n^{th} coil to be valid. Figure 3.2 shows a top-view of coil n (where both a square/round coil and the rectangular coil is shown since both are used in this thesis) with the admissible set of ${}^l\vec{q}_n$ coordinates about a given coil location ${}^l\vec{r}_n$ defined as \mathcal{S}_n . The center of set \mathcal{S}_n is, therefore, depending on the ${}^l\vec{r}_n$ location while the size of the set is determined by the size of the magnet-array. When the edge effects of the magnet array are included in the model, the size of this set can be increased.

When assuming rigid body behavior, superposition of coil currents can be applied to obtain the total wrench on the center of mass of the translator

$${}^l\vec{w}_{tot} = \sum_{n=1}^m \vec{\gamma}_n ({}^l\vec{q}, {}^l\vec{r}_n) {}^l i_n, \quad (3.31)$$

or in matrix form

$${}^l\vec{w}_{tot} = [\vec{\gamma}_1 ({}^l\vec{q}, {}^l\vec{r}_1) \quad \cdots \quad \vec{\gamma}_{m-1} ({}^l\vec{q}, {}^l\vec{r}_{m-1}) \quad \vec{\gamma}_m ({}^l\vec{q}, {}^l\vec{r}_m)] {}^l\vec{i}, \quad (3.32)$$

where ${}^l\vec{r}_1 \cdots {}^l\vec{r}_m$ are the vectors containing the position and orientation information of each of the coils and ${}^l\vec{i}$ is a vector consisting of all active coil currents

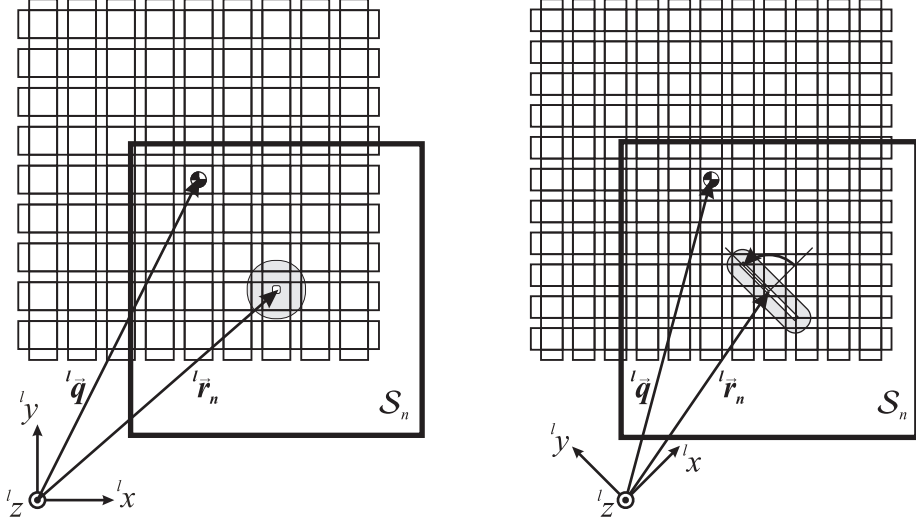


Figure 3.2. Single coil n including its admissible set of ${}^l\vec{q}$ coordinates S_n .

$i_1 \cdots i_m$. Moreover, since the vectors ${}^l\vec{r}_1 \cdots {}^l\vec{r}_m$ are constant, (3.32) can be simplified to

$$\boxed{{}^l\vec{w}_{tot} = \vec{\Gamma}({}^l\vec{q}) {}^l\vec{i}}. \quad (3.33)$$

The set S_{adm} of admissible coordinates ${}^l\vec{q}$ for the basic configuration of active coils described by (3.33) then becomes $S_{adm} = \bigcap_{n=1}^m S_n$. The previous implies that, because all individual coils $n = 1 \cdots m$ should be in their respective admissible sets S_n , the admissible set of a group of active coils S_{adm} becomes smaller when the amount of active coils becomes larger. An example of a basic configuration of active square coils is shown in figure 3.3 in grey. The figure also shows the individual admissible sets S_n of each coil. Moreover, the union of all these individual admissible sets defined as S_{adm} , which can be seen as the set of coordinates for which all individual coil models are valid, is indicated in grey.

3.3 Direct wrench-current decoupling

The model derived in section 3.2 can be used for commutation purposes (as described in section 2.1) where the system is now structured according to figure 3.4.

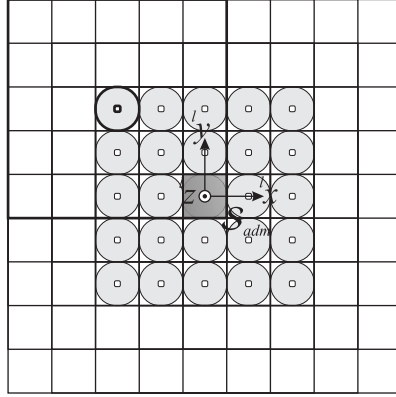


Figure 3.3. Basic configuration using square coils with its admissible set S_{adm} of ${}^l x$ and ${}^l y$ coordinates (in grey). The individual admissible sets of each coil S_n are also shown, where for illustrative purposes the individual set of the (bold) top left coil S_1 is indicated with the thick lines.

The mapping $\Gamma ({}^l \vec{q})$ has become linear with respect to the current vector \vec{i} .

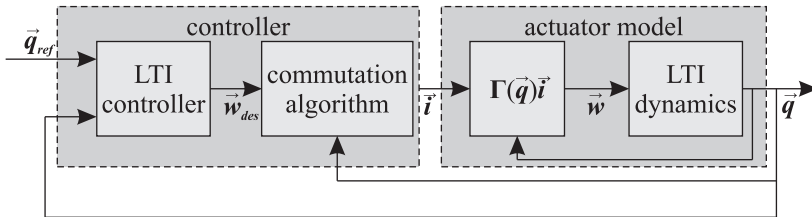


Figure 3.4. Simplified basic control configuration.

A possible method to linearize and decouple the planar actuator is to use an inverse mapping of (3.33). The following results (until equation (3.39)) are identical to [36] but have been derived independently and in parallel by us. Nevertheless, the derivation presented below is slightly different from [36] which uses Lagrange multipliers. As the set of equations described by (3.33) is under-determined (there are less DOF's than active coils) it is possible to impose extra constraints to the system. An interesting additional constraint is to minimize the sum of the ohmic losses

in the coils

$$\min_{\Gamma({}^l\vec{q})} \left\| {}^l\vec{i} \right\|_{\mathbf{R}}^2 = \left\| \Gamma^{-1}({}^l\vec{q}) {}^l\vec{w}_{des} \right\|_{\mathbf{R}}^2 \quad \forall {}^l\vec{q} \in \mathcal{S}_{adm}, \quad (3.34)$$

where the ohmic losses are described by $\left\| {}^l\vec{i} \right\|_{\mathbf{R}}^2$ which is the squared weighted 2-norm of the active current vector $\left({}^l\vec{i}^T \mathbf{R} {}^l\vec{i} \right)$ where \mathbf{R} is a diagonal weighting matrix of which the elements correspond to the resistances of each active coil. The matrix $\Gamma^{-1}({}^l\vec{q})$ is a reflexive generalized inverse of $\Gamma({}^l\vec{q})$ [37]. Specifically, we make use of the following result

Lemma 3.1. *Let $\|\vec{x}\|_{\mathbf{N}} := \sqrt{\vec{x}^H \mathbf{N} \vec{x}}$, be a (weighted) norm on \vec{x} where $\mathbf{N} \succ \mathbf{0}$ and let $\mathbf{A}\vec{x} = \vec{y}$. Suppose \mathbf{A} has full row rank. Then there exists a linear map \mathbf{A}^- such that*

$$\min_{\mathbf{A}\vec{x}=\vec{y}} \|\vec{x}\|_{\mathbf{N}} = \|\mathbf{A}^- \vec{y}\|_{\mathbf{N}}. \quad (3.35)$$

This map is given by

$$\mathbf{A}^- = \mathbf{N}^{-1} \mathbf{A}^H (\mathbf{A} \mathbf{N}^{-1} \mathbf{A}^H)^{-1}, \quad (3.36)$$

and satisfies $\mathbf{A} \mathbf{A}^- = \mathbf{I}$, $\mathbf{A} \mathbf{A}^- \mathbf{A} = \mathbf{A}$, $(\mathbf{A}^- \mathbf{A})^H \mathbf{N} = \mathbf{N} \mathbf{A}^- \mathbf{A}$ and is called the (weighted) minimum norm reflexive generalized inverse (or weak generalized inverse) of \mathbf{A} .

Proof. The proof is given in [37, section 3.1, theorem 3.1.3]□

The solution to minimization problem (3.34) can be found using lemma 3.1. The dimensions of Γ are $\#DOF \times \#\text{coils}$ so the rank of matrix Γ should equal the amount of DOF for the system of equations to be consistent. Furthermore, \mathbf{R} is a diagonal matrix so the condition $\mathbf{R} \succ \mathbf{0}$ holds since all coil resistances are larger than zero. Therefore,

$$\Gamma^{-1}({}^l\vec{q}) = \mathbf{R}^{-1} \Gamma^T({}^l\vec{q}) \left(\Gamma({}^l\vec{q}) \mathbf{R}^{-1} \Gamma^T({}^l\vec{q}) \right)^{-1} \quad \forall {}^l\vec{q} \in \mathcal{S}_{adm}. \quad (3.37)$$

When assuming all resistances to be equal to R_L (and positive) (3.34) simplifies to

$$\min_{\Gamma({}^l\vec{q})} R_L \left\| {}^l\vec{i} \right\|^2 = R_L \left\| \Gamma^{-1}({}^l\vec{q}) {}^l\vec{w}_{des} \right\|^2 \quad \forall {}^l\vec{q} \in \mathcal{S}_{adm}, \quad (3.38)$$

and (3.37) simplifies to

$$\Gamma^{-1}({}^l\vec{q}) = \Gamma^T({}^l\vec{q}) \left(\Gamma({}^l\vec{q}) \Gamma^T({}^l\vec{q}) \right)^{-1} \forall {}^l\vec{q} \in \mathcal{S}_{adm}. \quad (3.39)$$

where the solution is now independent of R_L .

3.3.1 Switching

This section shows a method which enables (in theory) unlimited stroke in the xy -plane. It is an expansion of the inverse mapping (3.39) solving minimization problem (3.38) which is defined for all ${}^l\vec{q} \in \mathcal{S}_{adm}$. When the set of admissible coordinates ${}^l\vec{q} \in \mathcal{S}_{adm}$ is large enough to form a connected set in the xy -plane, the basic configurations defined in section 3.2 can be repeated along the xy -plane to obtain a larger/infinite planar stroke.

A repeated basic configuration using square coils is shown in figure 3.5, where the dots represent the origin of local coordinate systems l which belong to each repeated basic topology (which is shown in figure 3.3). Each local coordinate system (which belongs to a state indicated by vector $\vec{\alpha}$) has its own set of desired admissible coordinates $\mathcal{S}_{\vec{\alpha}}$ which should be $\mathcal{S}_{\vec{\alpha}} \subseteq \mathcal{S}_{adm}$ to be able to form a connected set of coordinates in the xy -plane. However, when the desired stroke is larger than

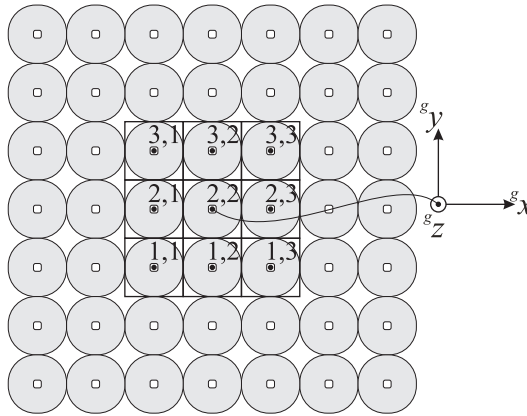


Figure 3.5. Basic square coil configuration repeated in the xy -plane.

one of the admissible sets ${}^l\vec{q} \in \mathcal{S}_{\vec{\alpha}}$ additional constraints are necessary to derive

a commutation algorithm. To derive these additional constraints it is necessary to introduce the voltage equations of the ironless moving-magnet planar actuator

$${}^g\vec{u} = {}^g\mathbf{R}{}^g\vec{i} + {}^g\mathbf{L}\frac{d{}^g\vec{i}}{dt} + \frac{d{}^g\vec{\Lambda}_m({}^g\vec{q})}{dt} = {}^g\mathbf{R}{}^g\vec{i} + {}^g\mathbf{L}\frac{d{}^g\vec{i}}{dt} + J_{{}^g\vec{\Lambda}_m}({}^g\vec{q})\frac{d{}^g\vec{q}}{dt}, \quad (3.40)$$

where the superscript g denotes the global coordinate system, ${}^g\vec{\lambda}_{pm}$ is the vector containing the flux linkage of the flux caused by the permanent magnets linked with the stator coils, $J_{{}^g\vec{\Lambda}_m}$ is the Jacobian of the flux linkage with respect to the position and orientation of the permanent-magnet array in global coordinates. The global coordinate frame g is introduced to keep track of the global position of the magnet array with respect to the repeating coil structure in local coil coordinates (e.g. see figure 3.5 which shows the global coordinates for the square coil topology and the centers of the nine local coordinate systems which are indicated by the dots). The second term of equation 3.40 depends on the time derivative of the currents. Therefore, since the amplifiers which are used to control the currents through the coils have a limited voltage range, the current waveforms must be continuous and have a limited time derivative.

Smooth position dependent weighting functions $\Delta({}^l\vec{q})$ can be added to minimization problem (3.38) to guarantee smooth currents when switching from one state to another. An example of these weighting functions is given in figure 3.6 where the weighting functions are applied to the coils at the edges of the active set of coils. In this example the diagonal weighting matrix $\Delta({}^l\vec{q})$ has the following structure

$$\Delta({}^l\vec{q}) = \Delta_x(q_x)\Delta_y(q_y), \quad (3.41)$$

where

$$\begin{aligned} \Delta_x(q_x) = \text{diag} & (\delta_{x,l}(q_x), \delta_{x,l}(q_x), \delta_{x,l}(q_x), \delta_{x,l}(q_x), \delta_{x,l}(q_x), \dots \\ & 1, \quad 1, \quad 1, \quad 1, \quad 1, \quad \dots \\ & 1, \quad 1, \quad 1, \quad 1, \quad 1, \quad \dots \\ & 1, \quad 1, \quad 1, \quad 1, \quad 1, \quad \dots \\ & \delta_{x,r}(q_x), \delta_{x,r}(q_x), \delta_{x,r}(q_x), \delta_{x,r}(q_x), \delta_{x,r}(q_x), \dots) \end{aligned} \quad (3.42)$$

with

$$\begin{aligned} \delta_{x,l}(x) &= \frac{1}{2} - \frac{1}{2} \sin\left(\frac{2}{3}\frac{\pi}{\tau}x\right), \\ \delta_{x,r}(x) &= \frac{1}{2} + \frac{1}{2} \sin\left(\frac{2}{3}\frac{\pi}{\tau}x\right), \end{aligned} \quad (3.43)$$

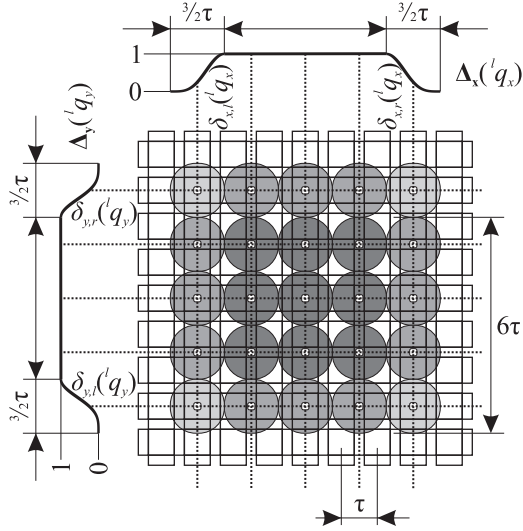


Figure 3.6. Square coil topology with smooth weighting functions.

and where

$$\mathbf{\Delta}_y(q_y) = \text{diag} \left(\begin{array}{cccc} \delta_{y,l}(q_y), & 1, & 1, & \delta_{y,r}(q_y), \dots \\ \delta_{y,l}(q_y), & 1, & 1, & \delta_{y,r}(q_y), \dots \\ \delta_{y,l}(q_y), & 1, & 1, & \delta_{y,r}(q_y), \dots \\ \delta_{y,l}(q_y), & 1, & 1, & \delta_{y,r}(q_y), \dots \\ \delta_{y,l}(q_y), & 1, & 1, & \delta_{y,r}(q_y), \dots \end{array} \right) \quad (3.44)$$

with

$$\begin{aligned} \delta_{y,l}(y) &= \frac{1}{2} - \frac{1}{2} \sin\left(\frac{2}{3} \frac{\pi}{\tau} y\right), \\ \delta_{y,r}(y) &= \frac{1}{2} + \frac{1}{2} \sin\left(\frac{2}{3} \frac{\pi}{\tau} y\right). \end{aligned} \quad (3.45)$$

Using these functions, the minimization of the squared weighted 2-norm ${}^l\vec{z}^\top \mathbf{\Delta}^{-1} ({}^l\vec{q}) {}^l\vec{z}$, which is now penalized with the inverse of the weighting matrix¹

¹With slight abuse of notation $\mathbf{\Delta}^{-1}$ is defined as the limit of the inverse of its diagonal elements, including the special case $\lim_{\delta \rightarrow 0} \frac{1}{\delta} = \infty$, where δ is a scalar on the diagonal of $\mathbf{\Delta}$ (see theorem 3.2).

$\Delta ({}^l\vec{q})$, becomes

$$\begin{aligned} & \min_{\Gamma({}^l\vec{q})} \min_{{}^l\vec{z} = {}^l\vec{w}_{des}} R_L \left\| {}^l\vec{z} \right\|_{\Delta^{-1}({}^l\vec{q})}^2 \\ & = R_L \left\| \Gamma^{-1}({}^l\vec{q}) {}^l\vec{w}_{des} \right\|_{\Delta^{-1}({}^l\vec{q})}^2 \quad \forall {}^l\vec{q} \in \mathcal{S}_{\vec{\alpha}}, \end{aligned} \quad (3.46)$$

which is now suboptimal with respect to the ohmic losses. The diagonal matrix has the following property $\Delta ({}^l\vec{q}) \succeq \mathbf{0}$. Therefore, the inverse of the diagonal weighting matrix $\Delta ({}^l\vec{q})$ is redefined as the inverse of its individual diagonal elements. Elements of the diagonal inverse matrix $\Delta^{-1} ({}^l\vec{q})$ can, therefore, also become infinitely large. Lemma 3.1 is only valid for positive definite weighting matrices and, therefore, it cannot be used directly to derive a solution to minimization problem (3.46) when one or more elements of $\vec{\delta} ({}^l\vec{q})$ are zero. The problem areas are illustrated by figure 3.7 which is an example using the square coil topology. The white coils in figure 3.7 indicate the coils which correspond to the weighting

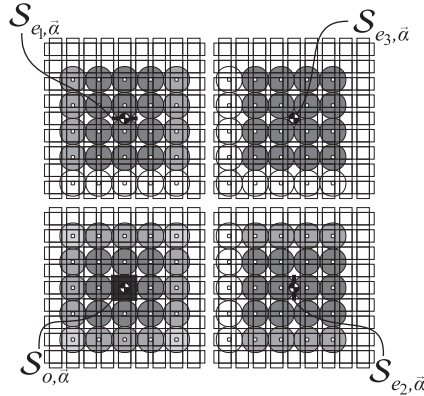


Figure 3.7. Switch areas of the square coil topology.

functions $\delta ({}^l\vec{q}) = 0$. The areas $\mathcal{S}_{o, \vec{\alpha}}$, $\mathcal{S}_{e_1, \vec{\alpha}}$, $\mathcal{S}_{e_2, \vec{\alpha}}$ and $\mathcal{S}_{e_3, \vec{\alpha}}$ correspond to the xy -coordinates associated with the respective combination of weighting functions $\delta ({}^l\vec{q}) = 0$. An additional set of constraints to the topology can be derived to assure that the solution presented by lemma 3.1 is valid to minimization problem (3.46). To arrive at a solution the admissible set of xy -coordinates $\mathcal{S}_{\vec{\alpha}}$ is split into several subsets.

Theorem 3.2. Let $\Delta (\vec{\delta} ({}^l\vec{q})) = \text{diag} (\vec{\delta} ({}^l\vec{q})) \succeq \mathbf{0}$ be a diagonal matrix, where the

real values $\delta ({}^l\vec{q})$ on the diagonal are, therefore, given by $\vec{\delta} ({}^l\vec{q}) \geq \vec{0}$. Let $\mathcal{S}_{o,\bar{\alpha}} \subset \mathcal{S}_{\bar{\alpha}}$ be an open set of admissible coordinates such that $\Delta (\vec{\delta} ({}^l\vec{q})) \succ \mathbf{0}$ (i.e. all weighting functions $\delta ({}^l\vec{q})$ are larger than zero).

Furthermore, let $\mathcal{S}_{\bar{\alpha}} = (\bigcup_{n=1}^m \mathcal{S}_{e_n,\bar{\alpha}}) \cup \mathcal{S}_{o,\bar{\alpha}}$, where m is the number of edge sets $\mathcal{S}_{e_n,\bar{\alpha}}$ and define an edge set as a connected set of admissible coordinates for which each possible switching situation results in the same combination of zero weighting functions $\delta ({}^l\vec{q})$ in $\vec{\delta} ({}^l\vec{q})$ (an example of these edge sets is given in figure 3.7). Moreover, let each edge set n have its own local reduced model $\Gamma_{e_n} ({}^l\vec{q})$, belonging to its smaller set of active coil currents corresponding to all $\delta ({}^l\vec{q})$ which are non-zero, indicated by vector ${}^l\vec{i}_{e_n}$.

Then the solution to the following minimization problem of the squared weighted 2-norm ${}^l\vec{i}^T \Delta^{-1} ({}^l\vec{q}) {}^l\vec{i}$

$$\begin{aligned} \min_{\Gamma ({}^l\vec{q}) {}^l\vec{i} = {}^l\vec{w}_{des}} R_L \left\| {}^l\vec{i} \right\|_{\Delta^{-1}(\vec{\delta}^{-1}({}^l\vec{q}))}^2 \\ = R_L \left\| \Gamma^{-} ({}^l\vec{q}, \vec{\delta} ({}^l\vec{q})) {}^l\vec{w}_{des} \right\|_{\Delta^{-1}(\vec{\delta}^{-1}({}^l\vec{q}))}^2 \quad \forall {}^l\vec{q} \in \mathcal{S}_{\bar{\alpha}}, \end{aligned} \quad (3.47)$$

which is now suboptimal with respect to the ohmic losses, becomes

$$\boxed{\Gamma^{-} ({}^l\vec{q}) = \Delta ({}^l\vec{q}) \Gamma^T ({}^l\vec{q}) \left(\Gamma ({}^l\vec{q}) \Delta ({}^l\vec{q}) \Gamma^T ({}^l\vec{q}) \right)^{-1} \quad \forall {}^l\vec{q} \in \mathcal{S}_{\bar{\alpha}}}, \quad (3.48)$$

provided that the rank of matrix $\Gamma ({}^l\vec{q})$ equals the number of DOF for all ${}^l\vec{q} \in \mathcal{S}_{o,\bar{\alpha}}$ and that the rank of each reduced model $\Gamma_{e_n} ({}^l\vec{q})$ also equals the amount of DOF for all ${}^l\vec{q}$ belonging to each corresponding ${}^l\vec{q} \in \mathcal{S}_{e_n,\bar{\alpha}}$.

Proof. Using lemma 3.1 the solution to minimization problem (3.47), excluding the edge sets, equals

$$\Gamma^{-} ({}^l\vec{q}) = \Delta ({}^l\vec{q}) \Gamma^T ({}^l\vec{q}) \left(\Gamma ({}^l\vec{q}) \Delta ({}^l\vec{q}) \Gamma^T ({}^l\vec{q}) \right)^{-1} \quad \forall {}^l\vec{q} \in \mathcal{S}_{o,\bar{\alpha}}, \quad (3.49)$$

provided that the rank of $\Gamma ({}^l\vec{q})$ equals the number of DOF and $\Delta^{-1} ({}^l\vec{q}) \succ \mathbf{0}$ for all ${}^l\vec{q} \in \mathcal{S}_{o,\bar{\alpha}}$.

The minimization problems of the edge sets can be defined as

$$\begin{aligned} \min_{\Gamma_{e_n} ({}^l\vec{q}) {}^l\vec{i}_{e_n} = {}^l\vec{w}_{des}} R_L \left\| {}^l\vec{i}_{e_n} \right\|_{\Delta_{e_n}^{-1}(\vec{\delta}_{e_n}^{-1}({}^l\vec{q}))}^2 \\ = R_L \left\| \Gamma_{e_n}^{-} ({}^l\vec{q}) {}^l\vec{w}_{des} \right\|_{\Delta_{e_n}^{-1}(\vec{\delta}_{e_n}^{-1}({}^l\vec{q}))}^2 \quad \forall {}^l\vec{q} \in \mathcal{S}_{e_n,\bar{\alpha}}, \end{aligned} \quad (3.50)$$

where $\Delta_{e_n}^{-1} \left(\vec{\delta}_{e_n}^{-1} ({}^l \vec{q}) \right) \succ \mathbf{0}$ again is a diagonal weighting matrix where the elements are given by $\vec{\delta}_{e_n}^{-1} ({}^l \vec{q})$ which are all corresponding non-zero elements of $\vec{\delta} ({}^l \vec{q})$. According to lemma 3.1, the solutions of (3.50) are given by

$$\Gamma_{e_n}^- \left({}^l \vec{q}, \vec{\delta}_{e_n} \right) = \Delta_{e_n} \left(\vec{\delta}_{e_n} \right) \Gamma_{e_n}^\top \left(\Gamma_{e_n} \Delta_{e_n} \left(\vec{\delta}_{e_n} \right) \Gamma_{e_n}^\top \right)^{-1} \forall {}^l \vec{q} \in \mathcal{S}_{e_n, \vec{\alpha}}, \quad (3.51)$$

provided that the rank of Γ_{e_n} equals the amount of DOF for all ${}^l \vec{q} \in \mathcal{S}_{e_n, \vec{\alpha}}$.

Let ${}^l \vec{i}_{e_n \mathbf{0}}$ be the vector of coils that are infinitely penalized (in the example shown in figure 3.7 this is indicated in red for each switching situation) and let $\vec{\delta}_{e_n \mathbf{0}}$ be the vector containing the corresponding weighting functions $\delta ({}^l \vec{q}) = 0$. Let the vector $\vec{\delta} \left(\vec{\delta}_{e_n}, \vec{\delta}_{e_n \mathbf{0}} \right)$ be constructed out of the elements of the vectors $\vec{\delta}_{e_n}$ and $\vec{\delta}_{e_n \mathbf{0}}$. When defining the inverse of a diagonal matrix as the inverse of its individual diagonal elements δ and using $\lim_{\delta \downarrow 0} \frac{1}{\delta} = \infty$, the following assumption can be made

$$\lim_{\vec{\delta}_{e_n \mathbf{0}} ({}^l \vec{q}) \downarrow \vec{\mathbf{0}}} \Gamma^- \left({}^l \vec{q}, \vec{\delta} \left(\vec{\delta}_{e_n}, \vec{\delta}_{e_n \mathbf{0}} \right) \right) = \Gamma^- \left({}^l \vec{q}, \vec{\delta} \left(\vec{\delta}_{e_n}, \vec{\mathbf{0}} \right) \right) \forall {}^l \vec{q} \in \mathcal{S}_{e_n, \vec{\alpha}}, \quad (3.52)$$

meaning that the limit of the weighting functions of the edge sets going to zero (resulting in an infinite penalty on the edge currents ${}^l \vec{i}_{e_n \mathbf{0}}$) should converge. Assuming that (3.52) holds, the following should also be true

$$\lim_{\vec{\delta}_{e_n \mathbf{0}} ({}^l \vec{q}) \downarrow \vec{\mathbf{0}}} \left\| \Gamma^- \left({}^l \vec{q}, \vec{\delta} \left(\vec{\delta}_{e_n}, \vec{\delta}_{e_n \mathbf{0}} \right) \right) \right\|_{\Delta^{-1} \left(\vec{\delta}^{-1} \left(\vec{\delta}_{e_n}^{-1}, \vec{\delta}_{e_n \mathbf{0}}^{-1} \right) \right)}^2 = \left\| \Gamma^- \left({}^l \vec{q}, \vec{\delta} \left(\vec{\delta}_{e_n}, \vec{\mathbf{0}} \right) \right) \right\|_{\Delta^{-1} \left(\vec{\delta}^{-1} \left(\vec{\delta}_{e_n}^{-1}, \infty \right) \right)}^2 \forall {}^l \vec{q} \in \mathcal{S}_{e_n, \vec{\alpha}}. \quad (3.53)$$

Assume that the conditions for (3.51) hold, then (3.52) holds, resulting in the follow-

ing equations

$$\begin{aligned}
& \Gamma_{e_n}(\mathbf{l}\vec{q}) \min_{\mathbf{l}\vec{i}_{e_n} = \mathbf{l}\vec{w}_{des}} R_L \left\| \mathbf{l}\vec{i}_{e_n} \right\|_{\Delta_{e_n}^{-1}(\vec{\delta}_{e_n}^{-1})}^2 = \\
& \Gamma(\mathbf{l}\vec{q}) \min_{\substack{\mathbf{l}\vec{i}_{e_n} = \mathbf{l}\vec{w}_{des} \\ \mathbf{l}\vec{i}_{e_n0} = \vec{0}}} R_L \left\| \mathbf{l}\vec{i}_{e_n} \right\|_{\Delta_{e_n}^{-1}(\vec{\delta}_{e_n}^{-1})}^2 = \\
& \lim_{\vec{\delta}_{e_n0}(\mathbf{l}\vec{q}) \downarrow \vec{0}} \min_{\Gamma(\mathbf{l}\vec{q}) \mathbf{l}\vec{i}_{e_n} = \mathbf{l}\vec{w}_{des}} R_L \left\| \mathbf{l}\vec{i}_{e_n} \right\|_{\Delta^{-1}(\vec{\delta}^{-1}(\vec{\delta}_{e_n}^{-1}, \vec{\delta}_{e_n0}^{-1}))}^2 = \\
& \lim_{\vec{\delta}_{e_n0}(\mathbf{l}\vec{q}) \downarrow \vec{0}} \left\| \Gamma^{-}(\mathbf{l}\vec{q}, \vec{\delta}_{e_n0}) \right\|_{\Delta^{-1}(\vec{\delta}^{-1}(\vec{\delta}_{e_n}^{-1}, \vec{\delta}_{e_n0}^{-1}))}^2 = \\
& \left\| \Gamma^{-}(\mathbf{l}\vec{q}, \vec{0}) \right\|_{\Delta^{-1}(\vec{\delta}^{-1}(\vec{\delta}_{e_n}^{-1}, \infty))}^2 = \\
& = \left\| \Gamma^{-}(\mathbf{l}\vec{q}, \vec{0}) \right\|_{\Delta^{-1}(\vec{\delta}^{-1}(\vec{\delta}_{e_n}^{-1}, \infty))}^2 \quad \forall \mathbf{l}\vec{q} \in \mathcal{S}_{e_n, \vec{\alpha}}.
\end{aligned} \tag{3.54}$$

Given $\mathcal{S}_{\vec{\alpha}} = (\bigcup_{n=1}^m \mathcal{S}_{e_n, \vec{\alpha}}) \cup \mathcal{S}_{o, \vec{\alpha}}$, where m is the amount of edge sets, this proofs that (3.48) is the required generalized inverse \square

The square coil topology can have an infinite stoke in the xy -plane using the derived commutation algorithm. The algorithm smoothly forces the edge currents to zero and the structure repeats itself in the xy -plane. This can also be shown by looking at the hybrid automaton [3] shown in figure 3.8 with the guards (switching conditions):

$$\begin{aligned}
\mathbf{G}_{xp, yp} &= \left\{ \left\{ \mathbf{l}q_x, \mathbf{l}q_y \right\} \in \mathbb{R}^2 \mid \mathbf{l}q_x > \frac{3}{4}\tau \wedge \mathbf{l}q_y > \frac{3}{4}\tau \right\}, \\
\mathbf{G}_{xp} &= \left\{ \left\{ \mathbf{l}q_x, \mathbf{l}q_y \right\} \in \mathbb{R}^2 \mid \mathbf{l}q_x > \frac{3}{4}\tau \wedge -\frac{3}{4}\tau < \mathbf{l}q_y \leq \frac{3}{4}\tau \right\}, \\
\mathbf{G}_{xp, yn} &= \left\{ \left\{ \mathbf{l}q_x, \mathbf{l}q_y \right\} \in \mathbb{R}^2 \mid \mathbf{l}q_x > \frac{3}{4}\tau \wedge \mathbf{l}q_y \leq -\frac{3}{4}\tau \right\}, \\
\mathbf{G}_{yn} &= \left\{ \left\{ \mathbf{l}q_x, \mathbf{l}q_y \right\} \in \mathbb{R}^2 \mid -\frac{3}{4}\tau < \mathbf{l}q_x \leq \frac{3}{4}\tau \wedge \mathbf{l}q_y \leq -\frac{3}{4}\tau \right\}, \\
\mathbf{G}_{xn, yn} &= \left\{ \left\{ \mathbf{l}q_x, \mathbf{l}q_y \right\} \in \mathbb{R}^2 \mid \mathbf{l}q_x \leq -\frac{3}{4}\tau \wedge \mathbf{l}q_y \leq -\frac{3}{4}\tau \right\}, \\
\mathbf{G}_{xn} &= \left\{ \left\{ \mathbf{l}q_x, \mathbf{l}q_y \right\} \in \mathbb{R}^2 \mid \mathbf{l}q_x \leq -\frac{3}{4}\tau \wedge -\frac{3}{4}\tau < \mathbf{l}q_y \leq \frac{3}{4}\tau \right\}, \\
\mathbf{G}_{xn, yp} &= \left\{ \left\{ \mathbf{l}q_x, \mathbf{l}q_y \right\} \in \mathbb{R}^2 \mid \mathbf{l}q_x \leq -\frac{3}{4}\tau \wedge \mathbf{l}q_y > \frac{3}{4}\tau \right\}, \\
\mathbf{G}_{yp} &= \left\{ \left\{ \mathbf{l}q_x, \mathbf{l}q_y \right\} \in \mathbb{R}^2 \mid -\frac{3}{4}\tau < \mathbf{l}q_x \leq \frac{3}{4}\tau \wedge \mathbf{l}q_y > \frac{3}{4}\tau \right\},
\end{aligned} \tag{3.55}$$

and where the reset maps which update the parameters during a switch are given

by

$$\begin{aligned}
R_{xp,yp} &= \left\{ (\{\bar{\alpha}^-\}, \{\bar{\alpha}^+\}), (\{ {}^l\bar{q}_{xy}^- \}, \{ {}^l\bar{q}_{xy}^+ \}) \mid \bar{\alpha}^-, \bar{\alpha}^+ \in \mathbb{Z}^2 \wedge \right. \\
&\quad \left. {}^l\bar{q}_{xy}^-, {}^l\bar{q}_{xy}^+ \in \mathbb{R}^2 \wedge \bar{\alpha}^+ = \bar{\alpha}^- + \begin{bmatrix} 1 \\ 1 \end{bmatrix} \wedge {}^l\bar{q}_{xy}^+ = {}^l\bar{q}_{xy}^- - \begin{bmatrix} \frac{3}{2}\tau \\ \frac{3}{2}\tau \end{bmatrix} \right\}, \\
R_{xp} &= \left\{ (\{\bar{\alpha}^-\}, \{\bar{\alpha}^+\}), (\{ {}^l\bar{q}_{xy}^- \}, \{ {}^l\bar{q}_{xy}^+ \}) \mid \bar{\alpha}^-, \bar{\alpha}^+ \in \mathbb{Z}^2 \wedge \right. \\
&\quad \left. {}^l\bar{q}_{xy}^-, {}^l\bar{q}_{xy}^+ \in \mathbb{R}^2 \wedge \bar{\alpha}^+ = \bar{\alpha}^- + \begin{bmatrix} 1 \\ 0 \end{bmatrix} \wedge {}^l\bar{q}_{xy}^+ = {}^l\bar{q}_{xy}^- - \begin{bmatrix} \frac{3}{2}\tau \\ 0 \end{bmatrix} \right\}, \\
R_{xp,yn} &= \left\{ (\{\bar{\alpha}^-\}, \{\bar{\alpha}^+\}), (\{ {}^l\bar{q}_{xy}^- \}, \{ {}^l\bar{q}_{xy}^+ \}) \mid \bar{\alpha}^-, \bar{\alpha}^+ \in \mathbb{Z}^2 \wedge \right. \\
&\quad \left. {}^l\bar{q}_{xy}^-, {}^l\bar{q}_{xy}^+ \in \mathbb{R}^2 \wedge \bar{\alpha}^+ = \bar{\alpha}^- + \begin{bmatrix} 1 \\ -1 \end{bmatrix} \wedge {}^l\bar{q}_{xy}^+ = {}^l\bar{q}_{xy}^- - \begin{bmatrix} \frac{3}{2}\tau \\ -\frac{3}{2}\tau \end{bmatrix} \right\}, \\
R_{yn} &= \left\{ (\{\bar{\alpha}^-\}, \{\bar{\alpha}^+\}), (\{ {}^l\bar{q}_{xy}^- \}, \{ {}^l\bar{q}_{xy}^+ \}) \mid \bar{\alpha}^-, \bar{\alpha}^+ \in \mathbb{Z}^2 \wedge \right. \\
&\quad \left. {}^l\bar{q}_{xy}^-, {}^l\bar{q}_{xy}^+ \in \mathbb{R}^2 \wedge \bar{\alpha}^+ = \bar{\alpha}^- + \begin{bmatrix} 0 \\ -1 \end{bmatrix} \wedge {}^l\bar{q}_{xy}^+ = {}^l\bar{q}_{xy}^- - \begin{bmatrix} 0 \\ -\frac{3}{2}\tau \end{bmatrix} \right\}, \\
R_{xn,yn} &= \left\{ (\{\bar{\alpha}^-\}, \{\bar{\alpha}^+\}), (\{ {}^l\bar{q}_{xy}^- \}, \{ {}^l\bar{q}_{xy}^+ \}) \mid \bar{\alpha}^-, \bar{\alpha}^+ \in \mathbb{Z}^2 \wedge \right. \\
&\quad \left. {}^l\bar{q}_{xy}^-, {}^l\bar{q}_{xy}^+ \in \mathbb{R}^2 \wedge \bar{\alpha}^+ = \bar{\alpha}^- + \begin{bmatrix} -1 \\ -1 \end{bmatrix} \wedge {}^l\bar{q}_{xy}^+ = {}^l\bar{q}_{xy}^- - \begin{bmatrix} -\frac{3}{2}\tau \\ -\frac{3}{2}\tau \end{bmatrix} \right\}, \\
R_{xn} &= \left\{ (\{\bar{\alpha}^-\}, \{\bar{\alpha}^+\}), (\{ {}^l\bar{q}_{xy}^- \}, \{ {}^l\bar{q}_{xy}^+ \}) \mid \bar{\alpha}^-, \bar{\alpha}^+ \in \mathbb{Z}^2 \wedge \right. \\
&\quad \left. {}^l\bar{q}_{xy}^-, {}^l\bar{q}_{xy}^+ \in \mathbb{R}^2 \wedge \bar{\alpha}^+ = \bar{\alpha}^- + \begin{bmatrix} -1 \\ 0 \end{bmatrix} \wedge {}^l\bar{q}_{xy}^+ = {}^l\bar{q}_{xy}^- - \begin{bmatrix} -\frac{3}{2}\tau \\ 0 \end{bmatrix} \right\}, \\
R_{xn,yp} &= \left\{ (\{\bar{\alpha}^-\}, \{\bar{\alpha}^+\}), (\{ {}^l\bar{q}_{xy}^- \}, \{ {}^l\bar{q}_{xy}^+ \}) \mid \bar{\alpha}^-, \bar{\alpha}^+ \in \mathbb{Z}^2 \wedge \right. \\
&\quad \left. {}^l\bar{q}_{xy}^-, {}^l\bar{q}_{xy}^+ \in \mathbb{R}^2 \wedge \bar{\alpha}^+ = \bar{\alpha}^- + \begin{bmatrix} -1 \\ 1 \end{bmatrix} \wedge {}^l\bar{q}_{xy}^+ = {}^l\bar{q}_{xy}^- - \begin{bmatrix} -\frac{3}{2}\tau \\ \frac{3}{2}\tau \end{bmatrix} \right\}, \\
R_{yp} &= \left\{ (\{\bar{\alpha}^-\}, \{\bar{\alpha}^+\}), (\{ {}^l\bar{q}_{xy}^- \}, \{ {}^l\bar{q}_{xy}^+ \}) \mid \bar{\alpha}^-, \bar{\alpha}^+ \in \mathbb{Z}^2 \wedge \right. \\
&\quad \left. {}^l\bar{q}_{xy}^-, {}^l\bar{q}_{xy}^+ \in \mathbb{R}^2 \wedge \bar{\alpha}^+ = \bar{\alpha}^- + \begin{bmatrix} 0 \\ 1 \end{bmatrix} \wedge {}^l\bar{q}_{xy}^+ = {}^l\bar{q}_{xy}^- - \begin{bmatrix} 0 \\ \frac{3}{2}\tau \end{bmatrix} \right\}.
\end{aligned} \tag{3.56}$$

The (smooth) general coordinates can be reconstructed from the local coordinates in the following way

$${}^g\bar{q}_{xy} = \frac{3}{2}\tau\bar{\alpha} + {}^l\bar{q}_{xy} + {}^q\bar{q}_{xy,0}. \tag{3.57}$$

Due to the fact that the hybrid automaton of the square coil topology shown in figure 3.8 only needs one state to obtain repetition, the use of a hybrid automaton to describe the system seems unnecessary. However, when a more complex topology is used it is a very useful tool to check the well-posedness of the switching strategy. In this case this means checking if all the switching situations can occur and prevent situations in which the system switches infinitely. To illustrate this, a topology using rectangular coils is introduced. Figure 3.9 shows the two basic configurations of ac-

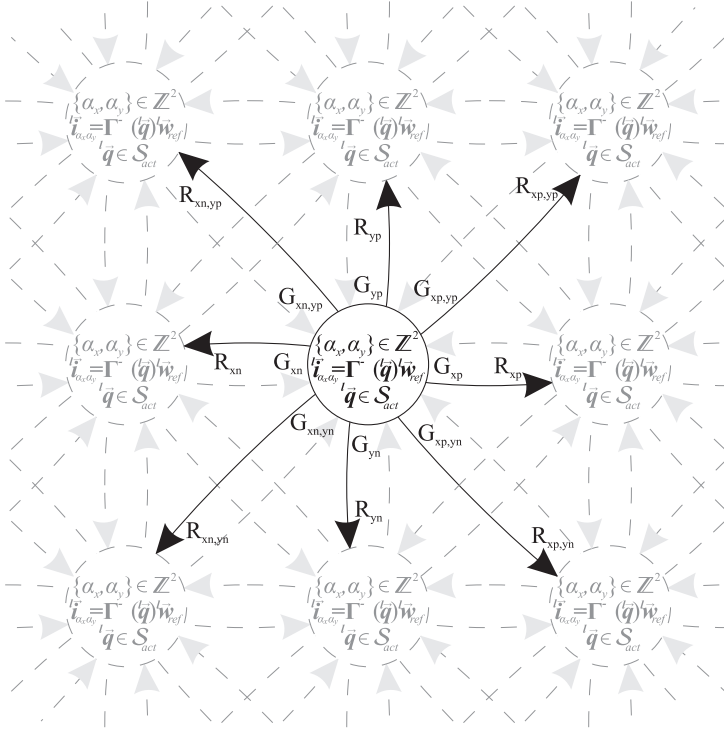


Figure 3.8. Automaton of the square coil topology.

tive rectangular coils (with their respective admissible sets of coordinates S_{adm1} and S_{adm2}) which, when combined, result in a repeatable topology. A repeated topology comprising of 84 stator coils, hereafter called the HPPA (Herringbone Pattern Planar Actuator), is shown in figure 3.10. The 84 stator coils shown in figure 3.10 result in 2×14 repeated local coil coordinate systems l of which the origins are indicated by the dots. Each local coil coordinate system is corresponding to an active coil set of 24 active stator coils (which are shown in figure 3.9). The xy -coordinates of the desired sets of admissible coordinates necessary to obtain repetition S_{odd} and S_{even} (i.e. the sets which can form a connected set of xy -coordinates as explained at the beginning of this section) are indicated in figure 3.10, where $S_{odd} \subseteq S_{adm1}$ and $S_{even} \subseteq S_{adm2}$. Again smooth switching functions $\delta(l\vec{q})$ are implemented to the edge coils of both basic HPPA topologies. The switching functions are shown in

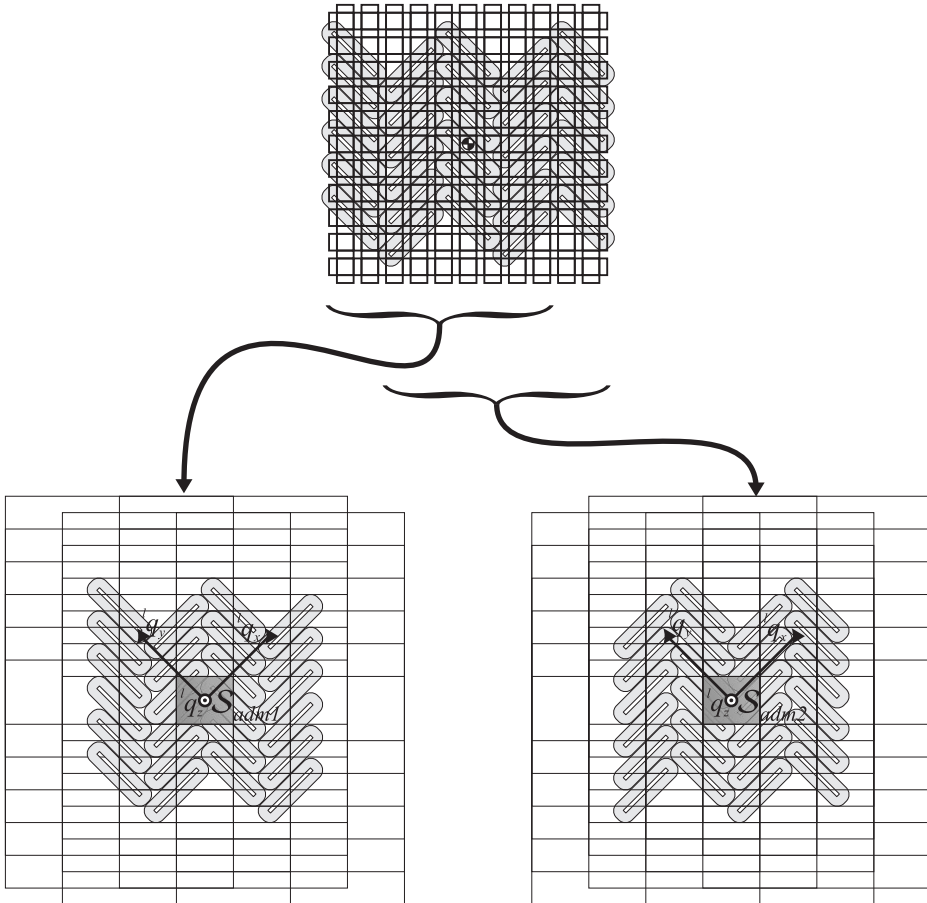


Figure 3.9. Two basic configurations (at the bottom of the picture) using rectangular coils with their admissible sets S_{adm1} and S_{adm2} of lq_x and lq_y coordinates (in grey) which, when combined, form a repeatable coil topology in the xy -plane (at the top of the picture). The individual admissible sets of each coil S_n are also shown for both basic configurations.

figure 3.12. Figure 3.13 again shows the two basic topologies with their, respective, edge configurations. There are now two optimization problems, corresponding to

the two basic configurations

$$\begin{aligned}
 & \Gamma_{odd}({}^l\bar{q}) \min_{{}^l\vec{i}_{\alpha_{odd}} = {}^l\vec{w}_{des}} R_L \left\| {}^l\vec{i}_{\alpha_{odd}} \right\|_{\Delta^{-1}(\bar{\delta}^{-1}({}^l\bar{q}))}^2 \\
 & = R_L \left\| \Gamma_{odd}^{-}({}^l\bar{q}, \bar{\delta}({}^l\bar{q})) {}^l\vec{w}_{des} \right\|_{\Delta^{-1}(\bar{\delta}^{-1}({}^l\bar{q}))}^2 \quad \forall {}^l\bar{q} \in \mathcal{S}_{\alpha_{odd}}, \\
 & \Gamma_{even}({}^l\bar{q}) \min_{{}^l\vec{i}_{\alpha_{even}} = {}^l\vec{w}_{des}} R_L \left\| {}^l\vec{i}_{\alpha_{even}} \right\|_{\Delta^{-1}(\bar{\delta}^{-1}({}^l\bar{q}))}^2 \\
 & = R_L \left\| \Gamma_{even}^{-}({}^l\bar{q}, \bar{\delta}({}^l\bar{q})) {}^l\vec{w}_{des} \right\|_{\Delta^{-1}(\bar{\delta}^{-1}({}^l\bar{q}))}^2 \quad \forall {}^l\bar{q} \in \mathcal{S}_{\alpha_{even}},
 \end{aligned} \tag{3.58}$$

which, according to (3.48), have the following two solutions

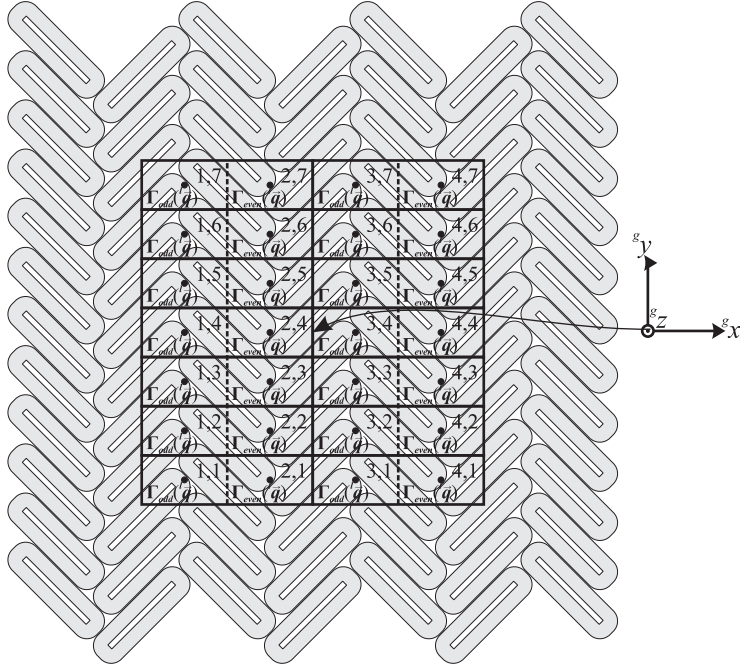


Figure 3.10. Herringbone Pattern Planar Actuator (HPPA) comprising of basic rectangular coil configurations (as shown in figure 3.9) repeated in the xy -plane.

$$\begin{aligned}
& \Gamma_{odd}^{-}({}^l\vec{q}) = \\
& \Delta({}^l\vec{q}) \Gamma_{odd}^{\top}({}^l\vec{q}) \left(\Gamma_{odd}({}^l\vec{q}) \Delta({}^l\vec{q}) \Gamma_{odd}^{\top}({}^l\vec{q}) \right)^{-1} \forall {}^l\vec{q} \in \mathcal{S}_{\vec{\alpha}_{odd}}, \\
& \Gamma_{even}^{-}({}^l\vec{q}) = \\
& \Delta({}^l\vec{q}) \Gamma_{even}^{\top}({}^l\vec{q}) \left(\Gamma_{even}({}^l\vec{q}) \Delta({}^l\vec{q}) \Gamma_{even}^{\top}({}^l\vec{q}) \right)^{-1} \forall {}^l\vec{q} \in \mathcal{S}_{\vec{\alpha}_{even}}.
\end{aligned} \tag{3.59}$$

The automaton corresponding to the HPPA (which contains two states) is given by figure 3.11.

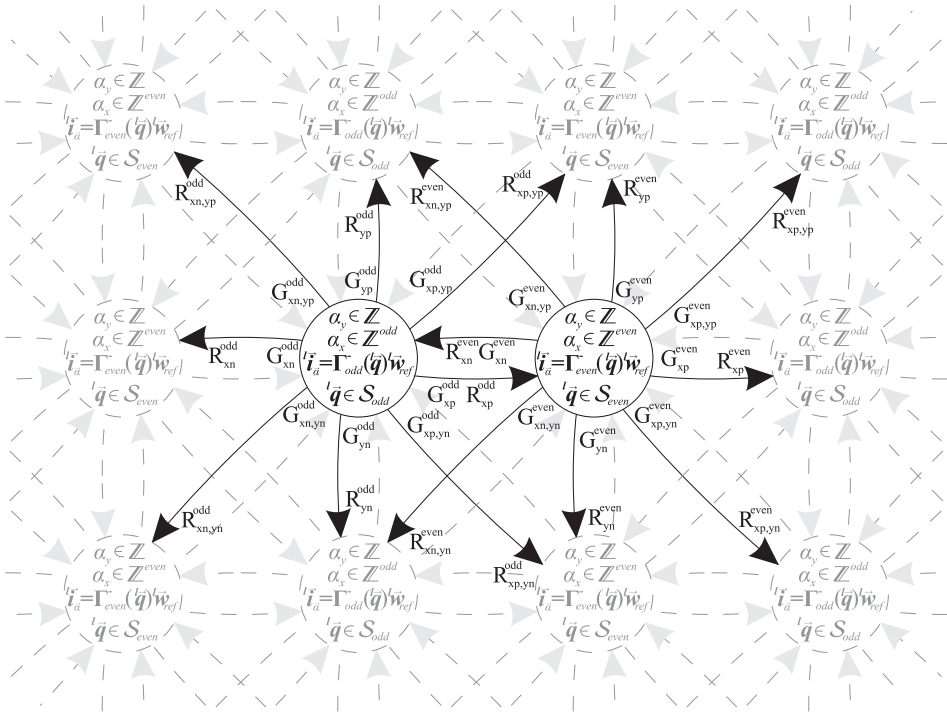


Figure 3.11. Automaton of the HPPA topology.

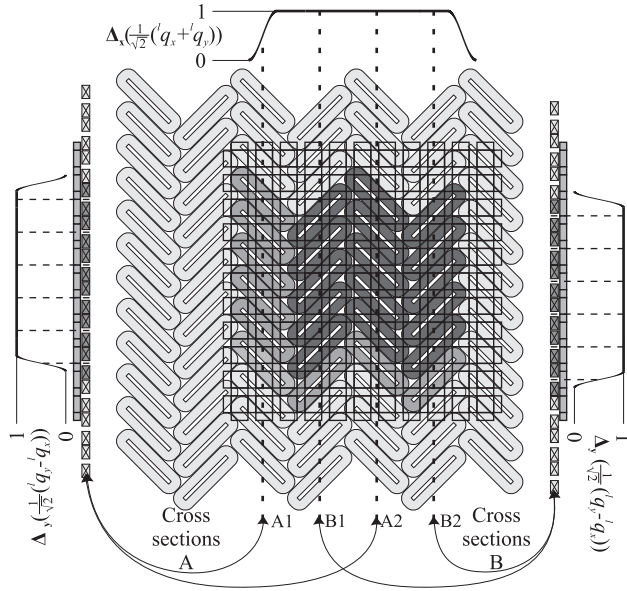


Figure 3.12. HPPA topology with smooth weighting functions.

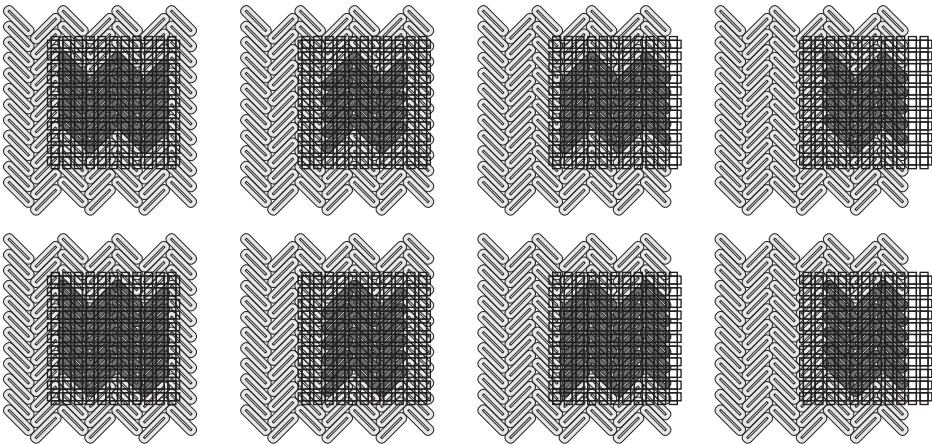


Figure 3.13. Switch areas of the HPPA topology.

3.4 Force and torque decomposition

This section links the direct wrench-current decoupling to the traditional $dq0$ transformation described in chapter 2. The reason for this is that the decomposition which links the direct wrench-current decoupling to the $dq0$ transformation results in useful design criteria with respect to performance as well as controllability.

First, the solution to minimization problem (3.47) is recalled

$$\Gamma^- ({}^l\vec{q}) = \Delta \Gamma^\top \left(\Gamma \Delta \Gamma^\top \right)^{-1} \forall {}^l\vec{q} \in \mathcal{S}_{\vec{\alpha}}, \quad (3.60)$$

where for notational simplicity the position dependency (${}^l\vec{q}$) has been neglected in this section. When the wrench vector is split in the force and the torque components the following equations can be defined

$$\vec{w} = \Gamma {}^l\vec{i} = \begin{bmatrix} \vec{F} \\ \vec{T} \end{bmatrix} = \begin{bmatrix} \Gamma_F \\ \Gamma_T \end{bmatrix} {}^l\vec{i}, \quad (3.61)$$

where (3.60) can be rewritten as

$$\Gamma^- ({}^l\vec{q}) = \Delta \begin{bmatrix} \Gamma_F^\top & \Gamma_T^\top \end{bmatrix} \begin{bmatrix} \Gamma_F \Delta \Gamma_F^\top & \Gamma_F \Delta \Gamma_T^\top \\ \Gamma_T \Delta \Gamma_F^\top & \Gamma_T \Delta \Gamma_T^\top \end{bmatrix}^{-1} \forall {}^l\vec{q} \in \mathcal{S}_{\vec{\alpha}}. \quad (3.62)$$

Using the Schur complement (see appendix A) it is possible to calculate the inverse of the partitioned matrix resulting in the following solution

$${}^l\vec{i} = \Gamma_T^- \vec{T}_{des} + (\mathbf{I} - \Gamma_T^- \Gamma_T) \Gamma_F^- \vec{F}_{des}, \quad (3.63)$$

with

$$\Gamma_F^- = \Delta \Gamma_F^\top \left(\Gamma_F \Delta \Gamma_F^\top \right)^{-1}, \quad (3.64)$$

$$\Gamma_T^- = \Phi^- \Gamma_T^\top \left(\Gamma_T \Phi^- \Gamma_T^\top \right)^{-1}, \quad (3.65)$$

$$\Phi^- = (\mathbf{I} - \Gamma_F^- \Gamma_F) \Delta, \quad (3.66)$$

provided that $\Gamma_F \Delta \Gamma_F^\top$ and $\Gamma_T \Phi^- \Gamma_T^\top$ are nonsingular. Moreover, equation (3.63) can be seen as the solution of the following two minimization problems

$$\min_{\Gamma_F {}^l\vec{i} = {}^l\vec{F}_{des}} R_L \left\| {}^l\vec{i} \right\|_{\Delta^{-1}}^2 = R_L \left\| \Gamma_F^- {}^l\vec{F}_{des} \right\|_{\Delta^{-1}}^2 \forall {}^l\vec{q} \in \mathcal{S}_{\vec{\alpha}}, \quad (3.67)$$

$$\min_{\Gamma_{\mathbf{T}} \vec{i} = {}^l \vec{T}_{des}} R_L \left\| {}^l \vec{i} \right\|_{\Phi}^2 = R_L \left\| \Gamma_{\mathbf{T}}^{-1} {}^l \vec{T}_{des} \right\|_{\Phi}^2 \quad \forall {}^l \vec{q} \in \mathcal{S}_{\vec{\alpha}}, \quad (3.68)$$

where the currents as a result of the reference force minimization are projected onto the null-space of the torque solution. Solution (3.63) can be split into three parts

- Firstly,

$${}^l \vec{i}_{\mathbf{F}} = \Gamma_{\mathbf{F}}^{-1} \vec{F}_{des}, \quad (3.69)$$

describes the currents ${}^l \vec{i}_{\mathbf{F}}$ which cause a reference force \vec{F}_{des} . Equation (3.69) provides a solution to minimization problem (3.67). Moreover, when all currents are equally penalized (i.e. $\Delta = \mathbf{I}$), the basic topology consists of a group of basic forces (as described in section 2.4) and when the angles are defined as $\phi = -\pi/4$ or 0 (depending on the topology) and $\psi = \theta = 0$ the solution given by (3.69) is equal to the sum of the basic forcer solutions obtained when applying the $dq0$ transformation described in chapter 2. The equality is obtained since in the special cases described in section 2.4 the $dq0$ transformation can be seen as a constrained minimization of the ohmic losses of a basic forcer. When the same constraints of the $dq0$ transformation are met by (3.67) (e.g. equally penalized coils consisting of a group of basic forcers with $\phi = -\pi/4$ or 0 and $\psi = \theta = 0$) the solution is equivalent.

An example of a group of four by four square coils, which is shown in figure 3.14, is used to illustrate the equivalence. When assuming $\psi = \theta =$

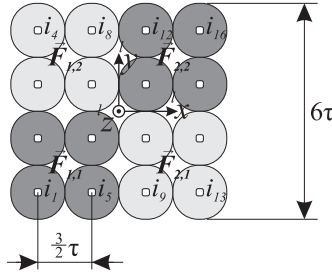


Figure 3.14. A basic topology consisting of four basic forcers (top view without translator).

$\phi = 0$, $\Gamma_{\mathbf{F}}$ can be scaled as follows

$$\Gamma_{\mathbf{F}}^{\#} ({}^l q_x, {}^l q_y) = \Lambda^{-1} ({}^l q_z) \Gamma_{\mathbf{F}}, \quad (3.70)$$

where

$$\mathbf{\Lambda}^{-1}(lq_z) = \frac{\tau}{\pi} \frac{1}{\lambda_{pm}} \exp\left(\frac{\sqrt{2}\pi l q_z}{\tau}\right) \begin{bmatrix} 1 & 0 & 0 \\ 0 & 1 & 0 \\ 0 & 0 & \frac{\sqrt{2}}{2} \end{bmatrix}, \quad (3.71)$$

is derived using (2.48). The solution to minimization problem (3.67) (using $\mathbf{\Delta} = \mathbf{I}$) then simplifies to

$$\begin{aligned} \mathbf{\Gamma}_{\mathbf{F}}^{-} &= \mathbf{\Gamma}_{\mathbf{F}}^{\#-}(lq_x, lq_y) \mathbf{\Lambda}^{-1}(lq_z) \\ &= \mathbf{\Gamma}_{\mathbf{F}}^{\#\top}(lq_x, lq_y) \left(\mathbf{\Gamma}_{\mathbf{F}}^{\#}(lq_x, lq_y) \mathbf{\Gamma}_{\mathbf{F}}^{\#\top}(lq_x, lq_y) \right)^{-1} \mathbf{\Lambda}^{-1}(lq_z) \\ &= \mathbf{\Gamma}_{\mathbf{F}}^{\#\top}(lq_x, lq_y) \begin{bmatrix} \frac{1}{4} & 0 & 0 \\ 0 & \frac{1}{4} & 0 \\ 0 & 0 & \frac{1}{4} \end{bmatrix} \mathbf{\Lambda}^{-1}(lq_z), \end{aligned} \quad (3.72)$$

which can be explained by the fact that after normalization the matrix $\mathbf{\Gamma}_{\mathbf{F}}^{\#}$ can be split into four identical orthonormal matrices (which have the property that $\mathbf{\Lambda}^{-1} = \mathbf{\Lambda}^{\top}$) belonging to the four forcers. The factors $\frac{1}{4}$ result from the fact that each forcer delivers one fourth of the total force. Moreover, in this case (since the forcers are all equally distributed) the system simplifies even further into

$$\begin{aligned} \mathbf{\Gamma}_{\mathbf{F}}^{-} &= \mathbf{\Gamma}_{\mathbf{F}}^{\#\top}(lq_x, lq_y) \begin{bmatrix} \frac{1}{4} & 0 & 0 \\ 0 & \frac{1}{4} & 0 \\ 0 & 0 & \frac{1}{4} \end{bmatrix} \mathbf{\Lambda}^{-1}(lq_z) \\ &= \begin{bmatrix} 1 & 0 & 1 & 0 & 0 & 0 & 0 & 0 & 1 & 0 & 1 & 0 & 0 & 0 & 0 & 0 \\ 0 & 0 & 0 & 0 & 1 & 0 & 1 & 0 & 0 & 0 & 0 & 0 & 1 & 0 & 1 & 0 \\ 0 & 1 & 0 & 1 & 0 & 0 & 0 & 0 & 0 & 1 & 0 & 1 & 0 & 0 & 0 & 0 \\ 0 & 0 & 0 & 0 & 0 & 1 & 0 & 1 & 0 & 0 & 0 & 0 & 0 & 1 & 0 & 1 \end{bmatrix} \\ &\quad \cdot {}^{efgh}\mathbf{T}_{dq_x q_y \mathbf{0}}(lq_x - c_x, lq_y - c_y) \begin{bmatrix} 0 & 0 & -\frac{1}{4} \\ \frac{1}{4} & 0 & 0 \\ 0 & \frac{1}{4} & 0 \\ 0 & 0 & 0 \end{bmatrix} \mathbf{\Lambda}^{-1}(lq_z), \end{aligned} \quad (3.73)$$

where ${}^{efgh}\mathbf{T}_{dq_x q_y \mathbf{0}}$ is derived in section 2.4 and where c_x and c_y are constant position offsets to match both coordinate systems.

In case of the two basic HPPA topologies (shown in figure 3.9), the result can be derived in a similar way, where

$$\mathbf{\Lambda}^{-1}(lq_z) = \frac{2}{3} \frac{\tau_n}{\pi} \frac{1}{\lambda_{pm}} \exp\left(\frac{\pi l q_z}{\tau_n}\right) \begin{bmatrix} 1 & 0 & 0 \\ 0 & 1 & 0 \\ 0 & 0 & 1 \end{bmatrix}, \quad (3.74)$$

can be derived using (2.51). The solution to minimization problem (3.67) (using $\Delta = \mathbf{I}$) then simplifies to

$$\begin{aligned}
 \Gamma_{\mathbf{F}}^{-} &= \Gamma_{\mathbf{F}}^{\#-} ({}^l q_x, {}^l q_y) \Lambda^{-1} ({}^l q_z) \\
 &= \Gamma_{\mathbf{F}}^{\#\top} ({}^l q_x, {}^l q_y) \left(\Gamma_{\mathbf{F}}^{\#} ({}^l q_x, {}^l q_y) \Gamma_{\mathbf{F}}^{\#\top} ({}^l q_x, {}^l q_y) \right)^{-1} \Lambda^{-1} ({}^l q_z) \\
 &= \Gamma_{\mathbf{F}}^{\#\top} ({}^l q_x, {}^l q_y) \Lambda^{-1} ({}^l q_z) \begin{bmatrix} \frac{1}{4} & 0 & 0 \\ 0 & \frac{1}{4} & 0 \\ 0 & 0 & \frac{1}{8} \end{bmatrix}.
 \end{aligned} \tag{3.75}$$

which can be explained by looking at figure 3.9, where for each of the two basic topologies there are four groups of forcers which can produce force in the xz -plane, and four forcers which can produce force in the yz -plane, respectively, resulting in the factors $\frac{1}{4}$ in the x - and y -directions and a factor $\frac{1}{8}$ in the z -direction.

- Secondly,

$$\boxed{{}^l \vec{i}_{T_0 F} = -\Gamma_{\mathbf{T}}^{-} \Gamma_{\mathbf{T}} \Gamma_{\mathbf{F}}^{-} \vec{F}_{des}}, \tag{3.76}$$

describes the currents ${}^l \vec{i}_{T_0 F}$ which correct for the unwanted disturbance torque, due to the force distribution over the translator, without producing any additional force components. Ideally, these currents should be zero since this is an unwanted effect. However, in moving-magnet planar actuators this is not possible due to the variable torque arm. A good design criteria is to keep this term as small as possible (especially with respect to a pure lifting force). The 2-norm of this term is a good design criteria. The 2-norm will increase, for acceleration forces in the xy -plane, when the height (in the z direction) of the mass center point of the translator is increased. Therefore, a good design criteria is to keep the 2-norm of this terms small with respect to the 2-norm of the first term discussed above.

- Lastly,

$${}^l \vec{i}_{\mathbf{T}} = \Gamma_{\mathbf{T}}^{-} \vec{T}_{des}, \tag{3.77}$$

describes the currents ${}^l \vec{i}_{\mathbf{T}}$ which cause a desired reference torque \vec{T}_{des} and no force.

Chapter 4

Design of controllable topologies

4.1 Introduction

An interesting challenge in designing a moving-magnet planar actuator is the design of the coil layout in the stator plane while keeping the controllability in mind. This chapter makes use of the direct wrench-current decoupling of chapter 3 as well as the $dq0$ transformation derived in chapter 2 to verify the controllability of a design. Part of the design method and some of the resulting topologies have been patented [21] and published [44, 42, 19, 45].

In section 4.2, the notion of (state) controllability is introduced and applied to the planar actuator models. In section 4.3 the theory is expanded to get a better idea of the quality of the derived design with respect to the error sensitivity of the decoupling algorithm. Section 4.4 applies the theory derived in sections 4.2 and 4.3 to the square coil topology and the HPPA (Herringbone Pattern Planar Actuator). Section 4.5 shows how to calculate the worst case (smallest) acceleration levels which can be obtained in the xy -plane for a given design, decoupling and maximum current specification.

4.2 State controllability conditions of a planar actuator

Throughout this chapter the notion of controllability is used. Therefore, first an introduction about the notion of (state) controllability (supposing that you know/can measure the states) is given

Definition 4.1. State controllability. (*S. Skogestad et al. [38, definition 4.1]*) The dynamical system $\dot{\vec{x}} = \mathbf{A}\vec{x} + \mathbf{B}\vec{u}$, or equivalently the pair (\mathbf{A}, \mathbf{B}) , is said to be state controllable if, for any initial state $\vec{x}(0) = \vec{x}_0$, any time $t_1 > 0$ and any final state \vec{x}_1 , there exists an input $\vec{u}(t)$ such that $\vec{x}(t_1) = \vec{x}_1$. Otherwise the system is said to be uncontrollable.

The system (\mathbf{A}, \mathbf{B}) is state controllable if and only if the controllability matrix

$$\mathbf{C} = [\mathbf{B} \quad \mathbf{A}\mathbf{B} \quad \mathbf{A}^2\mathbf{B} \quad \dots \quad \mathbf{A}^{n-1}\mathbf{B}], \quad (4.1)$$

has rank n (full row rank) where n is the number of states.

Definition 4.2. The planar actuators considered are a class of nonlinear systems which can be defined as a combination of a linear system (\mathbf{A}, \mathbf{B}) with an additional input mapping which is linear with respect to the current input vector ${}^l\vec{i}$, but nonlinear with respect to the position and orientation vector ${}^l\vec{q}$

$$\dot{\vec{x}} = \mathbf{A}\vec{x} + \mathbf{B}{}^l\vec{w}, \quad (4.2)$$

$$\vec{x} = [{}^l\vec{q}^\top \quad {}^l\dot{\vec{q}}^\top]^\top, \quad (4.3)$$

$${}^l\vec{w} = \mathbf{\Gamma}({}^l\vec{q}) {}^l\vec{i}, \quad (4.4)$$

$$(4.5)$$

where ${}^l\vec{w} = [{}^l\vec{F}^\top \quad {}^l\vec{T}^\top]^\top$ is the wrench vector consisting of the force and torque components on the mass center point of the translator (which is considered to be a rigid body). With the system matrices

$$\mathbf{A} = \begin{bmatrix} \mathbf{0} & \mathbf{I} \\ \mathbf{0} & \mathbf{0} \end{bmatrix}, \quad (4.6)$$

$$\mathbf{B} = \begin{bmatrix} \mathbf{0} \\ \mathbf{M}^{-1} \end{bmatrix},$$

where \mathbf{M} is a diagonal matrix consisting of the mass and inertias corresponding to each degree of freedom.

To derive a notion of controllability of this system the following definitions are introduced.

Definition 4.3. (*H. Nijmeijer et al. [32, section 3.1]*) Let a smooth affine nonlinear

control system be given by

$$\begin{aligned}\dot{\vec{x}} &= \vec{f}(\vec{x}) + \sum_{j=1}^m \vec{g}_j(\vec{x}) u_j, \\ \vec{u} &= [u_1 \quad \cdots \quad u_m]^\top \in U \subset \mathbb{R}^m,\end{aligned}\tag{4.7}$$

where \vec{x} are local coordinates for a smooth manifold \mathcal{M} (the state space manifold), and $\vec{f}, \vec{g}_1, \dots, \vec{g}_m$ are smooth vector fields on \mathcal{M} . \vec{f} is called the drift vector field, and \vec{g}_j , the input vector fields.

Definition 4.4. Controllability (H. Nijmeijer et al. [32, definition 3.2]) The nonlinear system of definition 4.3 is called controllable if for any two points \vec{x}_1, \vec{x}_2 in \mathcal{M} there exists a finite time t_f and an admissible control function $\vec{u} : [t_0, t_f] \rightarrow U$ such that $\vec{x}(t_f, t_0, \vec{x}_1, \vec{u}) = \vec{x}_2$

The simplest approach to study controllability of the nonlinear system of definition 4.3 is to consider its linearization.

Proposition 4.5. (H. Nijmeijer et al. [32, proposition 3.3]) Consider the nonlinear system of definition 4.3, and let $\vec{x}_0 \in \mathcal{M}$ satisfy $\vec{f}(\vec{x}_0) = \vec{0}$. Furthermore, let U contain a neighborhood V of $\vec{u} = \vec{0}$. Suppose that the linearization of the nonlinear system of definition 4.3 in \vec{x}_0 and $\vec{u} = \vec{0}$

$$\begin{aligned}\dot{\vec{z}} &= J_{\vec{f}}(\vec{x})|_{\vec{x}=\vec{x}_0} \vec{z} + \sum_{j=1}^m \vec{g}_j(\vec{x}_0) v_j, \\ \vec{z} &\in \mathbb{R}^n, \vec{v} \in \mathbb{R}^m,\end{aligned}\tag{4.8}$$

is a controllable linear system (where $J_{\vec{f}}(\vec{x})$ is defined as the Jacobian of the drift vectorfield with respect to the local coordinates \vec{x} of the smooth manifold \mathcal{M}). Then for every $t_f > 0$ and $\epsilon > 0$ the set of points which can be reached from \vec{x}_0 in time t_f using admissible control functions $u(\cdot) : [0, t_f] \rightarrow V$, satisfying $\|\vec{u}(t)\| < \epsilon$, contains a neighborhood of \vec{x}_0 .

This does not imply that if the linearized system is uncontrollable, the nonlinear system is uncontrollable. However, in the case of a planar actuator, it is desirable for the system to be holonomic², which in this case means that for every admissible position it should always be possible to move in all six degrees of freedom

²An example of a non-holonomic system is a car, which cannot directly move laterally resulting in an uncontrollable linearized system, although, (fortunately) it is controllable (the proof is given in [32]).

directly. More formally it means that the kinematic constraints should only depend on time and the generalized coordinates, and they should not depend on their generalized velocities (time derivatives of the generalized coordinates) [7]. Therefore, in the case of a the planar actuator, proposition 4.5 is a useful test method.

This can be seen when applying proposition 4.5 to the planar actuator system (definition 4.2) since

$$\vec{f}(\vec{x}_0) = \vec{0}, \quad (4.9)$$

holds for all admissible coordinates because

$$\vec{f}(\vec{x}_0) = \mathbf{A}\vec{x}_0 = \begin{bmatrix} \mathbf{0} & \mathbf{I} \\ \mathbf{0} & \mathbf{0} \end{bmatrix} \begin{bmatrix} {}^l\vec{q}_0 \\ \vec{0} \end{bmatrix} = \vec{0}. \quad (4.10)$$

Moreover,

$$\mathbf{J}_{\vec{f}}(\vec{x})|_{\vec{x}=\vec{x}_0} = \mathbf{A}, \quad (4.11)$$

so \vec{z} can be substituted by \vec{x} (in (4.8)). Now (4.8) can be simplified into

$$\dot{\vec{x}} = \mathbf{A}\vec{x} + \mathbf{B}\Gamma({}^l\vec{q}_0) {}^l\vec{i}, \quad (4.12)$$

using definition 4.1 this results in the rank condition

$$\begin{aligned} & \text{rank} \left(\begin{bmatrix} \mathbf{B}\Gamma({}^l\vec{q}) & \mathbf{A}\mathbf{B}\Gamma({}^l\vec{q}) & \mathbf{A}^2\mathbf{B}\Gamma({}^l\vec{q}) & \dots & \mathbf{A}^{(2\#\text{DOF}-1)}\mathbf{B}\Gamma({}^l\vec{q}) \end{bmatrix} \right) = \\ & \text{rank} \left(\begin{bmatrix} \mathbf{0} & \mathbf{M}^{-1}\Gamma({}^l\vec{q}) \\ \mathbf{M}^{-1}\Gamma({}^l\vec{q}) & \mathbf{0} \end{bmatrix} \right) = 2\#\text{DOF} \quad \forall {}^l\vec{q} \in \mathcal{S}_{\vec{\alpha}}. \end{aligned} \quad (4.13)$$

which simplifies into the following rank condition

$$\text{rank}(\mathbf{M}^{-1}\Gamma({}^l\vec{q})) = \#\text{DOF} \quad \forall {}^l\vec{q} \in \mathcal{S}_{\vec{\alpha}}. \quad (4.14)$$

So, for the planar actuator to be (state) controllable, the matrix should have full row rank for all admissible coordinates ${}^l\vec{q} \in \mathcal{S}_{\vec{\alpha}}$. Since \mathbf{M}^{-1} is a diagonal matrix with full rank, the condition can be simplified to

$$\text{rank}(\Gamma({}^l\vec{q})) = \#\text{DOF} \quad \forall {}^l\vec{q} \in \mathcal{S}_{\vec{\alpha}}. \quad (4.15)$$

The condition derived above is the same as stating that there exists a reflexive generalized inverse which results in the following condition

$$\Gamma({}^l\vec{q})\Gamma^{-}({}^l\vec{q}) = \mathbf{I} \quad \forall {}^l\vec{q} \in \mathcal{S}_{\vec{\alpha}}, \quad (4.16)$$

which can be checked using the theory of chapter 3. Moreover, when switching is necessary to increase the stroke in the xy -plane there should exist a reflexive generalized inverse which also allows for smooth switching of the currents (as discussed in section 3.3.1).

4.3 Error sensitivity of weighted minimal norm inverses and solutions

In the introduction of this chapter the concept of controllability is introduced. The condition given by (4.16) shows a test to determine whether or not a planar actuator is controllable. However, this only provides a yes or no decision about the controllability. To compare various designs it is desirable to have a design parameter which is a measure of the controllability. A possibility is to look at how reliable the diagonalization given by (4.16) will be under uncertainties. Without knowledge of the structure of these uncertainties a qualitative indication of the decoupling can be obtained by looking at the error sensitivity of the generalized inverse which is used in the decoupling. For this reason the condition number is introduced

Definition 4.6. *With slight abuse of notation the condition number for matrix inversion with respect to the induced matrix 2-norm $\|\cdot\|$ is given by the quantity*

$$\kappa_2(\mathbf{A}^-, \mathbf{A}) \equiv \begin{cases} \|\mathbf{A}^-\| \|\mathbf{A}\|, & \text{if } \text{rank}(\mathbf{A}^-) = n \\ \infty, & \text{if } \text{rank}(\mathbf{A}^-) < n \end{cases}, \quad (4.17)$$

where the induced matrix 2-norm $\|\cdot\|$ is defined as the maximum singular value of the matrix. Matrix \mathbf{A}^- is defined as a weighted minimum norm reflexive generalized inverse of \mathbf{A} (see lemma 3.1). Where \mathbf{A} is defined as an $n \times m$ matrix where $n \leq m$.

The abuse of notation is caused by the fact that if $\|\mathbf{A}^-\| \neq \frac{1}{\sigma_{\min}(\mathbf{A})}$, where $\sigma_{\max}(\mathbf{A})$ and $\sigma_{\min}(\mathbf{A})$ are the maximum and minimum singular values of \mathbf{A} , the condition number is defined differently compared to its usual notation which is

$$\kappa_2(\mathbf{A}) \equiv \frac{\sigma_{\max}(\mathbf{A})}{\sigma_{\min}(\mathbf{A})}, \quad (4.18)$$

(which can be checked using singular value decomposition).

If $\kappa_2(\mathbf{A}^-, \mathbf{A})$ is infinitely large, the condition given by (4.16) is not met, and the system is therefore not state controllable. Moreover, the following theorem can be used to derive an upper bound on the errors resulting from a matrix inverse.

Theorem 4.7. *Let \mathbf{A} be a matrix of size $n \times m$ with $m > n$ and let \mathbf{A}^- be a weighted minimum norm reflexive generalized inverse of \mathbf{A} (see lemma 3.1). Now suppose the real system should have been*

$$(\mathbf{A} + \mathbf{E}) \hat{\mathbf{x}} = \vec{\mathbf{b}} + \vec{\mathbf{e}}, \quad (4.19)$$

instead of

$$\mathbf{A}\vec{x} = \vec{b}, \quad (4.20)$$

then for small errors $\|\mathbf{E}\| \ll \frac{\|\mathbf{A}\|}{\kappa_2(\mathbf{A})}$ an approximation of the upper bound on the relative error is given by

$$\begin{aligned} \frac{\|\hat{\vec{x}} - \vec{x}\|}{\|\vec{x}\|} &\approx \frac{\|((\mathbf{I} + \mathbf{A}^{-1}\mathbf{E})^{-1}\mathbf{A}^{-1} - \mathbf{A}^{-1})\vec{b} + (\mathbf{I} + \mathbf{A}^{-1}\mathbf{E})^{-1}\mathbf{A}^{-1}\vec{e}\|}{\|\vec{x}\|} \\ &< \kappa_2(\mathbf{A}^{-1}, \mathbf{A}) \left(\frac{\|\mathbf{E}\|}{\|\mathbf{A}\|} + \frac{\|\vec{e}\|}{\|\vec{b}\|} \right). \end{aligned} \quad (4.21)$$

Proof. The proof is given in appendix B \square

It is not useful to apply the derived theorem directly to the matrix Γ . This is caused by the fact that the vector \vec{w} , which is transformed to the desired current set-point by matrix Γ^{-1} , consists of different quantities (force and torque components) having different units (N and Nm). Therefore, scaling is very important. Especially when comparing various actuator designs. To obtain a valid result, a scaling needs to be introduced which "normalizes" the wrench vector. The first step in scaling is to use the Mass/Inertia matrix \mathbf{M}

$${}^l\ddot{\vec{q}} = \mathbf{M}^{-1}\Gamma ({}^l\vec{q}) {}^l\vec{z}, \quad (4.22)$$

resulting in the acceleration vector, which is here defined as the second time derivative of the position vector, indicated by ${}^l\ddot{\vec{q}}$. This still results in different units ($\frac{\text{m}}{\text{s}^2}$ and $\frac{\text{rad}}{\text{s}^2}$). A possible solution is to use an effective arm in order to match the different units. In this chapter the arms are chosen in such a way that the mechanical power for each degree of freedom is equally penalized

$$P_m = {}^lF_{xyz} {}^l\dot{q}_{xyz} = {}^lT_\psi {}^l\dot{q}_\psi = {}^lT_\theta {}^l\dot{q}_\theta = {}^lT_\phi {}^l\dot{q}_\phi, \quad (4.23)$$

resulting in the following effective arms

$$\begin{aligned} l_\psi &= \sqrt{\frac{I_\psi}{M}}, \\ l_\theta &= \sqrt{\frac{I_\theta}{M}}, \\ l_\phi &= \sqrt{\frac{I_\phi}{M}}, \end{aligned} \quad (4.24)$$

where M is the mass of the translator and I_ψ , I_θ and I_ϕ are the moments of inertia about the mass center point of the translator in local coil coordinates l , respectively. This results in a scaling matrix

$$\mathbf{N} = \text{diag}(1, 1, 1, l_\psi, l_\theta, l_\phi). \quad (4.25)$$

The normalized matrices $\mathbf{\Gamma}^*$ and $\mathbf{\Gamma}^{*-}$ then become

$$\begin{aligned}\mathbf{\Gamma}^* &= \mathbf{N}\mathbf{M}^{-1}\mathbf{\Gamma}, \\ \mathbf{\Gamma}^{*-} &= \mathbf{\Gamma}^{-}\mathbf{M}\mathbf{N}^{-1}.\end{aligned}\tag{4.26}$$

An approximate upper bound on the relative error of the 2-norm of the active current vector using the normalized decoupling can now be calculated by

$$\kappa_2(\mathbf{\Gamma}^{*-}, \mathbf{\Gamma}^*) \left(\frac{\|\mathbf{E}^*\|}{\|\mathbf{\Gamma}^*\|} + \frac{\|\vec{e}^*\|}{\|l\vec{q}^*\|} \right).\tag{4.27}$$

The sensitivity of the error matrix \mathbf{E} and error vector \vec{e} to real design variables is also important when comparing different designs. The sensitivity of the decoupling with respect to e.g. the position errors of the stator coil positions depends on amongst others the pole pitch τ and the amount of active coils. The relative error of the wrench also depends on the model error due to neglected higher harmonics of the magnetic flux density of the magnet array in combination with the stator coil topology itself. A fair (exact) comparison between different topologies using only the condition number is, therefore, not possible. Moreover, when more details are available about the desired trajectories and the noise distribution over the degrees of freedom, it is also possible to use (setpoint dependent) scaling factors to determine the best scaling ratios. Nevertheless, in the next section it is shown that the condition number is still a useful design parameter.

4.4 Controllable 6 DOF basic topologies

In this section the design of a basic topology is discussed which allows for the translator to be (state) controllable in six degrees of freedom over the full range of admissible coordinates.

In order to do so the example of the 4×4 square coil topology is used, which was introduced in section 3.4 (the stator coils of the basic topology are again shown in figure 4.1). It is shown that when only the force components and no switching is considered the basic topology can be expressed as four basic forcers (as defined in chapter 2). Since each of these basic forcers can produce a position independent force vector, presumably with a different effective arm, it is safe to assume that the torque components can also be controlled. Moreover, since the ohmic losses of a single basic forcer are a factor two smaller when a force in the z -direction is required compared to an equal force in the x - or y -directions it is safe to assume that it will be effective with respect to producing a levitation force.

In order to achieve long-stroke movement the switching strategy of chapter 3 can be used. Using theorem 3.2 it can be shown that in order for the system to be controllable it is necessary that the reduced matrices (at the switching boundaries) should also be properly conditioned. The basic 4×4 topology is again shown at the

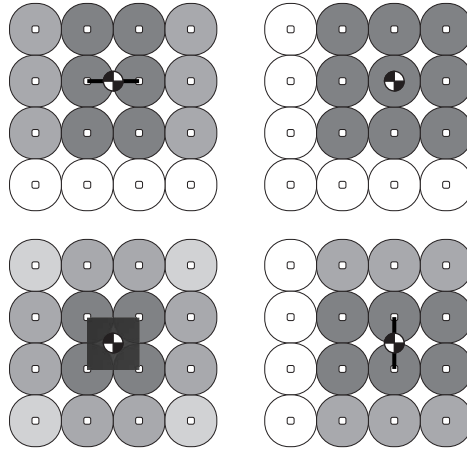


Figure 4.1. All topologies which need to be controllable for long-stroke motion including their necessary admissible sets (in black).

bottom left of figure 4.1. The other three situations show the reduced edge sets with their respective switching areas. At the switching areas the system does not consist of four basic forcers. The worst case situation (the top right situation of figure 4.1) is shown again in figure 4.2 where it is shown with two different magnet arrays. The left situation shows an uncontrollable system and the right situation shows a controllable situation. The difference between the systems is the magnet orientation with respect to the coils. In the uncontrollable case only the middle coil is located at a direct axis (capable of producing a lift force), the four corner coils are located at a zero axis (not capable of producing any force), and the other coils are located at either a q_x or a q_y quadrature axis (only capable of producing a force along the x - or y -axis, respectively). Since only one coil can produce a lift force the torque components cannot be controlled and, therefore, the nine coil topology is uncontrollable at that position. The previous can also be checked using the condition number defined by definition 4.6. When the condition number approaches infinity the system becomes uncontrollable. The force components are controllable which can be seen from the condition number plot shown in figure 4.3. The value of

the condition number only looking at the force components of this topology without switching is equal to $\sqrt{2}$ independent of position. Therefore, the condition number with switching will be $\geq \sqrt{2}$ but it should have the same order of magnitude. From figure 4.3 it can be seen that the decoupling is properly conditioned when only force components are considered. When including the torque components the total system becomes uncontrollable which can be seen from the condition number plot shown in figure 4.5 of which the condition number goes towards infinity at the edges.

The other situation (on the right in figure 4.2) has four coils located at the direct axis and four coils located at the quadrature axis and only the coil in the middle is located at a zero axis. Since there are now four coils which can produce lift, the torque components about the x - and y -axis can be controlled. The torque about the z -axis can also be controlled using the four coils which can produce a force in either the x - or y -direction. A similar analysis can be made of the other edge sets (shown in figure 4.1), which are also controllable. The condition numbers of the forces and the total system of this controllable version of the 4×4 setup are shown in figures 4.4 and 4.6, respectively.

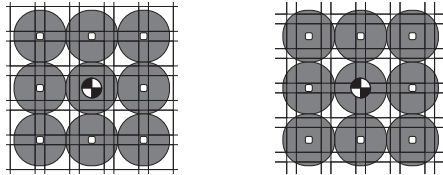


Figure 4.2. *Uncontrollable topology (left) and controllable topology (right) depending on the relative magnet-plate position.*

Another parameter which determines the degree of controllability is the weighting matrix $\Delta(\vec{q})$ which is necessary for the switching. In section 3.4 it is shown that part of the commutation of a 4×4 square coil topology can be written as four basic square coil forcers (which were defined in section 2.4). However, one of the conditions for this to hold is that there should be an equal weight applied to all individual coils. A possible method to relax this condition is to use an additional row and column of coils which results in the 5×5 basic topology which is used as an example throughout chapter 3. When the window functions (defined in section 3.3.1) which are used to weigh the currents in the decoupling are chosen symmetrically,

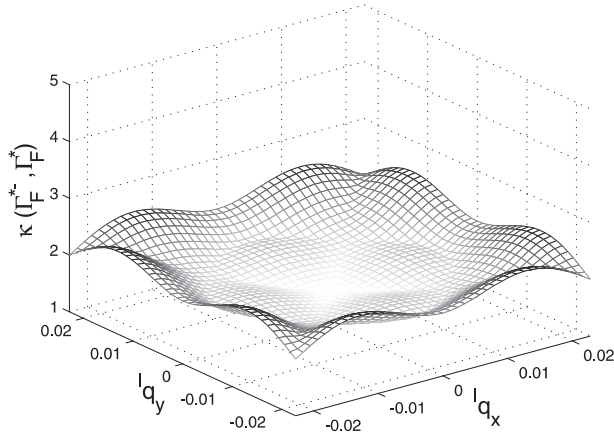


Figure 4.3. The condition number of the force decoupling applied to the square coil topology shown in figure 4.1 with the orientation of the magnet array shown at the left of figure 4.2.

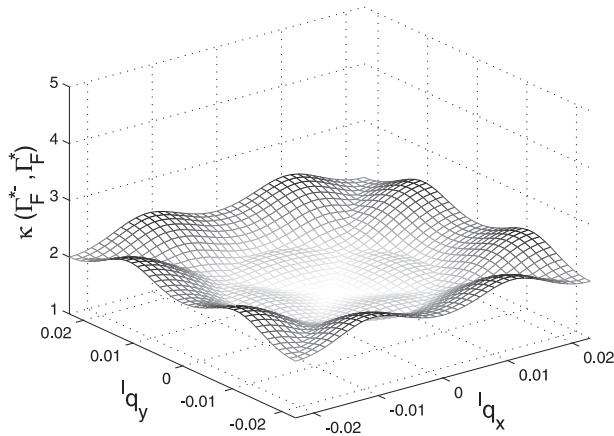


Figure 4.4. The condition number of the force decoupling applied to the square coil topology shown in figure 4.1 with the orientation of the magnet array shown at the right of figure 4.2.

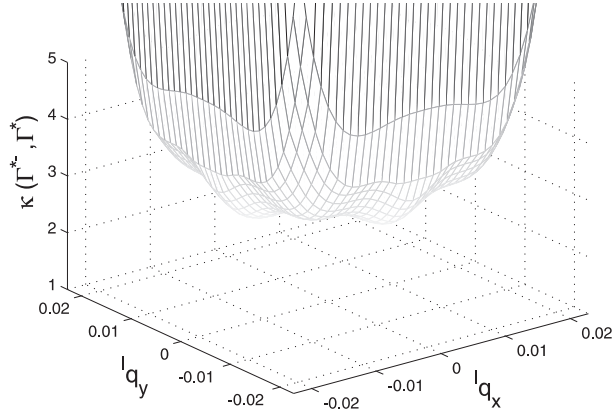


Figure 4.5. The condition number of the 6-DOF decoupling applied to the square coil topology shown in figure 4.1 with the orientation of the magnet array shown at the left of figure 4.2.

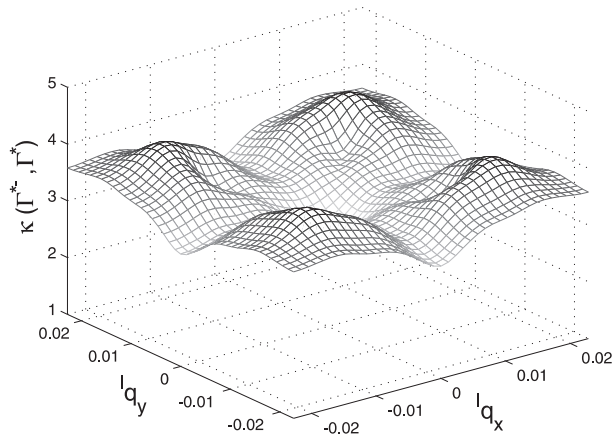


Figure 4.6. The condition number of the 6-DOF decoupling applied to the square coil topology shown in figure 4.1 with the orientation of the magnet array shown at the right of figure 4.2.

such that $\delta_l = \delta_{x,l} = \delta_{y,l}$, $\delta_r = \delta_{x,r} = \delta_{y,r}$ and $\delta_l ({}^l\vec{q}) + \delta_r ({}^l\vec{q}) = 1$, effectively the resulting system will behave like the 4×4 basic topology, resulting in

$$\begin{aligned}
 \Gamma_{\mathbf{F}}^- &= \Gamma_{\mathbf{F}}^{\#-} ({}^lq_x, {}^lq_y) \Lambda^{-1} ({}^lq_z) \\
 &= \Gamma_{\mathbf{F}}^{\#\top} ({}^lq_x, {}^lq_y) \left(\Gamma_{\mathbf{F}}^{\#} ({}^lq_x, {}^lq_y) \Gamma_{\mathbf{F}}^{\#\top} ({}^lq_x, {}^lq_y) \right)^{-1} \Lambda^{-1} ({}^lq_z) \\
 &= \Gamma_{\mathbf{F}}^{\#\top} ({}^lq_x, {}^lq_y) \begin{bmatrix} \frac{1}{4} & 0 & 0 \\ 0 & \frac{1}{4} & 0 \\ 0 & 0 & \frac{1}{4} \end{bmatrix} \Lambda^{-1} ({}^lq_z).
 \end{aligned} \tag{4.28}$$

The only property which is lost is the power invariance of the $dq0$ transformation (because $\Gamma_{\mathbf{F}}^{\#\top} ({}^lq_x, {}^lq_y)$ cannot be split into orthonormal matrices anymore) but the additional transformations which are necessary to decouple the torque components are also power variant so the property is also lost in the total 4×4 basic topology. Splitting the commutation algorithm into forces and torques only resembles to the $dq0$ transformation when the rotational angles are not taken into account. When the angles are also included in the decoupling it is not very interesting to implement the commutation by splitting it into a force vector and torque vector since the generalized inverse of the force matrix does not result in a constant diagonal matrix anymore. Actuators which only stabilize the rotations (e.g. assuming a perfect magnetic bearing) can benefit, with respect to the computational demands, from the fact that after splitting the decoupling into force and torque vectors most matrices which need to be inverted have become diagonal and position invariant. Since the amount of active coils of the 5×5 square coil topology and the HPPA topology are almost equal (25 for the square coil topology against 24 for the HPPA topology), respectively, it is interesting to compare the condition numbers of both topologies. The condition numbers of the square coils and the HPPA topology are shown in figures 4.7 and 4.8, respectively. It can be concluded from the figures that both topologies are equally well conditioned. Nevertheless, the HPPA design has less model disturbances due to smaller unmodeled higher harmonics in the flux density distribution [17] and is, therefore, more suitable for model based commutation. Moreover, when switching is ignored, the square coil topology effectively has $\frac{1}{4}$ of its coils located at a 0-axis (which means that these coils cannot be used to produce any force) and $\frac{1}{4}$ of its coils located at a d -axis. Therefore, the dissipation of the HPPA topology, which does not have its coils located at a zero axis and $\frac{1}{2}$ of its coils located at a d -axis, is lower when a pure lift force is desired, because effectively half of the coils can be used to produce lift.

The decoupling algorithm has to be implemented on a DSP. Therefore, it will have to be calculated at discrete events. In order to maintain accuracy of the decoupling at high speed the spacial derivatives of the currents must be small enough not

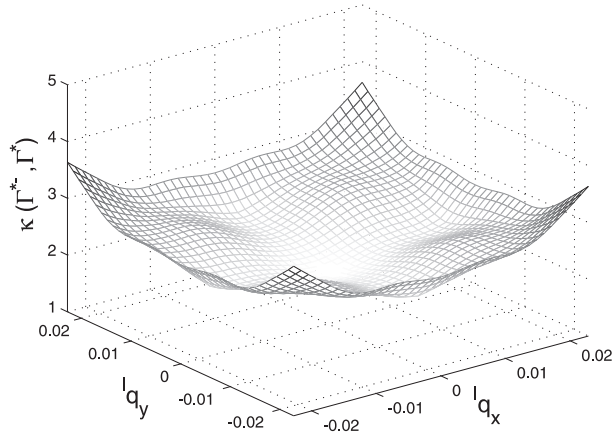


Figure 4.7. The condition number of the 6-DOF decoupling applied to the 5×5 square coil topology.

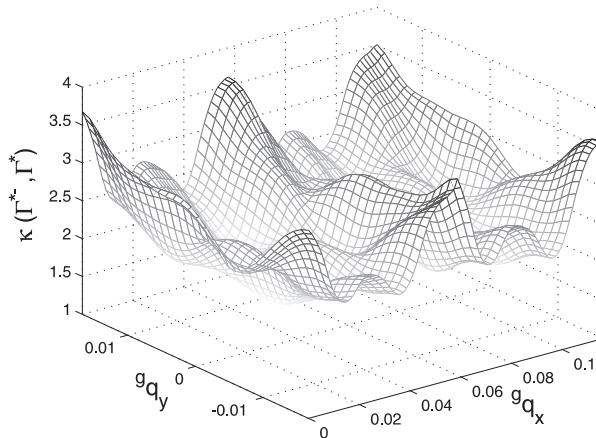


Figure 4.8. The condition number of the 6-DOF decoupling applied to the HPPA topology.

to create large decoupling errors due to sampling. Unfortunately, due to the complex torque compensation, the 6-DOF decoupling has become too complex to find an analytical solution of the inverse. Therefore, it is hard to find a simple bound of

the maximum error, although a low condition number of the decoupling will result in smaller errors due to sampling. For the HPPA prototype the sample frequency is set as large as possible. Moreover, half-order-hold is used to minimize the error. Half-order-hold makes use of the reference speed to calculate the effective position halfway the sample time (assuming a constant speed during one sample). Using this effective position, the decoupling error due to sampling can be reduced. When a sample frequency of 4KHz is used and a maximum speed of 1m/s the maximum position steps due to sampling are $250\mu\text{m}$, resulting in a maximum error of the position used in the decoupling of $125\mu\text{m}$ when using half-order-hold, which is the same order of magnitude as the design accuracy of the stator and translator.

4.5 Worst-case force components

Due to the constant levitation force and the non-linear decoupling it is hard to find the maximum acceleration specifications due to actuator constraints. This section focusses on the worst-case (smallest) acceleration specification which can be achieved in the xy -plane when using the direct wrench-current decoupling of chapter 3.

When the actuator is considered in its working point, which in the HPPA case means a clearance of $q_z = 1\text{ mm}$, and the following orientations $\phi = -\pi/4\text{ rad}$ and $\psi = \theta = 0\text{ rad}$, it is possible to determine the large signal bounds on the force in the xy -plane ${}^l\vec{F}_{xy} = [{}^lF_x \quad {}^lF_y]^\top$ by the following minimization problem

$${}^l\vec{F}_{xy,wc} = \arg \min_{{}^l\vec{F}_{xy}} \left\| {}^l\vec{F}_{xy} \right\|_2 \quad \forall \{ {}^lq_x, {}^lq_y \} \subset \mathcal{S}_{\vec{\alpha}} \quad (4.29)$$

$${}^l\vec{w} = [\quad {}^l\vec{F}_{xy}^\top \quad Mg \quad {}^l\vec{T}^\top]^\top$$

$$\| {}^l\vec{i} \|_\infty = i_{max}$$

The minimization searches for the worst-case (minimal) amplitude of the force vector in the xy -plane (using the direct wrench-current decoupling) for which the infinity norm of the current vector equals the maximum current i_{max} (meaning that one or more of the coil currents will clip), while maintaining a constant levitation force in the z -direction ${}^lF_z = Mg$ (where M is the total mass of the translator and g is the gravitational constant). The resulting vector ${}^l\vec{F}_{xy,wc}$ is the worst-case (smallest) acceleration force in the xy -plane at a given position, illustrated by figure 4.9. The worst-case acceleration in the xy -plane ${}^l\vec{q}_{xy}$ can be derived from the worst-case forces by dividing them by the total mass of the translator. The amplitude of the worst-case acceleration and the angle of the vector in the xy -plane with respect to the lx axis are shown for the HPPA topology in figures 4.10 and 4.11, respectively,

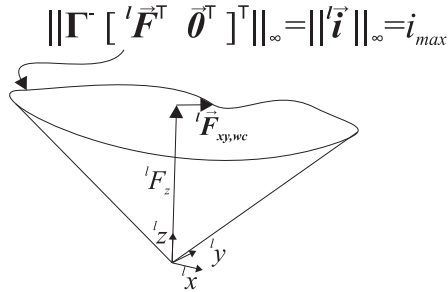


Figure 4.9. Illustration which indicates how the worst-case (smallest) acceleration vector (where one or more of the stator coil currents will clip) can be found at a given position and orientation ${}^l\vec{q}$ when using the direct wrench-current decoupling $\Gamma^{-1} ({}^l\vec{q})$.

using a mass of 8.2 kg and an air-gap (clearance) of 1 mm. Figures 4.12 and 4.13 show the same simulation using the maximum clearance of the HPPA of 2 mm.

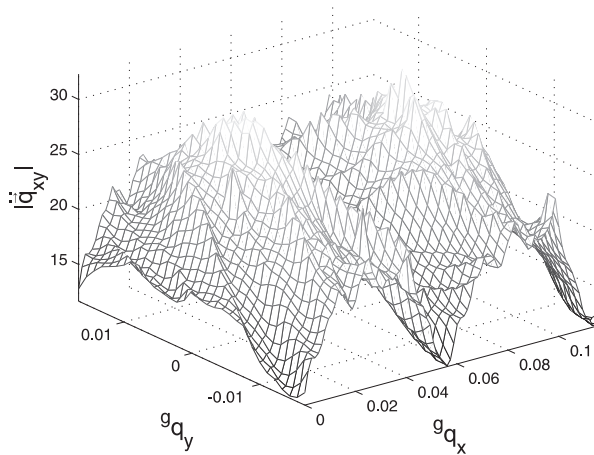


Figure 4.10. Worst-case amplitude of the acceleration vector in the xy -plane $\| {}^l\ddot{\vec{q}}_{xy} \|$ at a clearance of 1 mm.

From these pictures it can be seen that it is possible to obtain an acceleration of at least $12 \frac{m}{s^2}$ in all directions of the xy -plane. When the same minimization problem

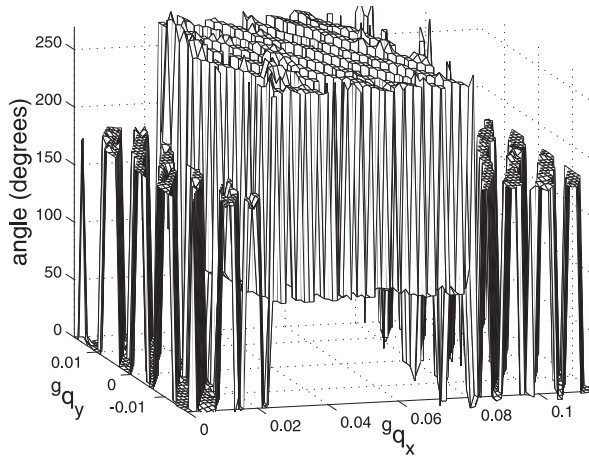


Figure 4.11. Worst-case direction of the acceleration vector in the xy -plane angle $({}^l\ddot{\mathbf{q}}_{xy})$ with respect to the ${}^l x$ -axis at a clearance of 1 mm.

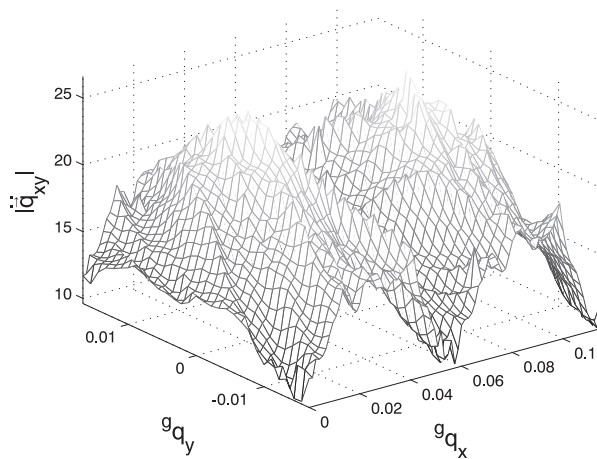


Figure 4.12. Worst-case amplitude of the acceleration vector in the xy -plane $\|{}^l\ddot{\mathbf{q}}_{xy}\|$ at a clearance of 2 mm.

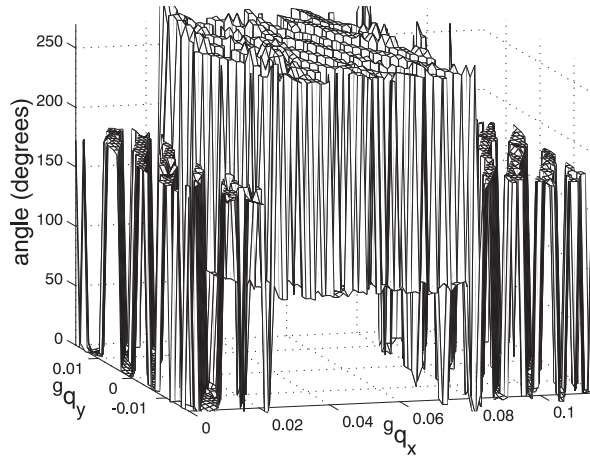


Figure 4.13. Worst-case direction of the acceleration vector in the xy -plane angle $\left({}^l\ddot{\mathbf{q}}_{xy}\right)$ with respect to the lx -axis at a clearance of 2 mm.

is applied to the same settings using a clearance of $q_z = 2$ mm the smallest worst-case acceleration becomes $10 \frac{\text{m}}{\text{s}^2}$ (as can be seen from figure 4.12). The smallest worst-case acceleration and its direction can be explained by looking at the worst-case switching topologies of the HPPA shown in figure 4.14. The darker columns of stator coils shown in figure 4.14 are the only coils which can generate a force in the smallest worst case acceleration direction. Therefore, since the amount of coils which can generate a force in the worst case direction is smallest it is obvious that the current through one of these coils will be the highest.

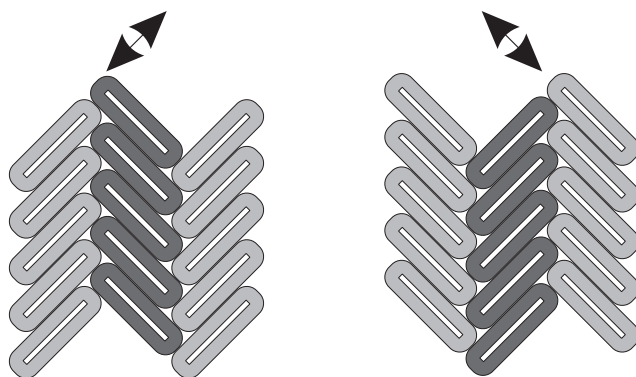


Figure 4.14. *The two active topologies corresponding to the directions of the worst-case acceleration vector in the xy -plane, where only the dark-gray coils can be used for the acceleration in the worst-case direction.*

Chapter 5

Experiments

5.1 Introduction

The theory derived in [17] and the previous chapters of this thesis have been used to create a 6-DOF prototype called the HPPA (Herringbone Pattern Planar Actuator). The experimental setup and some of the experiments which were done using this setup are discussed in this chapter. The experimental setup is discussed in section 5.2. Closed-loop measurements have been performed on the HPPA which are discussed in section 5.4. To explain these measurements, first the control structure is discussed in section 5.3.

5.2 Experimental setup

In this section the experimental setup will be discussed. Section 5.2.1 supplies the details of the HPPA (Herringbone Pattern Planar Actuator) which has been realized. In section 5.2.2 the measurement system is described in detail.

5.2.1 HPPA prototype

A prototype of the herringbone pattern planar actuator (HPPA) which was discussed throughout this thesis has been realized. A more detailed description of the electromechanical analysis and design of the HPPA prototype is given in [17]. Figure 5.1 shows the stator of the realized prototype containing 84 coils. The orthocyclically wound coils have been manufactured by Tecnotion. Each coil is connected to a

single-phase current amplifier which have been supplied by Prodrive (with permission of ASML). Figure 5.2 shows the translator of the HPPA which consists of a stiff aluminum carrier (on the left), which was designed and manufactured by the workshop of the Eindhoven University of Technology, Gemeenschappelijke Technische Dienst (GTD). To the aluminum carrier of the translator 385 magnets have been glued by Vacuumschmelze (shown on the right side of figure 5.2). Table 5.1 shows some of the dimensions and properties of the HPPA, where the coil pitch is defined as the relative displacement of the centers of the stator coils along the gq_x and gq_y direction in the stator plane.

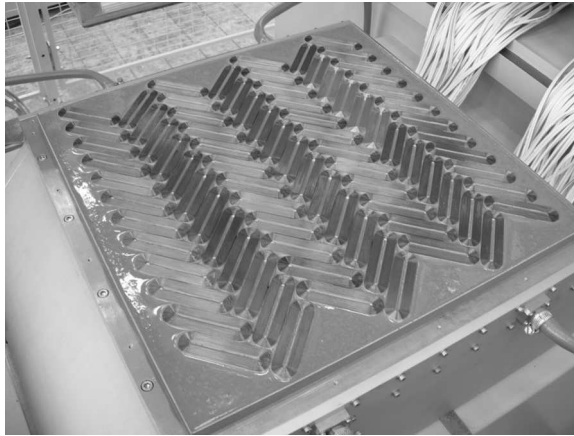


Figure 5.1. Stator of the HPPA with 84 stator coils. The white cables are connected to 84 single-phase currents amplifiers. The hoses are used to cool the stator using water and glycol.

5.2.2 Test bench

The measurements on the HPPA are carried out on a test bench, which is constructed on top of the base frame of an Assembléon H-drive [35, 39] (figures 5.3 and 5.4). A schematic top-view of the H-drive is given in figure 5.4. This gantry consists of three linear motors. Two motors are positioned in parallel (${}^{enc}y_1$ and ${}^{enc}y_2$). Between the translators of these motors a third linear motor is mounted which can move in the ${}^{enc}x$ -direction. By displacing the y_1 - and y_2 -motors with respect to each other, the x -beam can rotate about the z -axis (${}^g\phi_h \pm 5$ mrad). An

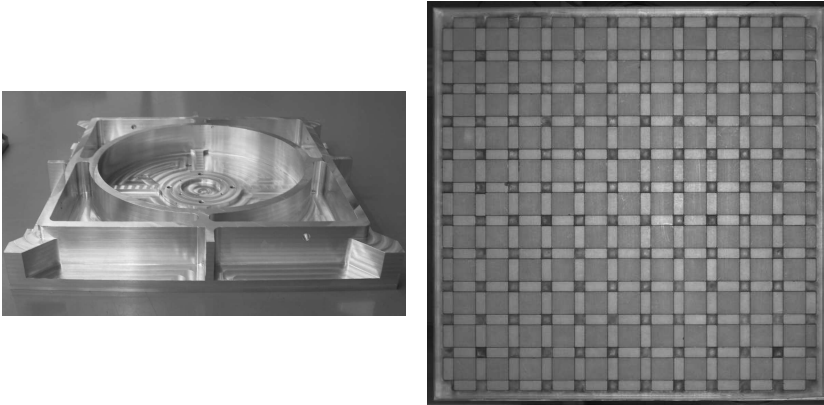


Figure 5.2. *The stiff aluminum carrier to which the magnets are glued to form the translator (on the left). Translator of the HPPA containing 385 magnets arranged in a Halbach pattern (on the right).*

overview of the test-bench is shown in figure 5.3. Figure 5.3 also shows the control hardware. A dSPACE DS1005MP modular DSP system is used with two processor boards. One board is used for IO interfacing and H-drive control, while the other processor board is used for the real-time commutation of the prototype. The IO turned out to be a huge computational load on the DSP because of the 28 RS485 serial interface connections which are providing the 84 amplifier channels of the HPPA stator coils with the current set-points. The sample frequency is set to its maximum possible value of 4kHz (as discussed at the end of section 4.4).

The test bench can operate in two modes.

Force and torque measurement

The translator of the HPPA can be mounted via a 6-DOF load cell (JR3 45E15A4-I63-S 100N10) to the translator of the x -motor of the H-drive. The H-drive can be used to position the translator with the magnet array above the stator coils and the force and torque components can be measured with the load cell. With this configuration, the force and torque acting on the translator of the HPPA itself are measured. However, also disturbances from the H-drive are measured because the bandwidth of the load cell (150 Hz) is much larger than the bandwidth of the controllers of the H-drive (30 Hz). The force and torque are measured statically (stand-still) or

Table 5.1. *Dimensions and properties of the HPPA*

Parameter	Value	Unit
maximum number of active coils (xy)	24 (4x6)	-
total number of coils (xy)	84 (7x12)	-
magnetic poles (xy)	121 (11x11)	-
translator size (xy)	300x300	mm
stroke (xy)	232x233	mm
clearance (z -direction)	1 - 2	mm
max. velocity (xy -plane)	1.0	m/s
worst-case max. acceleration (xy -plane)	10	m/s ²
max. jerk (xy -plane)	1000	m/s ³
pole pitch magnet array, τ	25.0	mm
pole pitch magnet array, τ_n	17.7	mm
coil pitch (gq_x -direction), τ_{cx}	58	mm
coil pitch (gq_y -direction), τ_{cy}	33.3	mm
total mass translator, m	8.2	kg
inertia translator about COG, I_{xy}	0.062	kg m ²
I_z	0.122	kg m ²
mass carrier without magnets, m_c	4.28	kg
permanent-magnet material	VACODYM 655HR	
power amplifiers	PADC3AX52/6	
cooling medium	water/glycol	

quasi-statically at low speed (0.02 m/s). The quasi-statically measured data is filtered off-line with a fourth-order anti-causal low-pass filter with a cut-off frequency of 25 Hz. This filter does not introduce a phase shift in the measurement data. Because of the low measurement speed, the frequency of the measured force and torque signals is low (first harmonic: 0.57 Hz at 0.02 m/s) and, therefore, the higher harmonics of the force and torque are not suppressed by the filter.

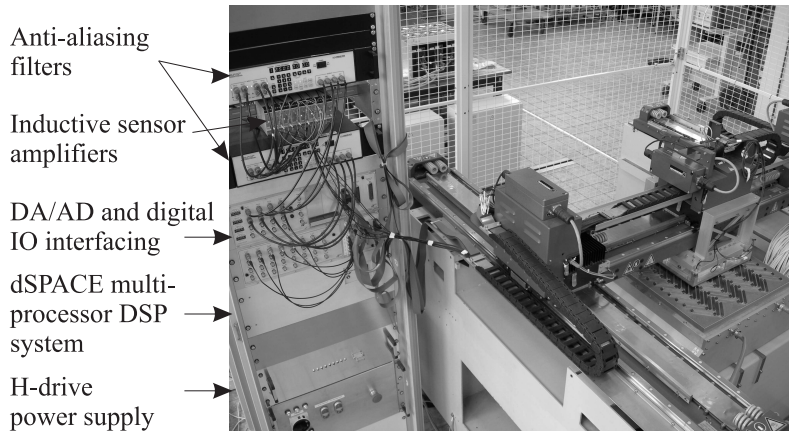


Figure 5.3. Planar actuator test bench.

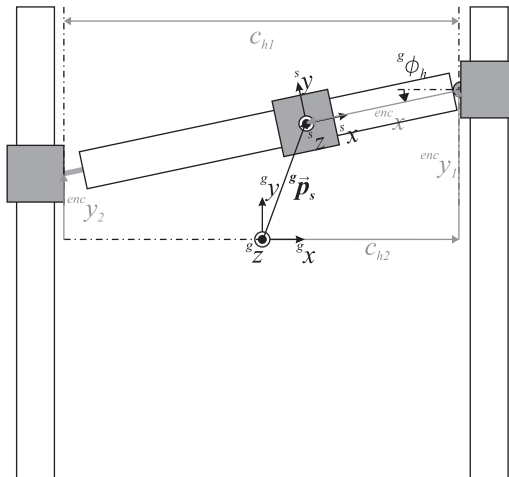


Figure 5.4. H-drive coordinates.

Position measurement with safety bounds

The position on the μm and sub- μm scale can be measured with several techniques, e.g. optical encoders, laser triangulators, laser interferometers, inductive sensors

and capacitive sensors.

These types of sensor differ mainly in accuracy, range and cost. For the measurement system of the HPPA cost was an important issue. Because the H-drive itself is equipped with $1 \mu\text{m}$ resolution optical encoders, it was decided to measure the position of the translator of the HPPA with respect to the H-drive with inductive sensors ($0.16 \mu\text{m}$ rms-resolution) and to use the encoders of the H-drive for the long-stroke position measurement. As the range of the inductive sensors is limited to 2 mm, the H-drive should move simultaneously with the translator of the HPPA.

To reconstruct the position and orientation of the mass-center-point of the translator a measurement frame consisting of eight Lion Inductive ECL100-U8B sensors is attached to the H-drive. Four of them measure the distance between the measurement frame and the translator of the HPPA in the z -direction, two in the x -direction and two in the y -direction. The measurement targets are located at the corners (z -direction) and the centers of the edges of the translator (x - and y -directions). A detail of the measurement frame with the inductive sensors is shown in Figure 5.5. To obtain the desired measurement range, the H-drive and, therefore, the measurement frame, follow the same trajectory in the xy -plane as the translator. Using this strategy it is possible to reconstruct the six degrees-of-freedom by combining the information of the eight inductive sensors with the three optical linear encoders of the H-drive. The non-linear mapping which transforms the eight



Figure 5.5. *Translator and measurement frame.*

inductive sensor outputs $ind\vec{d} = [d_{s1} \ d_{s2} \ d_{s3} \ d_{s4} \ d_{s5} \ d_{s6} \ d_{s7} \ d_{s8}]^T$ m (as shown by the arrows in figure 5.6) and the three linear encoder outputs of the H-drive $enc\vec{q} = [enc_x \ enc_{y_1} \ enc_{y_2}]^T$ (as defined in figure 5.4) to the six degrees-of-freedom of the platform can be obtained in two steps.

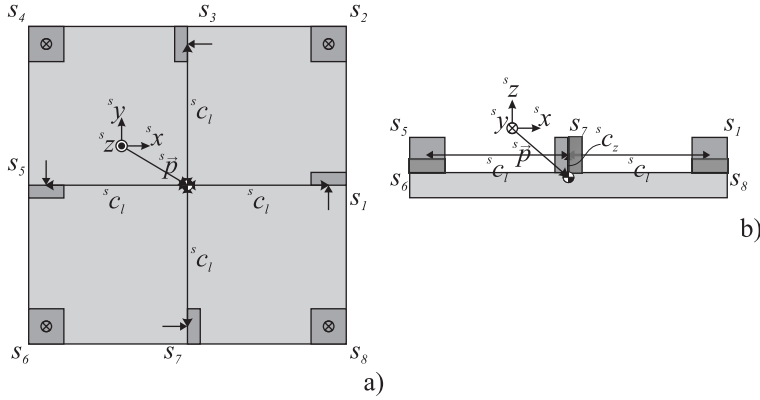


Figure 5.6. Schematic overview of the HPPA translator with respect to the sensors and sensor frame coordinates s a) top-view of the translator. b) side-view of the translator. The actual origin of the sensor frame is closer to the mass-center-point (max. 0.55 mm offset) but it has been increased to show the vectors more clearly.

Firstly, the 6-DOF position ${}^s\vec{p}$ of the translator of the HPPA with respect to the sensor frame is determined

$${}^s\vec{p} \approx {}^s\vec{p}_{offset} + {}^s\mathbf{T}_{ind} \mathit{ind}\vec{d}, \quad (5.1)$$

where (5.1) is an approximation which can be made for small translator angles. The offset vector ${}^s\vec{p}_{offset}$ (as shown in figure 5.6), which describes the small offset of the mass-center-point of the translator with respect to the desired origin of the sensor frame coordinate system (indicated by superscript s), is given by

$${}^s\vec{p}_{offset} = [0 \quad 0 \quad -{}^s c_z]^T, \quad (5.2)$$

and the transformation matrix which reconstructs the position of the HPPA translator in sensor frame coordinates is given by

$${}^s\mathbf{T}_{ind} = \frac{1}{4 {}^s c_l} \begin{bmatrix} 0 & -{}^s c_z & -2 {}^s c_l & {}^s c_z & 0 & {}^s c_z & 2 {}^s c_l & -{}^s c_z \\ 2 {}^s c_l & -{}^s c_z & 0 & -{}^s c_z & -2 {}^s c_l & {}^s c_z & 0 & {}^s c_z \\ 0 & -{}^s c_l & 0 & -{}^s c_l & 0 & -{}^s c_l & 0 & -{}^s c_l \end{bmatrix}, \quad (5.3)$$

where ${}^s c_l$ and ${}^s c_z$ are defined in figure 5.6. The sensors that are opposite to each other in the xy -plane (s_3 and s_7 for the x -direction and s_1 and s_5 for the y -direction) also measure in opposite directions with respect to each other. In this

way the common noise that is picked up by the sensors is removed in the x - and y -directions because the difference of both sensor pairs is used to reconstruct the x - and y -positions (which can also be seen from the signs in the matrix ${}^s\mathbf{T}_{\text{ind}}$ (5.3)). Moreover, this sensor placement allows for the measurement surfaces to be placed in such a way that their mass distribution does not affect the mass-center-point of the translator in the xy -plane (it remains in the center of the translator in the xy -plane). Unfortunately, the same sensor layout cannot be used for the z -direction because this axis can only be measured contactless in one direction using this setup. However, there are four sensors to reconstruct this direction.

The first-order Taylor expansion of the Euler angles of the translator about its working point with respect to the sensor frame is used. This results in the following approximation of the translator angles (where ${}^s\psi$, ${}^s\theta$ and ${}^s\phi$ are the rotations about the ${}^s x$ -, ${}^s y$ - and ${}^s z$ -axis, respectively)

$$\begin{bmatrix} {}^s\psi \\ {}^s\theta \\ {}^s\phi \end{bmatrix} \approx \frac{1}{4 {}^s c_l} \begin{bmatrix} 0 & -1 & 0 & -1 & 0 & 1 & 0 & 1 \\ 0 & 1 & 0 & -1 & 0 & -1 & 0 & 1 \\ 1 & 0 & 1 & 0 & 1 & 0 & 1 & 0 \end{bmatrix} \text{ind} \vec{d}. \quad (5.4)$$

The maximum angles of the translator about the x - and y -axes are small due to the limited levitation height and the maximum angle about the z -axis is also kept small because of the limited sensor range and because the analytical model which is used in the decoupling algorithm does not hold for large rotations about this axis. Moreover, they are kept even smaller (maximum of 6 mrad) because of safety issues (see the end of this section). Therefore, using a first-order Taylor approximation does not result in large errors (maximum position errors in the micrometer range when using the maximum admissible angles).

However, when calculating the second transformation which transforms the sensor frame coordinates to the global coordinates using the three linear encoders of the H-drive, the transformation is not linearized with respect to the H-drive angle because the rotation about the z -axis of the H-drive (${}^g\phi_h$ as defined in figure 5.4) would result in unacceptable position errors in the xy -plane when using a first-order Taylor expansion due to the large distance between the point of rotation of the H-drive and the center of mass of the translator of the HPPA (a distance in the order of 0.5 m in the working point of the HPPA). Therefore, the transformation of the position of the translator with respect to the sensor frame (in sensor frame coordinates s) to the position with respect to the global coordinate system (in global coordinates g) is given by

$${}^g\vec{p} = {}^g\vec{p}_s ({}^{enc}\vec{q}) + {}^g\mathbf{R}_s ({}^{enc}\vec{q}) {}^s\vec{p}, \quad (5.5)$$

where the rotation matrix is given by

$${}^s\mathbf{R}_s = \begin{bmatrix} \cos({}^g\phi_h) & -\sin({}^g\phi_h) & 0 \\ \sin({}^g\phi_h) & \cos({}^g\phi_h) & 0 \\ 0 & 0 & 1 \end{bmatrix}, \quad (5.6)$$

and the measurement frame position in global coordinates is given by

$${}^g\vec{p}_s ({}^{enc}\vec{q}) = \begin{bmatrix} c_{h2} - {}^{enc}x \cos({}^g\phi_h) \\ {}^{enc}y_1 - {}^{enc}x \sin({}^g\phi_h) \\ c_{h3} \end{bmatrix}, \quad (5.7)$$

where ${}^{enc}x$ and ${}^{enc}y_1$ (which are elements of the vector ${}^{enc}\vec{q}$) are defined in figure 5.4. The sine and cosine of ${}^g\phi_h$ can be reconstructed (for $-\frac{\pi}{2} < {}^g\phi_h < \frac{\pi}{2}$) by

$$\begin{aligned} \cos({}^g\phi_h) &= \frac{1}{\sqrt{1 + \left(\frac{{}^{enc}y_1 - {}^{enc}y_2}{c_{h1}}\right)^2}}, \\ \sin({}^g\phi_h) &= \frac{{}^{enc}y_1 - {}^{enc}y_2}{c_{h1} \sqrt{1 + \left(\frac{{}^{enc}y_1 - {}^{enc}y_2}{c_{h1}}\right)^2}}, \end{aligned} \quad (5.8)$$

which results in an exact solution of the translator position in global coordinates when all angle components are zero and an approximation for small angles which can be calculated using the eleven sensors. The angle components of the translator with respect to the global coordinates can be reconstructed as follows

$$\begin{bmatrix} {}^g\psi \\ {}^g\theta \\ {}^g\phi \end{bmatrix} = \begin{bmatrix} s_\psi \\ s_\theta \\ s_\phi + {}^g\phi_h \end{bmatrix}. \quad (5.9)$$

Because of the position measurement system, the H-drive is always moving together with the translator of the planar actuator. To prevent damage caused by contact between the stator and the translator of the HPPA due to, for example, unstable controllers or power failure, the stroke of the translator of the HPPA with respect to the measurement frame is limited by four pins (diameter 4.9 mm) which are captured by over-sized holes (diameter 6 mm) in the translator of the HPPA. Two of these pins are indicated in Figure 5.5. The disadvantage of these pins is that the rotation angles of the translator of the HPPA are limited to 6 mrad and the relative translation (between the translator and the measurement frame) is limited to 1.1 mm. Once the HPPA is in control, there is no contact between its translator and the measurement frame.

Additionally, the maximum reference force and torque components of the HPPA are limited to prevent further damage to the system (max. force gF_x , gF_y and gF_z of 100N and max. torque gT_x and gT_y of 8Nm and gT_z of 10Nm).

5.3 Control structure

After linearization and decoupling of the system the HPPA needs to be stabilized. Because the system has been decoupled six SISO controllers have been used. Essentially the decoupled mechanical system can be described as if each degree of freedom (here indicated by q) consists of a double integrator

$$\frac{q}{\ddot{q}_{des}} = \frac{1}{s^2}. \quad (5.10)$$

The structure of these six SISO controllers can, therefore, be the same for each degree of freedom.

After applying the decoupling algorithm the system is theoretically meta-stable. This indicates that infinitely small model perturbations caused by erroneous decoupling can cause instability of at least one of the degrees of freedom and oscillations in the other degrees of freedom. A small signal approximation of the system and the decoupling (for one DOF) by linearization about a fixed position and orientation can be used to illustrate this as shown in figure 5.7. In the figure the (for simplicity one DOF) non-linear mapping $\Gamma_{1\text{dof}}(q)$ of the HPPA model is split into a current gain vector \mathbf{K}_i and a position gain \mathbf{K}_p . The inverse mapping $\Gamma_{1\text{dof}}^{-1}(q)$ can be rewritten as a function of an inverse mapping of the current gain vector \mathbf{K}_i^{-1} and the position gain \mathbf{K}_p . The figure shows the resulting simplified system when an error is made in the position gain (indicated by \mathbf{K}_p^*) resulting in either an unstable or an oscillating system depending on the sign of the difference of $\mathbf{K}_p - \mathbf{K}_p^*$. The errors in the \mathbf{K}_i^{-1} term similarly result in an unstable or oscillating system with additive disturbance terms. Fortunately, errors in the decoupling will not result in additional zeros which would complicate the stabilization of the plant or, in the case of right-half plane zeros, limit the obtainable bandwidth. The errors in the decoupling can, therefore, be modeled as small perturbations of the poles over the real or imaginary axis (symmetric w.r.t. the origin) and gains.

There are three different discrete modes which have been implemented to control the HPPA:

- start-up/lift-off mode
- operational/tracking mode
- shut-down/landing mode

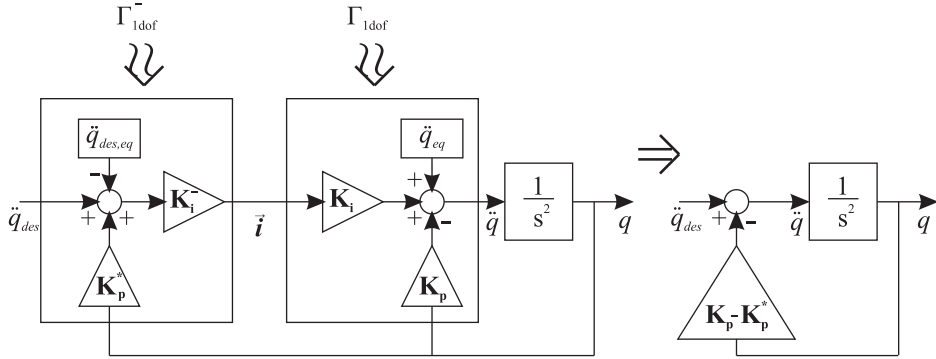


Figure 5.7. Linearized HPPA model with decoupling (simplified to one degree of freedom).

Each mode has its own set of SISO controllers which need to be switched. Moreover, each mode transition needs to be bumpless.

Start-up / lift-off mode

The first mode takes place when the HPPA is switched on. At start-up the translator of the HPPA is touching the safety pins of the measurement frame (as explained at the end of section 5.2). Therefore, the start-up controllers do not contain an integrator which could cause damage to the stator coils when the lift-off reference trajectory is slightly outside the admissible set of possible coordinates (which would cause wind-up because the integrative action would increase the coil currents). The six SISO start-up controllers consist of a lead-lag filter to create phase-lead for stability and a roll-off low-pass filter to create a strictly-proper controller

$$\frac{\ddot{q}_{fb}}{q} = C_{pd}(s) = g_{bw} \frac{(s + z_{ll})}{(s + p_{ll})} \frac{1}{(s + p_{lpf})}, \quad (5.11)$$

where g_{bw} is the gain, z_{ll} and p_{ll} are the zero and pole of the lead-lag filter, respectively, and p_{lpf} is the pole of the low-pass filter. Given a certain desired bandwidth c_{bw} rad (defined as the frequency of the 0dB point of the amplitude of the open-loop

transfer function) the control parameters can be derived as follows

$$\begin{aligned}
 g_{bw} &= c_{z,ll} \sqrt{\frac{1+c_{p,ll}^2}{1+c_{z,ll}^2}} c_{bw} \sqrt{1+c_{p,lpf}^2} c_{bw}^2, \\
 z_{ll} &= \frac{c_{bw}}{c_{z,ll}}, \\
 p_{ll} &= c_{bw} c_{p,ll}, \\
 p_{lpf} &= c_{bw} c_{p,lpf},
 \end{aligned} \tag{5.12}$$

where the new parameters are normalized with respect to the desired bandwidth. Assuming an ideal plant (double integrator), the resulting system can now be loop shaped using $c_{z,ll}$, $c_{p,ll}$ and $c_{p,lpf}$ and scaled to the desired bandwidth using c_{bw} . Where $c_{z,ll}$ and $c_{p,ll}$ can be used to create phase-lead at the desired bandwidth by influencing the zero and pole location of the lead-lag filter, respectively, scaled with the desired bandwidth, to create robust stability. Furthermore, $c_{p,lpf}$ influences the pole location of the low-pass filter, scaled with the desired frequency, to create a strictly-proper controller (with $c_{p,lpf} > c_{p,ll}$ so the phase-lead is not influenced too much by the low-pass filter). Moreover, acceleration feed-forward is used to improve the tracking error resulting in

$$\ddot{q}_{des} = \ddot{q}_{ref} + \ddot{q}_{fb}. \tag{5.13}$$

The start-up controller of the HPPA setup using the following parameters $c_{z,ll}=5$, $c_{p,ll}=4$, $c_{p,lpf}=4$ and $c_{bw}=60$ rad/s results in the root locus and Bode plot of the open-loop system shown in figures 5.8 and 5.9, respectively.

Operational / tracking mode

After lift-off, the system checks if the position and orientation error of the platform stays within specified bounds with respect to its desired operating point (absolute value of each position error < 1 mm and of each rotation < 2 mrad) in 6 DOF for 1 second. When this is the case the system switches to the tracking mode which has its own set of six SISO tracking controllers which have the same parameters and structure as the start-up controllers with an added gain $g_{bw,i}$ and accompanying pole zero pair p_i and z_i

$$C_{pid}(s) = g_{bw,i} \frac{s + z_i}{s + p_i} C_{pd}(s), \tag{5.14}$$

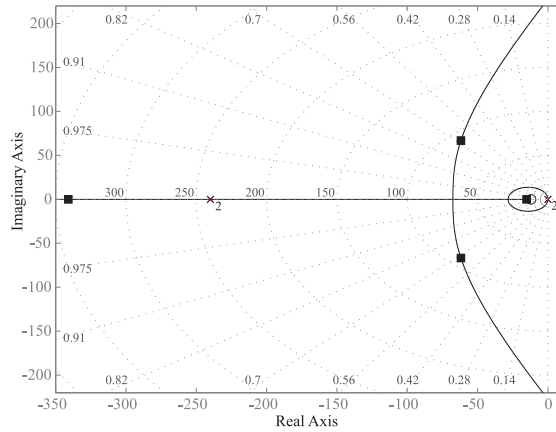


Figure 5.8. Root locus using the strictly-proper pd controller with $c_{z,tl}=5$, $c_{p,tl}=4$, $c_{p,lpf}=4$ and $c_{bw}=60$ rad/s. (the closed-loop poles are indicated by squares and the open-loop poles and zeros are indicated by circles and crosses, respectively)

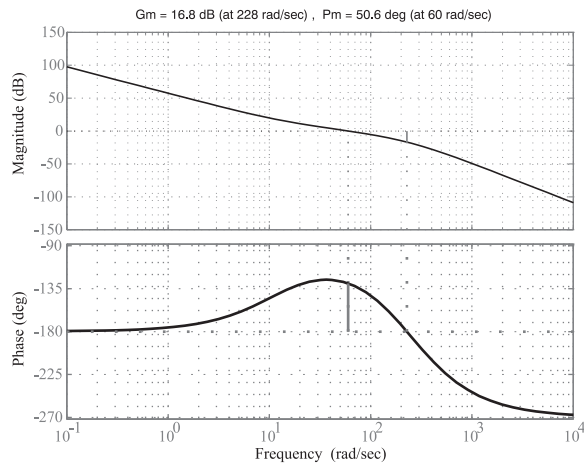


Figure 5.9. Bode plot of the open-loop system using the strictly-proper pd controller with $c_{z,tl}=5$, $c_{p,tl}=4$, $c_{p,lpf}=4$ and $c_{bw}=60$ rad/s.

where the additional gain, pole and zero are defined as

$$\begin{aligned} g_{bw,i} &= c_{z,i} \sqrt{\frac{1+c_{p,i}^2}{1+c_{z,i}^2}}, \\ z_i &= c_{bw}/c_{z,i}, \\ p_i &= c_{bw}c_{p,i}, \end{aligned} \quad (5.15)$$

where z_i and p_i are again normalized with respect to c_{bw} , resulting in $c_{z,i}$ and $c_{p,i}$, respectively, which can be used to create integrative action in the controller. The additional gain $g_{bw,i}$ is introduced to keep the 0dB point of the open-loop system at the desired frequency of c_{bw} . Moreover, the initial states of the tracking controller are identical to the states of the start-up controller during switching and the initial state of the added pole zero pair is set to zero and the normalized pole and zero parameters are set to $c_{p,i} = \frac{1}{c_{z,i}}$. This effectively results in the same control structure during switching (because the pole and zero of the controller cancel each other) which, therefore, guarantees smooth bumpless switching between the controllers. After switching, the added pole p_i is slowly (quasi-statically) moved towards zero by smoothly decreasing $c_{p,i}$ to zero, creating an integrative action in the tracking controller, in order to remove steady-state tracking errors. Moreover, after creating the integrative action, the parameter defining the bandwidth c_{bw} is slowly (quasi-statically) increased over a time-span of one second to 330 rad/s. When assuming an ideal plant ($\frac{1}{s^2}$), increasing the bandwidth c_{bw} only results in scaling of the root-locus plots and the closed-loop poles without changing their relative positions, due to the normalized gain, pole and zero locations of the controller. The root-locus and Bode plot of the open-loop system are shown in figures 5.10 and 5.11, respectively, for a bandwidth of 60 rad/s (before increasing the bandwidth to 330 rad/s).

Shut-down / landing mode

The third mode is the landing mode which has the same set of SISO controllers as the tracking mode. This mode assures smooth landing of the translator before it is switched off. The landing phase smoothly removes the integrative action by increasing $c_{p,i}$ back to $\frac{1}{c_{z,i}}$ after which it smoothly decreases the bandwidth c_{bw} to 30 rad/s. After this step, the levitation height reference trajectory ${}^g q_{z,ref}$ is smoothly decreased to zero (which is below the allowed position in the z-direction) and, simultaneously, the gravity force feed-forward signal (of 80.7N in the ${}^g F_z$ direction) is smoothly decreased by 5 N. Consequently, the translator of the HPPA will start to land. After touching the safety pins the desired force in the ${}^g q_z$ direction ${}^g F_{z,des}$ will decrease due to the reference trajectory in the z-direction ${}^g z_{ref}$ which

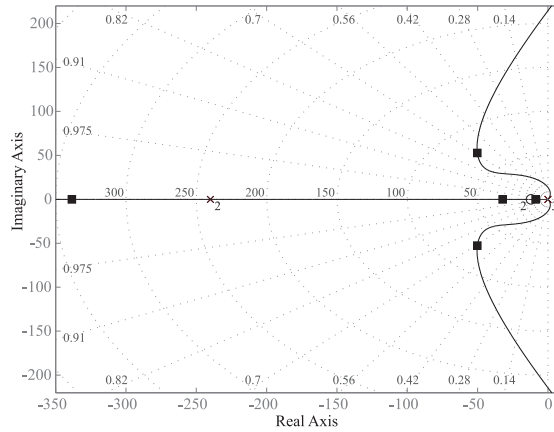


Figure 5.10. Root locus using the strictly-proper pid controller with $c_{z,1l}=5$, $c_{p,1l}=4$, $c_{p,1pf}=4$, $c_{z,i}=5$, $c_{p,i}=0$ and $c_{bw}=60$ rad/s. (the closed-loop poles are indicated by squares and the open-loop poles and zeros are indicated by circles and crosses, respectively)

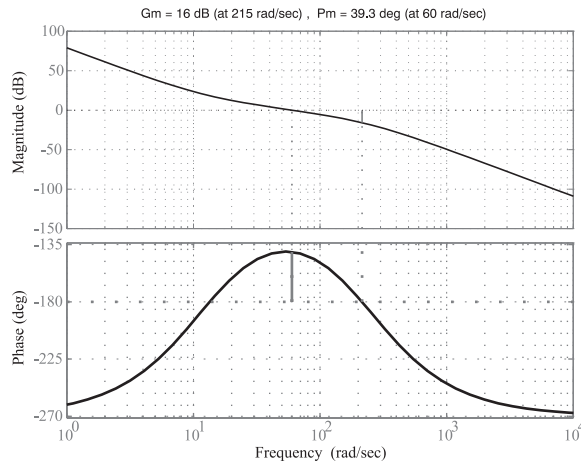


Figure 5.11. Bode plot of the open-loop system using the strictly-proper pid controller with $c_{z,1l}=5$, $c_{p,1l}=4$, $c_{p,1pf}=4$, $c_{z,i}=5$, $c_{p,i}=0$ and $c_{bw}=60$ rad/s.

continues to decrease. When the force output value of the controller in the z-direction ${}^gF_{z,des}$ is below a threshold value of 75 N the currents are set to zero and the system is switched off. The switch in the current set-points before switching off is dealt with by the amplifiers.

5.4 Measurement results

This section discusses the dynamic measurements which were performed on the system. Two different experiments are discussed in this section. The first experiment focusses on closed-loop dynamical identification of the linearized and decoupled system using noise identification. The second experiment focusses on the tracking errors of three specially selected trajectories.

5.4.1 Closed-loop identification

To carry out the dynamical identification of the decoupled system the system needs to be controlled first. The identification controller which was used to carry out these experiments has the following controller parameters (which were defined in section 5.3): $c_{z,ll}=3$, $c_{p,ll}=3$, $c_{p,lpf}=50$, $c_{z,i}=5$, $c_{p,i}=0$ and $c_{bw}=60$ rad/s. The resulting SISO controllers (during the tracking mode) then become

$$C_{pid}(s) = 3.18 \cdot 10^7 \frac{(s + 12)(s + 20)}{s(s + 180)(s + 3000)}. \quad (5.16)$$

Using these controllers Gaussian white noise can be inserted in the loop to identify the system using a Siglab identification device. The maximum identification stroke of the translator is limited by the safety pins because the H-drive is not excited, to prevent unwanted crosstalk of the dynamical systems. This limits the rms value of the noise that can be used in order to get a valid identification. The resolution of the measurement system is also limited because the optical linear encoders have a resolution of $1\mu\text{m}$. This limits the maximum frequency which can be properly identified. The maximum frequency is limited by the expected double integrator of the plant because the behavior of the plant at higher frequencies needs an increasing amount of input power to be visible at the sensor outputs. The input power is limited because of the thermal limits of the active stator coils (the system is already dissipating because of the magnetic bearing in addition to the dissipation needed to perform the identification). When using the controller given by (5.16) in combination with a maximum rms (gaussian) position noise of 0.2mm the maximum frequency which can be properly identified (here defined as the frequency

for which the predicted closed-loop frequency response multiplied by the rms value of the maximum noise reaches the quantization levels of the position encoders) is predicted at approximately 0.2kHz. The same controller is used to identify the rotation where the maximum rms orientation noise is limited to 0.7mrad (which is again limited due to the safety pins). The position noise is shaped by the control sensitivity which results in an integrative action for very low frequencies which removes DC errors. Moreover, it reduces the amplitudes for the low frequencies which are of less interest (and which would cause the translator to hit its safety margins) and it boosts the higher frequencies which are of interest (the desired cross-over frequencies). The frequency response of the sensitivity

$$\mathbf{S}(j\omega) = (\mathbf{I} + \mathbf{P}(j\omega) \mathbf{C}(j\omega))^{-1}, \quad (5.17)$$

of the total system with controller is identified by correlating the inserted position noise which is inserted in the loop with the measured position and orientation errors. The frequency response of the plant can now be reconstructed as follows

$$\mathbf{P}(j\omega) = (\mathbf{S}^{-1}(j\omega) - \mathbf{I}) \mathbf{C}^{-1}(j\omega), \quad (5.18)$$

where $\mathbf{S}(j\omega)$ is a matrix constructed out of all thirty six frequency responses of the system and where $\mathbf{C}(j\omega)$ is a diagonal matrix containing the six SISO tracking controllers for each degree of freedom. Furthermore, the plant $\mathbf{P}(j\omega)$ can be scaled using the normalization matrix \mathbf{N} which is defined in section 4.3 resulting in

$$\mathbf{P}^*(j\omega) = \mathbf{N} \mathbf{P}(j\omega) \mathbf{N}^{-1}, \quad (5.19)$$

which now has the same units for each degree-of-freedom allowing for comparison of the cross-terms of $\mathbf{P}^*(j\omega)$ with the diagonal terms.

Point *d* shown in figure 5.12 shows the point in the *xy*-plane where the identification is performed. The levitation setpoint during identification has been set to 1.2mm and the rotation setpoints (with respect to the general coordinate system *g*) have been set to zero. Figures 5.13-5.18 show the Bode plots of the diagonal terms of the transfer functions of the normalized plant and the approximate amplitudes of the cross-terms of the same input to the other outputs. The problem with identifying the cross-terms is that for higher frequencies it is not possible to insert enough noise power to identify them properly (below position sensor resolution). The coherence of the cross-terms of the identified sensitivity (where averaging of four independent noise measurements is used) for the frequency components which can be excited is very low (below 0.5). Only in the frequency band between approximately 10Hz and 20Hz the coherence is above 0.7 for the cross-terms which are above the noise

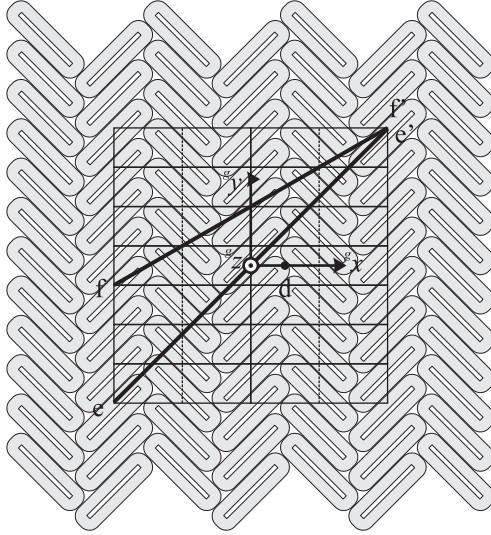


Figure 5.12. Trajectories d , $e - e'$ and $f - f'$ on which the position and angle errors of the controlled HPPA have been measured. d also indicates the position at which the dynamics of the HPPA have been identified.

limit. This indicates that the cross-coupling could be non-linear or that the signal to noise ratio could be too low. The reconstructed cross-terms, therefore, are not reliable. The additional phase shift is caused by the anti-aliasing filters, and the communication delay to the amplifiers. The additional phase shift limits the closed-loop bandwidth which can be obtained by the system. The gain and phase margins of the real system using the tracking controller with a bandwidth of 330 rad/s as described in section 5.3 are reduced to as low as 15 and 3 dB, respectively. Even with these low margins the system remains working properly. Although in previous chapters the decoupling algorithm has been defined in its most general form as

$${}^l\vec{i}_{\vec{\alpha}} = \Gamma^{-} ({}^l\vec{q}) {}^l\vec{w}_{des}, \quad (5.20)$$

where the 6-DOF decoupling matrix $\Gamma^{-} ({}^l\vec{q})$ depends on the 6-DOF position and orientation vector ${}^l\vec{q}$, at first the 6-DOF decoupling matrix was implemented depending only on the 3-DOF position. At normal operation, when the angles can be assumed to be zero, the resulting decoupling will be equivalent. When stiff magnetic bearing controllers are used, this results in a good decoupling of the system

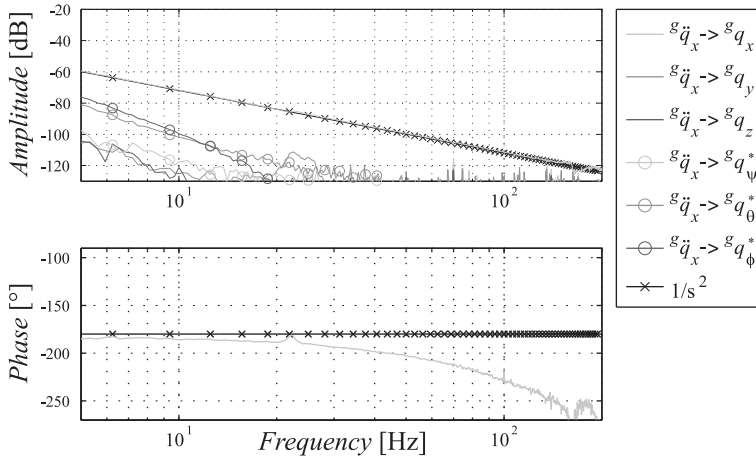


Figure 5.13. Normalized Bode plot of ${}^g\ddot{q}_x \rightarrow {}^gq_x$ including the amplitudes of the cross-terms.

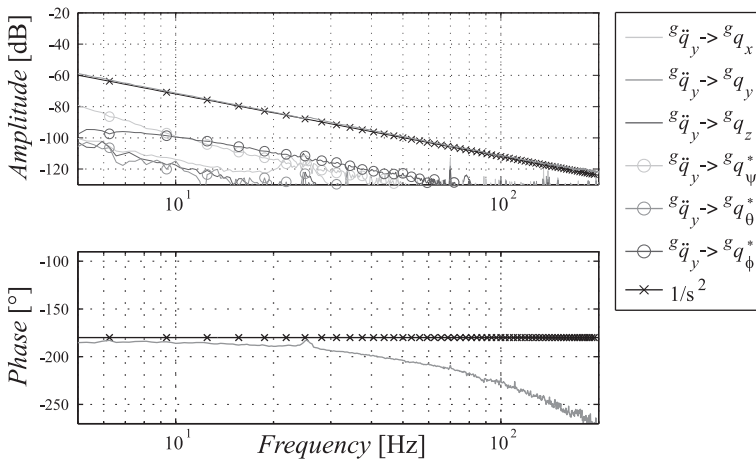


Figure 5.14. Normalized Bode plot of ${}^g\ddot{q}_y \rightarrow {}^gq_y$ including the amplitudes of the cross-terms.

because the angle errors are small. However, during identification of the system the angles are excited over a larger range. Therefore, an approximation for small

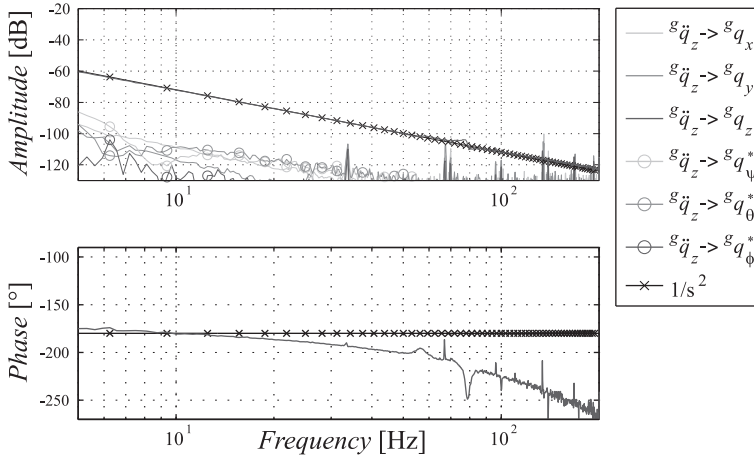


Figure 5.15. Normalized Bode plot of $g_{\ddot{q}_z} \rightarrow g_{q_z}$ including the amplitudes of the cross-terms.

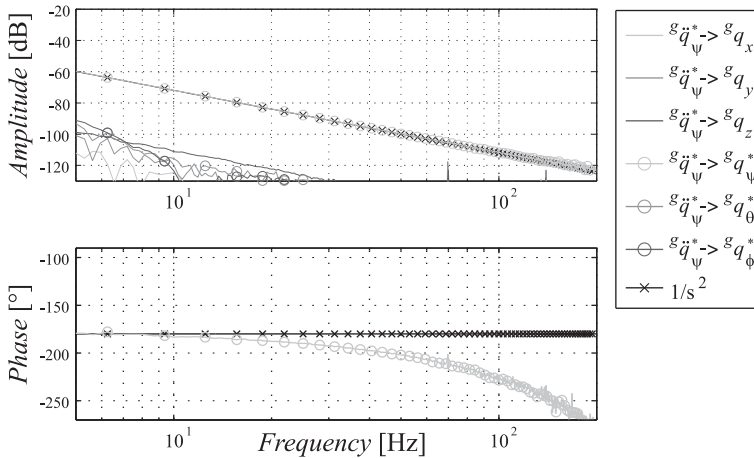


Figure 5.16. Normalized Bode plot of $g_{\ddot{q}_\psi}^* \rightarrow g_{q_\psi}^*$ including the amplitudes of the cross-terms.

angles about the x - and y -axis has been included in the decoupling using an effective local distance in the z -direction between the translator and each individual coil

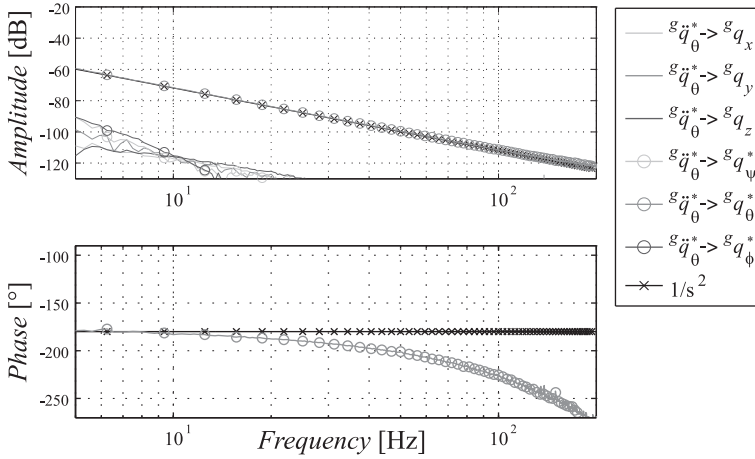


Figure 5.17. Normalized Bode plot of ${}^g\ddot{q}_\theta^* \rightarrow {}^gq_\theta^*$ including the amplitudes of the cross-terms.

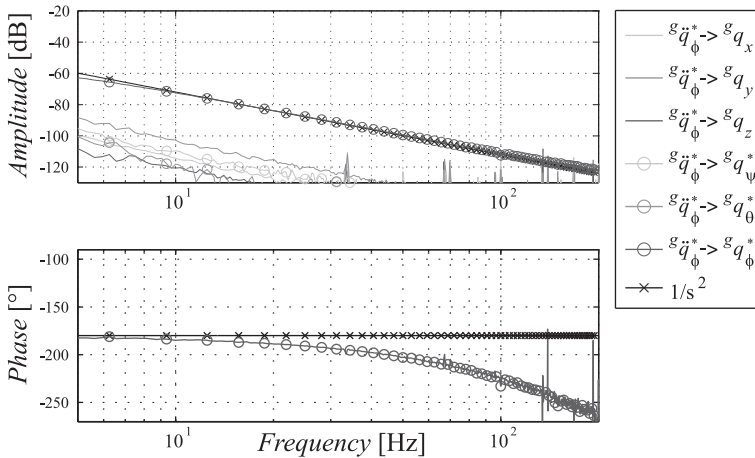


Figure 5.18. Normalized Bode plot of ${}^g\ddot{q}_\phi^* \rightarrow {}^gq_\phi^*$ including the amplitudes of the cross-terms.

(ignoring the higher-order effects of the rotation of the local magnetic field). This results in a more accurate decoupling for a larger range of x - and y -angles. Fig-

Figure 5.19 shows the difference in identification results when using a 3-DOF position dependent decoupling and when using a 5-DOF dependent decoupling (including the rotations about the x - and y -axis). The Bode plot clearly shows a badly damped resonance. This is caused by the error in the decoupling which at this identification position results in a complex pole pair in the left-half plane. The expected results would have been an undamped resonance when assuming the perfectly decoupled HPPA dynamics to be a double integrator. However, there is a small damping term present in the HPPA due to eddy current damping in the aluminum back-plate to which the stator coils are attached causing the complex pole pair to shift slightly to the left-half plane. Using the 5-DOF dependent decoupling, the resonance in the identified system is gone as can be seen from Figure 5.19.

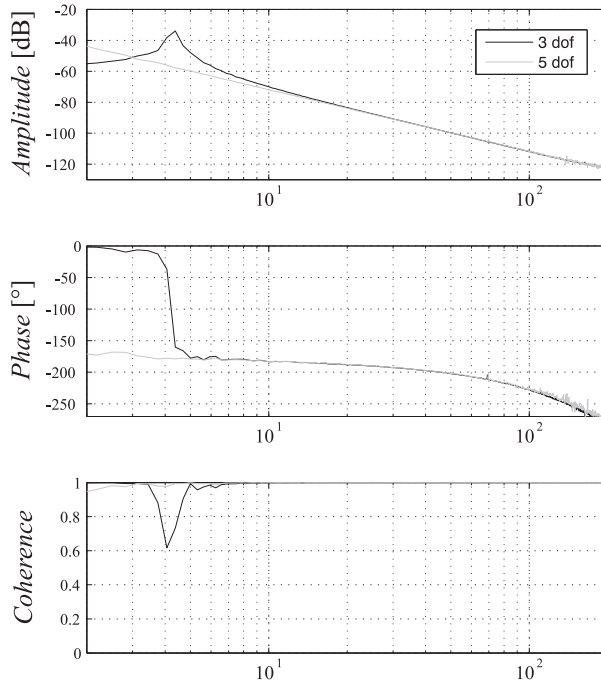


Figure 5.19. Normalized Bode plots of ${}^g\ddot{q}_\psi^* \rightarrow {}^gq_\psi^*$ using a 3-DOF (without the angles) and a 5-DOF (including the ${}^gq_\psi$ and ${}^gq_\theta$ angles) dependent commutation algorithm.

5.4.2 Tracking performance

The second experiment involves measuring the tracking errors for two demanding trajectories in the xy -plane and a movement in the z -direction. The trajectories are shown in figure 5.12 where the clearance in the z -direction was set to 1mm for the xy -trajectories. Further information about the motion profile is given in table 5.2. The position and angle tracking errors for trajectory e-e' are shown in figure 5.20 together with the acceleration profile and the estimated power dissipation. The power dissipation has become position dependent due to the non-linear decoupling strategy. At first instance the worst-case maximum acceleration at a clearance of 1mm which is derived in section 4.5 seems to be violated by this trajectory. Nevertheless, the trajectory avoids the worst-case points during acceleration (the maximum worst-case acceleration in the xy -plane as a function of position is given by figure 4.10). The motion profile is not visible anymore in the tracking errors, which are less than $30 \mu\text{m}$ and 0.1 mrad . The oscillation which is mainly present in the gq_x and gq_y position errors is probably caused by vibrations of the H-drive and the measurement frame which moves simultaneously with the translator of the HPPA in the xy -plane. Further optimization of the controllers is, therefore, only useful when the measurement system is improved. The acceleration profile, the power dissipation and the position and angle tracking errors of trajectory f-f' are shown in figure 5.21. This trajectory moves exactly through the worst-case switching points at which only fifteen coils are active, although the acceleration vector is not along the worst-case acceleration direction in the xy -plane (as explained in section 4.5). The five points of the trajectory at which only fifteen coils are active are visible in the power dissipation plot as the point where there is a slightly increased dissipation. However, the switching points are not visible in the tracking errors. The acceleration profile, the power dissipation and the position and angle tracking errors of trajectory d are shown in figure 5.22. The H-drive is switched off during the measurement of this trajectory in order to reduce the disturbances of the measurement setup. It can be seen from figure 5.22 that the acceleration profile and the increasing levitation force are visible in the tracking error of the gq_z -position. This is an indication that either the feed-forward or the effective gain at this position in the decoupling still has some error over the full range in the z -direction. Nevertheless, the error is much smaller than the mechanical tolerances of the H-drive in the z -direction over the measurement range in the xy -plane (which is estimated to be $< 5 \cdot 10^{-5} \text{ m}$).

Figure 5.23 shows the 6-DOF steady-state error of the system (when the H-drive is switched off) at static levitation (in point d indicated in figure 5.12 with a clearance of 1.5 mm). The rms-errors are $0.1 \mu\text{m}$ and $1 \mu\text{rad}$, respectively, which is corresponding to the rms-resolutions of the inductive sensors after calibration

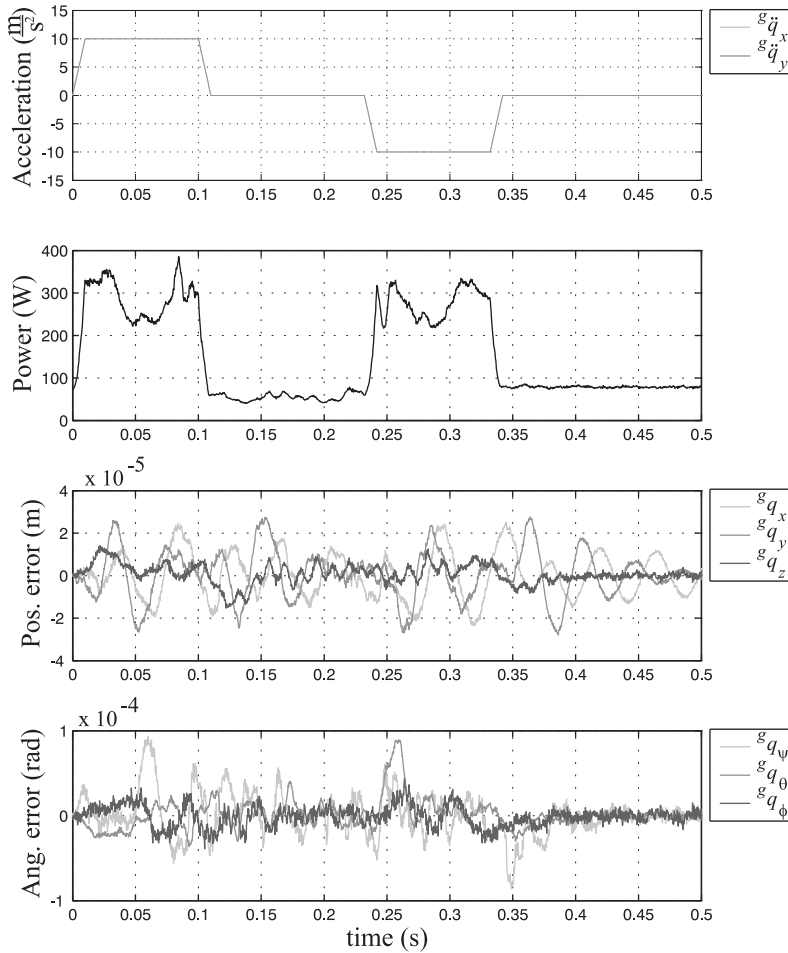


Figure 5.20. Acceleration profile, estimated power dissipation and the position and angle errors of the translator of the HPPA during movement on trajectory *e-e'* defined in figure 5.12 and table 5.2.

($0.09\text{-}0.13 \mu\text{m}$). Moreover, it can be seen that the error of the position in the *z*-direction and the rotation about the *z*-axis clearly contains a 100Hz component which is not present in the other degrees-of-freedom. This is caused by the com-

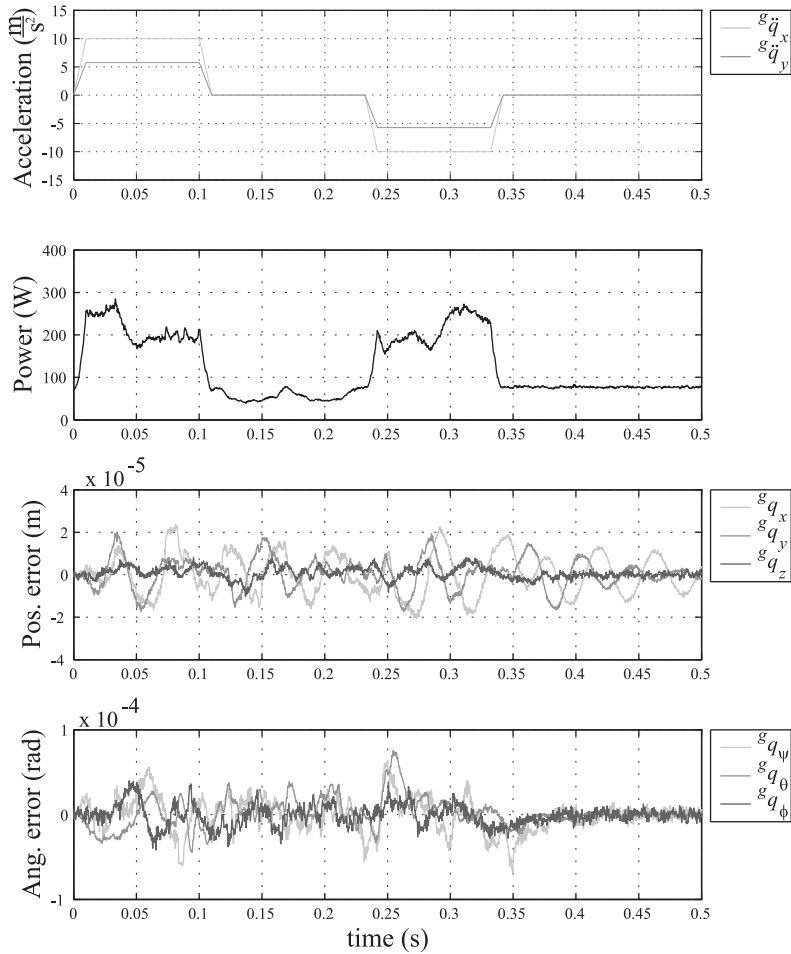


Figure 5.21. Acceleration profile, estimated power dissipation and the position and angle errors of the translator of the HPPA during movement on trajectory f - f' defined in figure 5.12 and table 5.2.

mon noise of the inductive sensors, which is not canceled for these two degrees-of-freedom (which is explained in section 5.2.2).

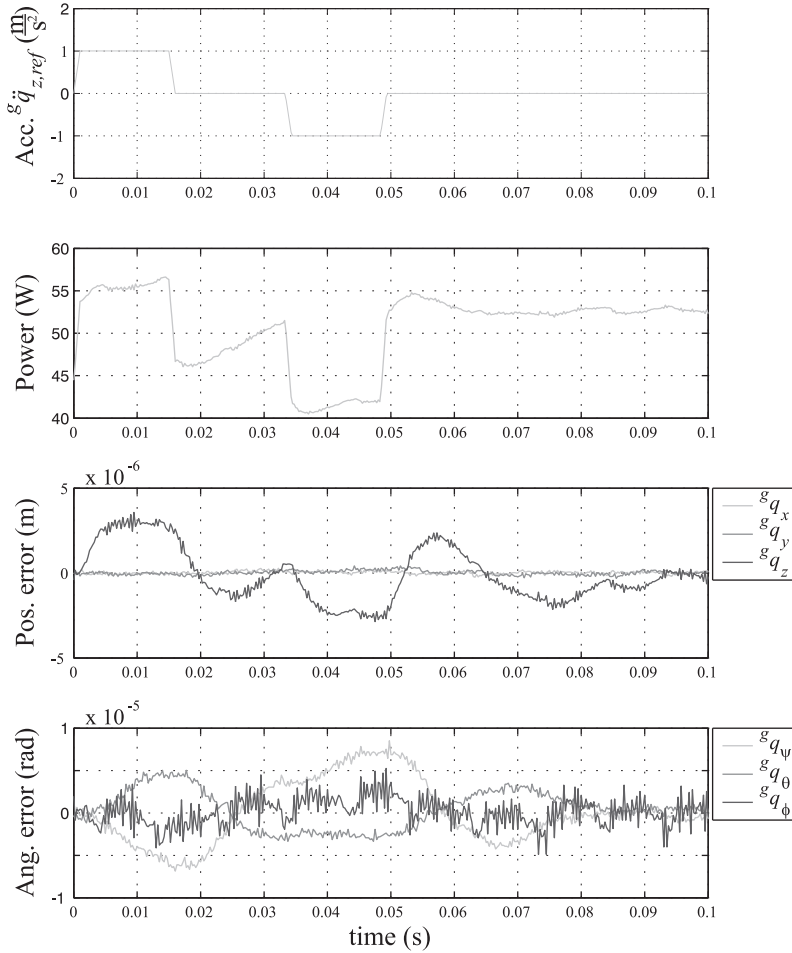


Figure 5.22. Acceleration profile, estimated power dissipation and the position and angle errors of the translator of the HPPA during movement on trajectory d defined in figure 5.12 and table 5.2.

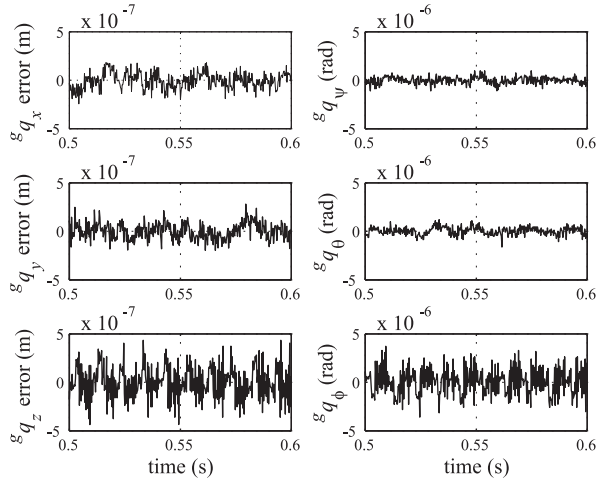


Figure 5.23. Static levitation position and angle errors of the translator of the HPPA in point d defined in figure 5.12 with a clearance of 1.5mm.

Table 5.2. Information of the motion profiles at different trajectories

	d	e-e'	f-f'	
clearance	1.0-1.5	1.0	1.0	mm
${}^g \dot{q}_{x,ref}$	0	1.0	1.0	m/s
${}^g \dot{q}_{y,ref}$	0	1.0	0.575	m/s
${}^g \dot{q}_{z,ref}$	0.015	0	0	m/s
${}^g \ddot{q}_{x,ref}$	0	10	10	m/s ²
${}^g \ddot{q}_{y,ref}$	0	10	5.75	m/s ²
${}^g \ddot{q}_{z,ref}$	1	0	0	m/s ²
${}^g \dddot{q}_{x,ref}$	0	1000	1000	m/s ³
${}^g \dddot{q}_{y,ref}$	0	1000	575	m/s ³
${}^g \dddot{q}_{z,ref}$	1000	0	0	m/s ³

Chapter 6

Conclusions and recommendations

Control aspects, and the design aspects for controllability, of ironless long-stroke planar actuators with moving magnets and integrated active magnetic bearing have been investigated in this thesis. The combined research in electromechanical design and control presented in [17] and this thesis has resulted in a solid fundament to the electromagnetic analysis, model based commutation and design of this type of actuators. Moreover, the research has resulted in a fully operational and successfully tested prototype, the Herringbone Pattern Planar Actuator (HPPA).

6.1 Model based commutation algorithm

A novel commutation strategy, called direct wrench-current decoupling, has been presented in this thesis. Using the derived commutation algorithms it is possible to decouple both the force as well as the torque components of an ironless moving-magnet planar actuator. Moreover, the commutation algorithm also allows for smooth switching of active coil sets without influencing the decoupling, because only the coils that are underneath or near the edge of the magnet array effectively contribute to the magnetic bearing and propulsion of the translator. The commutation algorithm is decomposed into force and torque components where one of the force components has similarities with the traditional $dq0$ or Park's transformation linking the new theory to the traditional one.

6.2 Linking control to the design proces

Using the condition number of the direct wrench-current decoupling it is possible to verify whether or not a stator coil topology is state-controllable in a given position of the translator. Moreover, additional conditions have been derived which allow for the design/verification of controllable stator coil topologies with the capability of an infinite stroke in the xy -plane using smooth switching functions.

The currents resulting in a force distribution, which is optimal with respect to the minimal ohmic losses when ignoring the disturbance torque, can be calculated for a given stator coil topology. Moreover, an expression of the stator coil currents can be calculated which can be used to correct the optimal force distribution in such a way that the disturbance torque is canceled in an optimal way with respect to the ohmic losses. These currents do not contribute to the netto force on the translator. Therefore, keeping the power dissipation caused by this second term as small as possible is an important performance criteria for the actuator.

Given an ironless planar moving-magnet actuator, using the derived commutation strategy, it is possible to calculate the direction and amplitude of the smallest worst-case acceleration vector in the xy -plane, over the entire set of admissible x -, y - and z -positions, which results in one or more of the stator coil currents reaching the maximum amplifier current constraint.

6.3 Realization and test of the prototype

A prototype of an ironless moving-magnet planar actuator with integrated magnetic bearing called the "herringbone pattern planar actuator" (HPPA) has been realized and tested successfully. The translator can be levitated at standstill with a position error and an angle error of $< 0.5\mu\text{m}$ and $< 4\mu\text{rad}$, respectively. The tracking errors at high-speed motion profiles, using a maximum test speed of 1.4m/s and an acceleration of 14m/s^2 , are $< 30\mu\text{m}$ for the position error and $< 0.1\text{mrad}$ for the angle error.

Currently, the measurement system is most likely to be the limiting factor in the performance of the HPPA prototype. Parasitic effects due to the dynamic coupling between the measurement frame and the HPPA make it hard to separate the real dynamics of the HPPA from the dynamics of the measurement frame. In order to further investigate the prototype, it is advisable to remove it from the H-drive and install a measurement system which measures the position and orientation of the translator directly.

6.4 Outlook towards future developments

6.4.1 Full rotation about the z -axis

The derived commutation algorithm is not necessarily limited to long-stroke xy -movement. The fundamentally limited stroke in the z -direction results in a limited rotation about the x - and y -axis because an increasing clearance between the stator coils and the magnet array results in less force. However, extension of the actuator design and commutation algorithms to include full rotation about the z -axis could increase the functionality of planar actuators. Finding and validating controllable topologies which allow for this increased functionality is challenging because of the variable pole-pitch during rotation and the increased model complexity.

6.4.2 Planar actuators with non-holonomic constraints

There could be applications for which the accuracy during planar movement is not necessarily desired over the full xy -range. Moreover, when transportation from one section of accurate positioning to another section of accurate positioning is desired, reduction of the number of coils can probably be obtained by allowing for non-holonomic constraints on the system in the transportation area. Using these constraints only a finite set of trajectories is controllable in the transportation area. An example could be to accelerate the translator to a speed which is high enough to reach the destination area without the need for instantaneous 6-DOF decoupling (and low power consumption) of the degrees of freedom in all positions of the transportation area.

6.4.3 Fault tolerant planar actuator commutation

The commutation algorithm can be adapted to become fault-tolerant when it is possible to detect which coils are not working properly anymore. These coils should be penalized in the decoupling. As long as the rank of the decoupling does not drop due to the decreased number of active coils the system will still be operational, although the performance will decrease slightly because the currents in the remaining coils will increase.

6.4.4 Wireless power transfer, data communication and control

The advantage of a moving-magnet planar actuator over a moving-coil planar actuator is the absence of cables. With a contactless energy supply and wireless com-

munication, a manipulator on top of the translator of the planar actuator could be controlled while maintaining a contactless system. Information of the sensors can be communicated through radio, optical or inductive links. A robust control strategy of the stacked drives has to be derived which can deal with the influences of wireless interfacing in an optimal way (e.g. communication delays and data-loss).

A project has already been started to investigate and demonstrate a planar actuator with a manipulator, which has a contactless energy supply and wireless data communication and control [20, 14].

6.4.5 Multiple translators above one stator

The realized planar actuator consists of one stator and one translator. With an appropriate measurement system, also multiple translators can be levitated above a single stator. Because cables to the translator are not required, there is also no risk of cables being tangled.

Appendix A

Schur complement

Let A be a square partitioned matrix

$$A \equiv \begin{bmatrix} A_{11} & A_{12} \\ A_{21} & A_{22} \end{bmatrix}, \quad (\text{A.1})$$

with A_{11} and A_{22} also square. When A_{11} is nonsingular, A has the following decomposition

$$\begin{bmatrix} A_{11} & A_{12} \\ A_{21} & A_{22} \end{bmatrix} = \begin{bmatrix} I & 0 \\ A_{21}A_{11}^{-1} & I \end{bmatrix} \begin{bmatrix} A_{11} & 0 \\ 0 & S \end{bmatrix} \begin{bmatrix} I & A_{11}^{-1}A_{12} \\ 0 & I \end{bmatrix}, \quad (\text{A.2})$$

with the Schur complement matrix [16] S equal to

$$S \equiv A_{22} - A_{21}A_{11}^{-1}A_{12}, \quad (\text{A.3})$$

where A is nonsingular iff S is nonsingular. If A is nonsingular

$$\begin{aligned} \begin{bmatrix} A_{11} & A_{12} \\ A_{21} & A_{22} \end{bmatrix}^{-1} &= \left(\begin{bmatrix} I & 0 \\ A_{21}A_{11}^{-1} & I \end{bmatrix} \begin{bmatrix} A_{11} & 0 \\ 0 & S \end{bmatrix} \begin{bmatrix} I & A_{11}^{-1}A_{12} \\ 0 & I \end{bmatrix} \right)^{-1} \\ &= \begin{bmatrix} I & -A_{11}^{-1}A_{12} \\ 0 & I \end{bmatrix} \begin{bmatrix} A_{11}^{-1} & 0 \\ 0 & S^{-1} \end{bmatrix} \begin{bmatrix} I & 0 \\ -A_{21}A_{11}^{-1} & I \end{bmatrix} \\ &= \begin{bmatrix} A_{11}^{-1} + A_{11}^{-1}A_{12}S^{-1}A_{21}A_{11}^{-1} & -A_{11}^{-1}A_{12}S^{-1} \\ -S^{-1}A_{21}A_{11}^{-1} & S^{-1} \end{bmatrix}. \end{aligned} \quad (\text{A.4})$$

Appendix B

Proof of theorem 4.7

This proof is based on the work of R.A. Horn et al. [16, section 5.8] but it has been adapted to include non-square matrices.

Let the error matrix \mathbf{E} be small enough so that $(\mathbf{A} + \mathbf{E})$ is invertible, then the error of the inverse is defined as

$$\hat{\mathbf{x}} - \vec{\mathbf{x}} = (\mathbf{A} + \mathbf{E})^{-1} (\vec{\mathbf{b}} + \vec{\mathbf{e}}) - \mathbf{A}^{-1} \vec{\mathbf{b}}, \quad (\text{B.1})$$

when the following transformation is used

$$(\mathbf{A} + \mathbf{E}) = \mathbf{A} (\mathbf{I} + \mathbf{A}^{-1} \mathbf{E}), \quad (\text{B.2})$$

then a possible estimate of the error becomes

$$\hat{\mathbf{x}} - \vec{\mathbf{x}} \approx \left((\mathbf{I} + \mathbf{A}^{-1} \mathbf{E})^{-1} \mathbf{A}^{-1} - \mathbf{A}^{-1} \right) \vec{\mathbf{b}} + (\mathbf{I} + \mathbf{A}^{-1} \mathbf{E})^{-1} \mathbf{A}^{-1} \vec{\mathbf{e}}, \quad (\text{B.3})$$

which is a good assumption if $\rho(\mathbf{A}^{-1} \mathbf{E}) \ll 1$ (where $\rho(\mathbf{A}) \equiv \max(|\lambda|)$ is the spectral radius of \mathbf{A} and λ is an eigenvalue of \mathbf{A}). Furthermore, if $\rho(\mathbf{A}^{-1} \mathbf{E}) < 1$ then $(\mathbf{I} + \mathbf{A}^{-1} \mathbf{E})^{-1}$ can be written as a power series in $\mathbf{A}^{-1} \mathbf{E}$ resulting in

$$\begin{aligned} & \left((\mathbf{I} + \mathbf{A}^{-1} \mathbf{E})^{-1} \mathbf{A}^{-1} - \mathbf{A}^{-1} \right) \vec{\mathbf{b}} + (\mathbf{I} + \mathbf{A}^{-1} \mathbf{E})^{-1} \mathbf{A}^{-1} \vec{\mathbf{e}} \\ &= \sum_{k=1}^{\infty} (-1)^k (\mathbf{A}^{-1} \mathbf{E})^k \mathbf{A}^{-1} \vec{\mathbf{b}} + \sum_{k=0}^{\infty} (-1)^k (\mathbf{A}^{-1} \mathbf{E})^k \mathbf{A}^{-1} \vec{\mathbf{e}} \\ &= \sum_{k=1}^{\infty} (-1)^k (\mathbf{A}^{-1} \mathbf{E})^k \vec{\mathbf{x}} + \sum_{k=0}^{\infty} (-1)^k (\mathbf{A}^{-1} \mathbf{E})^k \mathbf{A}^{-1} \vec{\mathbf{e}}. \end{aligned} \quad (\text{B.4})$$

Assume $\|\mathbf{A}^{-}\mathbf{E}\| < 1$ and $\vec{b} \neq \vec{0}$ then

$$\begin{aligned} & \left\| \left((\mathbf{I} + \mathbf{A}^{-}\mathbf{E})^{-1} \mathbf{A}^{-} - \mathbf{A}^{-} \right) \vec{b} + (\mathbf{I} + \mathbf{A}^{-}\mathbf{E})^{-1} \mathbf{A}^{-} \vec{e} \right\| \\ & \leq \sum_{k=1}^{\infty} \|\mathbf{A}^{-}\mathbf{E}\|^k \|x\| + \sum_{k=0}^{\infty} \|\mathbf{A}^{-}\mathbf{E}\|^k \|\mathbf{A}^{-} \vec{e}\| \\ & = \frac{\|\mathbf{A}^{-}\mathbf{E}\|}{1 - \|\mathbf{A}^{-}\mathbf{E}\|} \|\vec{x}\| + \frac{\|\mathbf{A}^{-} \vec{e}\|}{1 - \|\mathbf{A}^{-}\mathbf{E}\|} \frac{\|\mathbf{A} \vec{x}\|}{\|\vec{b}\|}, \end{aligned} \quad (\text{B.5})$$

then the relative error becomes

$$\begin{aligned} & \frac{\left\| \left((\mathbf{I} + \mathbf{A}^{-}\mathbf{E})^{-1} \mathbf{A}^{-} - \mathbf{A}^{-} \right) \vec{b} + (\mathbf{I} + \mathbf{A}^{-}\mathbf{E})^{-1} \mathbf{A}^{-} \vec{e} \right\|}{\|\vec{x}\|} \\ & \leq \frac{\|\mathbf{A}^{-}\mathbf{E}\|}{1 - \|\mathbf{A}^{-}\mathbf{E}\|} + \frac{\|\mathbf{A}^{-} \vec{e}\|}{1 - \|\mathbf{A}^{-}\mathbf{E}\|} \frac{\|\mathbf{A}\|}{\|\vec{b}\|}. \end{aligned} \quad (\text{B.6})$$

Assume that $\|\mathbf{E}\| < \frac{1}{\|\mathbf{A}^{-}\|}$ then (B.6) becomes

$$\begin{aligned} & \frac{\left\| \left((\mathbf{I} + \mathbf{A}^{-}\mathbf{E})^{-1} \mathbf{A}^{-} - \mathbf{A}^{-} \right) \vec{b} + (\mathbf{I} + \mathbf{A}^{-}\mathbf{E})^{-1} \mathbf{A}^{-} \vec{e} \right\|}{\|\vec{x}\|} \\ & \leq \frac{\|\mathbf{A}^{-}\mathbf{E}\|}{1 - \|\mathbf{A}^{-}\mathbf{E}\|} + \frac{\|\mathbf{A}^{-} \vec{e}\|}{1 - \|\mathbf{A}^{-}\mathbf{E}\|} \frac{\|\mathbf{A}\|}{\|\vec{b}\|} \\ & \leq \frac{\|\mathbf{A}^{-}\| \|\mathbf{E}\|}{1 - \|\mathbf{A}^{-}\| \|\mathbf{E}\|} + \frac{\|\mathbf{A}^{-}\| \|\mathbf{A}\| \|\vec{e}\|}{1 - \|\mathbf{A}^{-}\| \|\mathbf{E}\|} \frac{1}{\|\vec{b}\|} \\ & = \frac{\kappa_2(\mathbf{A}^{-}, \mathbf{A})}{1 - \kappa_2(\mathbf{A}^{-}, \mathbf{A}) \frac{\|\mathbf{E}\|}{\|\mathbf{A}\|}} \left(\frac{\|\mathbf{E}\|}{\|\mathbf{A}\|} + \frac{\|\vec{e}\|}{\|\vec{b}\|} \right). \end{aligned} \quad (\text{B.7})$$

Moreover, when $\|\mathbf{E}\| \ll \frac{\|\mathbf{A}\|}{\kappa_2(\mathbf{A}^{-}, \mathbf{A})}$ the following holds
 $\rho(\mathbf{A}^{-}\mathbf{E}) \leq \|\mathbf{A}^{-}\mathbf{E}\| \leq \|\mathbf{A}^{-}\| \|\mathbf{E}\| \ll 1$ and (B.7) can be rewritten into a good estimation of the upperbound on the relative error

$$\begin{aligned} & \frac{\|\hat{\vec{x}} - \vec{x}\|}{\|\vec{x}\|} \approx \frac{\left\| \left((\mathbf{I} + \mathbf{A}^{-}\mathbf{E})^{-1} \mathbf{A}^{-} - \mathbf{A}^{-} \right) \vec{b} + (\mathbf{I} + \mathbf{A}^{-}\mathbf{E})^{-1} \mathbf{A}^{-} \vec{e} \right\|}{\|\vec{x}\|} \\ & < \kappa_2(\mathbf{A}^{-}, \mathbf{A}) \left(\frac{\|\mathbf{E}\|}{\|\mathbf{A}\|} + \frac{\|\vec{e}\|}{\|\vec{b}\|} \right) \end{aligned} \quad (\text{B.8})$$

□

Appendix C

List of symbols

Symbol	Units	Quantity
$\vec{}$		Vector
\vec{q}	m,rad	Coordinate vector
q		quadrature axis
d		direct axis
\vec{i}	A	Current vector
\vec{u}	V	Voltage vector
\vec{F}	N	Force vector
\vec{T}	Nm	Torque vector
\vec{w}	N,Nm	Wrench vector consisting of force and torque components
T		Transformation matrix
Υ		Positive-definite matrix
c		Coil coordinates
m		Magnet coordinates
l		Local coil coordinates
g		General coordinates
s		Sensor coordinates
S_n		Admissible set of coordinates of a single coil n
S_{adm}		Admissible set of coordinates of a basic active coil configuration

$S_{\vec{\alpha}}$		Necessary admissible set of coordinates of a basic active coil configuration to obtain a switchable configuration
α_x, α_y		The switch counters indicating the offset along the ${}^g q_x$ -direction and ${}^g q_y$ -direction of a repeated basic active coil configuration, respectively
$\vec{\alpha}$		The switch state vector containing $[\alpha_x \ \alpha_y]^\top$
\top		Transpose
H		Conjugate transpose
Γ	$\frac{N}{A}, \frac{N_m}{A}$	Matrix containing the model of the active set of coils
Γ^-	$\frac{A}{N}, \frac{A}{N_m}$	Decoupling matrix containing the generalized inverse of the active set of coils
Γ_F^-	$\frac{A}{N}$	Decoupling matrix containing the generalized inverse of the active set of coils only using the force components
Γ_T^-	$\frac{A}{N_m}$	Decoupling matrix containing the generalized inverse of the active set of coils only using the torque components
$\Delta ({}^l \vec{q})$		Weighing matrix which is added to the decoupling to assure smooth switching
δ		one of the diagonal terms of weighing matrix $\Delta ({}^l \vec{q})$
τ	m	pole-pitch
τ_n	m	effective pole-pitch after rotation of $\pi/4$ rad of the magnet-array
t	s	time

Bibliography

- [1] M. B. Binnard, "Six degree of freedom control of planar motors," U.S. Patent Application 2003/0 085 676, May 8, 2003.
- [2] M. B. Binnard, "System and method to control planar motors," U.S. Patent 6,650,079, Nov. 18, 2003.
- [3] M. S. Branicky, V. S. Borkar, and S. K. Mitter, "A unified framework for hybrid control: Model and optimal control theory," *IEEE Trans. Automat. Contr.*, vol. 43, pp. 31–45, Jan. 1998.
- [4] J. C. Compter, "Electro-dynamic planar motor," *Precision Engineering*, vol. 28, no. 2, pp. 171–180, Apr. 2004.
- [5] J. C. Compter and P. C. M. Frissen, "Displacement device," Patent WO 01/18 944 A1, Mar. 15, 2001.
- [6] J. C. Compter, P. C. M. Frissen, and J. van Eijk, "Displacement device," Patent WO 2006/075 291 A2, Jul. 20, 2006.
- [7] B. de Kraker and D. H. van Campen, *Mechanical vibrations*. The Netherlands: Shaker, 2001.
- [8] R. E. Doherty and C. A. Nickle, "Synchronous machines - parts I and II - an extension of Blondel's two reaction theory - steady state power angle characteristics," *AIEE Trans.*, vol. 45, pp. 912–942, Jun. 1926.
- [9] R. E. Doherty and C. A. Nickle, "Synchronous machines - part III - torque angle characteristics under transient conditions," *AIEE Trans.*, vol. 46, pp. 1–18, Feb. 1927.

-
- [10] R. E. Doherty and C. A. Nickle, "Synchronous machines - part IV," *AIEE Trans.*, vol. 47, pp. 457–492, Feb. 1928.
- [11] R. E. Doherty and C. A. Nickle, "Three-phase short circuit synchronous machines - V," *AIEE Trans.*, vol. 49, pp. 700–714, Apr. 1930.
- [12] E. Durand, *Magnétostatique*. Paris, France: Masson et *C^{ie}*, 1968.
- [13] A. E. Fitzgerald, J. C Kingsley, and S. D. Umans, *Electric Machinery*, 6th ed. New York: McGraw-Hill, 2003.
- [14] M. Gajdusek, J. de Boeij, A. A. H. Damen, and P. P. J. van den Bosch, "Contactless planar actuator with manipulator - experimental setup for control," in *Proc. of the 6th international symposium on linear drives for industrial applications*, Lille, France, Sep. 2007.
- [15] A. J. Hazelton, M. B. Binnard, and J. M. Gery, "Electric motors and positioning devices having moving magnet arrays and six degrees of freedom," U.S. Patent 6,208,045, Mar. 27, 2001.
- [16] R. A. Horn and C. R. Johnson, *Matrix analysis*. Cambridge, UK: Cambridge university press, 1999.
- [17] J. W. Jansen, "Magnetically levitated planar actuator with moving magnets: electromechanical analysis and design," Ph.D. dissertation, Eindhoven University of Technology, Nov. 2007.
- [18] J. W. Jansen, E. A. Lomonova, A. J. A. Vandenput, and C. M. M. van Lierop, "Analytical model of a magnetically levitated linear actuator," in *Conference Record of the 2005 Industry Applications Conference 40th Annual Meeting*, Hong Kong, Oct. 2005, pp. 2107–2113.
- [19] J. W. Jansen, E. A. Lomonova, A. J. A. Vandenput, and C. M. M. van Lierop, "Design flow for a six degree-of-freedom planar actuator," in *Proc. of th 3rd IEEE Young Researchers Symposium in Electrical Power Engineering*, Ghent, Belgium, Apr. 2006.
- [20] J. W. Jansen, C. M. M. van Lierop, J. de Boeij, E. A. Lomonova, J. L. Duarte, and A. J. A. Vandenput, "Moving magnet multi-dof planar actuator technology with contactless energy and data transfer," in *Proc. of the 6th international symposium on linear drives for industrial applications*, Lille, France, Sep. 2007.

- [21] J. W. Jansen, C. M. M. van Lierop, and E. A. Lomonova, "Werkwijze voor het vervaardigen van een vlakke actuator alsmede een vlakke actuator aldus vervaardigd," Dutch Patent Application 1 029 246, Jun. 14, 2005.
- [22] J. W. Jansen, C. M. M. van Lierop, E. A. Lomonova, and A. J. A. Vandenput, "Moving-magnet planar actuator with integrated active magnetic bearing," in *Proc. of the ASPE 2006 annual meeting*, Monterey, California, Oct. 2006, pp. 119–122.
- [23] J. W. Jansen, C. M. M. van Lierop, E. A. Lomonova, and A. J. A. Vandenput, "Magnetically levitated planar actuator with moving magnets," in *IEEE Int. Electric Machines and Drives Conference (IEMDC'07)*, Antalya, Turkey, May 2007, pp. 272–278.
- [24] J. W. Jansen, C. M. M. van Lierop, E. A. Lomonova, and A. J. A. Vandenput, "Modeling of magnetically levitated planar actuators with moving magnets," *IEEE Trans. Magn.*, vol. 43, no. 1, pp. 15–25, Jan. 2007.
- [25] J. W. Jansen, C. M. M. van Lierop, E. A. Lomonova, and A. J. A. Vandenput, "Ironless magnetically levitated planar actuator," *J. Appl. Phys.*, in press.
- [26] J. W. Jansen, C. M. M. van Lierop, E. A. Lomonova, and A. J. A. Vandenput, "Magnetically levitated planar actuator with moving magnets," *IEEE Trans. Ind. Applicat.*, in press.
- [27] K. Kemp and S. Wurm, "EUV lithography," *Comptes Rendus Physique*, vol. 7, pp. 875–886, 2006.
- [28] W. J. Kim, "High-precision planar magnetic levitation," Ph.D. dissertation, Massachusetts Institute of Technology, 1997.
- [29] W. J. Kim, D. L. Trumper, and J. H. Lang, "Modeling and vector control of a planar magnetic levitator," *IEEE Trans. Ind. Applicat.*, vol. 34, no. 6, pp. 1254–1262, Nov./Dec. 1998.
- [30] N. Korenaga, "Alignment apparatus and exposure apparatus using the same," U.S. Patent 7,075,198, Jul. 11, 2006.
- [31] P. J. McKerrow, *Introduction to robotics*. Sydney, Australia: Addison-Wesley Publishers Ltd., 1991.
- [32] H. Nijmeijer and A. J. van der Schaft, *Nonlinear dynamical control systems*. New York: Springer, 1990.

-
- [33] R. H. Park, "Two-reaction theory of synchronous machines - generalized method of analysis - part I," *AIEE Trans.*, vol. 48, pp. 716–730, Jul. 1929.
- [34] R. H. Park, "Two-reaction theory of synchronous machines - generalized method of analysis - part II," *AIEE Trans.*, vol. 52, pp. 352–355, Jun. 1933.
- [35] *ACM Micro Service manual*, Philips EMT, Eindhoven, Netherlands, 2001.
- [36] W. Potze and P. C. M. Frissen, "Method for controlling an electric motor, control unit and electric motor," Patent WO 2006/054 243 A2, May 26, 2006.
- [37] C. R. Rao and S. K. Mitra, *Generalized inverse of matrices and its applications*. Wiley, 1971.
- [38] S. Skogestad and I. Postlethwaite, *Multivariable feedback control*. England: Wiley, 2005.
- [39] H. M. J. R. Soemers, "The design of high performance manipulators," in *Proc. of the 2001 IEEE/ASME Int. Conf. on Advanced Intelligent Mechatronics*, Como, Italy, Jul. 2001, pp. 149–152.
- [40] T. Teng, T. Ueda, S. Makinouchi, and B. Yuan, "Moving magnet type planar motor control," in *Proc. of the 1st Int. Conf. on Positioning Technology*, Hamamatsu, Japan, Jun. 2004, pp. 203–208.
- [41] T. Ueta, B. Yuan, and T. C. Teng, "Moving magnet type planar motor control," U.S. Patent Application 2003/0 102 722, Jun. 5, 2003.
- [42] C. M. M. van Lierop, J. W. Jansen, A. A. H. Damen, E. A. Lomonova, P. P. J. van den Bosch, and A. J. A. Vandenput, "Model based commutation of a long-stroke magnetically levitated linear actuator," in *Conference record of the 2006 IEEE Industry Applications Conference 41st Annual Meeting*, Tampa, Florida, Oct. 2006.
- [43] C. M. M. van Lierop, J. W. Jansen, A. A. H. Damen, E. A. Lomonova, P. P. J. van den Bosch, and A. J. A. Vandenput, "Model based commutation of a long-stroke magnetically levitated linear actuator," *IEEE Trans. Ind. Applicat.*, under review.
- [44] C. M. M. van Lierop, J. W. Jansen, A. A. H. Damen, and P. P. J. van den Bosch, "Control of multi-degree-of-freedom planar actuators," in *Proc. of the 2006 IEEE International Conference on Control Applications, CCA 2006*, Munich, Germany, Oct. 2006, pp. 2516–2521.

-
- [45] C. M. M. van Lierop, J. W. Jansen, E. A. Lomonova, A. A. H. Damen, A. J. A. Vandenput, and P. P. J. van den Bosch, "Commutation of a magnetically levitated planar actuator with moving-magnets," in *Proc. of the 6th international symposium on linear drives for industrial applications*, Lille, France, Sep. 2007.
- [46] C. M. M. van Lierop, J. W. Jansen, E. A. Lomonova, A. A. H. Damen, A. J. A. Vandenput, and P. P. J. van den Bosch, "Commutation of a magnetically levitated planar actuator with moving-magnets," *IEEJ Trans. Ind. Applicat.*, under review.

Samenvatting

Dutch abstract

Systemen met meerdere mechanische vrijheidsgraden worden vaak geconstrueerd met elektromechanische actuatoren met maar één vrijheidsgraad. Over het algemeen beschikken deze actuatoren over een standaard, vaak geïntegreerd, commutatie (d.w.z. linearisatie- en ontkoppelings-) algoritme, welke de actuator van de noodzakelijkeingangssignalen voorziet. Het toepassen van dit commutatie-algoritme resulteert bij deze machines in gemakkelijke regeleigenschappen en relatief simpele actuator begrenzingen. In sommige applicaties is het noodzakelijk om actuatoren toe te passen die meerdere vrijheidsgraden combineren om zo tegemoet te kunnen komen aan de steeds strengere eisen. Als gevolg van het integreren van vrijheidsgraden in één actuator, worden de commutatie en de regeling echter complexer. Het is daarom van het grootste belang om de regeltechniek vanaf een vroeg stadium in het ontwerpproces van deze actuatoren mee te nemen. De twee belangrijkste bijdragen van dit proefschrift zijn het beschrijven van een nieuw commutatie-algoritme, maar vooral ook het toelichten van de daaruit voortvloeiende ontwerpimplicaties.

Een magnetisch gelagerde planaire (in een vlak bewegende) actuator is een voorbeeld van een actuator waarin meerdere vrijheidsgraden gecombineerd zijn. Deze actuator kan gebruikt worden als alternatief voor xy -aandrijvingen die bestaan uit aan elkaar gekoppelde lineaire motoren. Deze aandrijvingen worden veelal toegepast in industriële hoge precisie applicaties waarbij objecten in een vlak gepositioneerd moeten worden. De planaire actuator is opgebouwd uit een stator met een aaneenschakeling van spoelen waarboven een translator met een patroon van permanente magneten zweeft. De translator, het bewegende deel, wordt hierbij slechts ondersteund door magnetische velden. Door het magnetische lager moet de translator echter actief gestabiliseerd worden in zes vrijheidsgraden. In dit proef-

schrift wordt de dynamica, de commutatie en het regelontwerp beschreven van een magnetisch gelagerde planaire actuator met bewegende magneten. Het grootste voordeel van deze actuator is dat er geen kabels nodig zijn van de vaste wereld naar de translator. Alleen de spoelen die zich onder het magneetoppervlak bevinden, kunnen een effectieve bijdrage aan de levitatie en voortstuwing van de translator leveren. Daarom wordt er afhankelijk van de positie van de translator in het xy -vlak geschakeld tussen verschillende sets van actieve spoelen. Het schakelen tussen spoelen in combinatie met de volledig contactloze translator maakt, in principe, een oneindige slag in het xy -vlak mogelijk.

Vanwege de integratie van de voortstuwing in het xy -vlak en de actieve magnetische lagering is het niet mogelijk om gebruik te maken van standaard ontkoppelstrategieën voor synchrone machines voor het ontkoppelen van de kracht- en koppelcomponenten. Vandaar dat er een nieuw commutatie-algoritme is afgeleid dat de transformatie van de kracht- en koppelcomponenten, als functie van de stromen door de spoelen en de positie en oriëntatie van het platform, invertteert. In dit proefschrift is er gekozen voor een model-gebaseerde commutatie en regel-aanpak, gebruik makend van een real-time analytisch model van de planaire actuator. Het real-time model is gebaseerd op analytische oplossingen van de Lorentz kracht- en koppelintegralen. Het nieuwe algoritme levert een optimale oplossing, in die zin dat het energieverbruik van de actuator wordt geminimaliseerd. Nog een belangrijke bijdrage in dit proefschrift is de introductie van gladde positie afhankelijke weegfuncties in het commutatie-algoritme. Deze functies resulteren in een glad schakelgedrag tussen verschillende actieve groepen van spoelen. De resulterende stroomvorm door iedere individueel aangestuurde actieve spoel is sterk niet sinusvormig.

De model-gebaseerde aanpak, in combinatie met het nieuwe commutatie-algoritme, heeft een ontwerpmethodologie opgeleverd die de regelbaarheid van planaire-actuator-topologieën opneemt in de ontwerpfase. Met behulp van deze methode worden verscheidene topologieën behandeld in dit proefschrift. Door de veranderende hoeveelheid actieve spoelen tijdens het schakelen tussen de verschillende actieve spoelgroepen, hangen de actuator begrenzingen af van de xy -positie van de translator. Dit proefschrift bevat daarom ook een analyse van de haalbare acceleratie als functie van de positie van de translator in combinatie met de begrenzing van de stroomversterkers. Verder is het dynamische gedrag van het ontkoppelde systeem geanalyseerd bij kleine fouten en is er een stabiliserende regelstructuur afgeleid.

Een van de ontwerpen van de planaire actuator, de HPPA (Herringbone Pattern Planar Actuator), is tot in meer detail uitgewerkt en is ook daadwerkelijk gebouwd. Deze actuator is vernoemd naar het spoelpatroon (gelegen in een vis-

graat patroon). De stator bestaat uit een totaal van 84 spoelen, waarvan er tussen de 15 en 24 gelijktijdig worden gebruikt voor de lagering en de voortstuwing van de translator. Het real-time model, het dynamische gedrag en het commutatie-algoritme zijn experimenteel geverifieerd met behulp van deze volledig operationele actuator. De magnetisch gelagerde, planaire actuator met zes vrijheidsgraden en bewegende magneten (de HPPA) is ontwikkeld en getest en werkt naar behoren volgens alle vooraf gestelde ontwerp- en prestatie-eisen.

Dankwoord

Acknowledgements

Tijdens het afronden van dit proefschrift is het schrijven van een dankwoord een prettige afleiding. Een project zoals dit staat of valt met een goede samenwerking. Vandaar dat ik als eerste mijn collega Helm Jansen wil bedanken voor de prettige samenwerking van de afgelopen vier jaar. Je gedrevenheid om dit project tot een goed einde te brengen, ook als het wel eens tegen zat, was een belangrijke motivatie voor mij om hetzelfde te doen. Ook ik had mij geen betere project partner kunnen wensen [17].

Natuurlijk wil ik ook mijn vriendin Chantal bedanken voor het vele geduld dat ze heeft moeten uitoefenen tijdens het afronden van mijn proefschrift. Je bent mijn rots in de branding. Ik ben erg blij met wat we, ondanks de turbulente periode, het afgelopen jaar samen hebben bereikt.

Mijn familie heeft er de afgelopen vier jaar voor gezorgd dat er genoeg rust was in mijn privé situatie om ongestoord te kunnen werken. Els, John en Willem: Bedankt dat ik altijd bij jullie aan kon kloppen als er iets was waar ik mee zat. Hoewel het vele klussen aan het huis veel tijd en energie in beslag heeft genomen was het een aangename afwisseling ten opzichte van mijn taken als promovendus. In relatie tot mijn proefschrift wil ik mijn vader en Maarten van Dijk bedanken voor het ontwerpen van de mooie kaften.

Verder wil ik Paul van den Bosch, Ad Damen, André Vandenput en Elena Lomonova bedanken voor de vrijheid en het vertrouwen in de afgelopen periode. Jullie enthousiasme met betrekking tot dit project heeft het mogelijk gemaakt om binnen de gestelde periode een werkend prototype af te kunnen leveren.

Mijn commissieleden, Hans Butler, John Compter en Okko Bosgra wil ik bedanken voor het lezen van mijn proefschrift en de daaropvolgende discussies. Ook wil ik Michel Antal bedanken voor het zitting nemen in mijn commissie, het goed-

keuren van mijn publicaties, en zijn inzet voor IOP-EMVT.

Het succesvol realiseren van een werkend prototype was nooit gelukt zonder de inzet van diverse mensen. In het bijzonder wil ik daarom Marijn Uyt de Willigen bedanken voor de vele uren die hij heeft gestoken in het realiseren van een veilige en betrouwbare opstelling (en het aanhoren van onze verhalen). Ook wil ik Will Hendrix, Udo Bartzke en Ab Schrader bedanken voor hun inzet bij het implementeren van de regelopstelling en de protocollen. Een groot aantal componenten moest speciaal voor deze opstelling worden ontwikkeld. De gemeenschappelijke technische dienst (GTD) van de technische universiteit Eindhoven heeft een onmisbare bijdrage geleverd aan de ontwikkeling en de assemblage van de mechanica. Vooral dankzij de inzet en flexibiliteit van Jovita Moerel en Patrick de Laat is de samenwerking met de GTD soepel en succesvol verlopen. Vanuit het bedrijfsleven wil ik Korneel Wijnands (Prodrive), Mark van den Broek (Vacuumschmelze), Peter Krechting (Tecnotion), Ad Vermeer (Assembléon) en Peter van Gils (ASML) bedanken voor hun inzet.

Verder zijn er nog een aantal stagiaires en afstudeerders die een bijdrage hebben geleverd aan de opstelling. Hiervan wil ik in het bijzonder, Angelino Eijgermans, Justin van Essen, Jan Schellekens en Jochem Vissers bedanken.

Natuurlijk zijn er ook vele collega's die ik wil bedanken. Allereerst wil ik natuurlijk mijn altijd aanwezige kamergenoot Andrej Jokic bedanken voor de vele leuke gesprekken. Dankzij jou viel het gelukkig een stuk minder op dat ik ook behoorlijk chaotisch ben. Ik hoop alleen wel dat we vanaf nu iets minder vaak op kantoor te vinden zijn. Graag wil ik langs deze weg ook mijn collega promovendi, Aleksandar, Anton, Bart, Femke, Hans, Heico, Jasper, Jeroen, John, Juraj, Laurentiu, Leo, Maarten, Mark, Michal, Michiel, Mircea, Patricia, Patrick, Paul en Satya bedanken. In het bijzonder wil ik Mark en Maarten bedanken voor de leuke tijd die we hebben gehad tijdens conferenties, John voor de discussies over het bouwen van huizen en Mircea voor de ondertitel van dit proefschrift. Mijn collega paranimf en bijna kamergenoot Paul wil ik bedanken voor de leuke tijd en het ongewild bijwonen van de discussies tussen Helm en mij. Siep Weiland wil ik bedanken voor zijn wiskundig advies. Natuurlijk wil ik ook Barbara bedanken voor de leuke uitjes en voor de hulp bij al mijn financiële, organisatorische en administratieve problemen.

Ook wil ik langs deze weg al mijn vrienden, die ik de afgelopen tijd heb moeten verwaarlozen, bedanken. Jullie gaan weer meer van mij horen.

Een raar fenomeen is dat het meest toegankelijke en over het algemeen meest gelezen deel, namelijk het dankwoord, vaak opgenomen wordt aan het eind van een proefschrift. Tot slot wil ik dus alle mensen bedanken die de moeite hebben genomen om dit deel van mijn proefschrift te bereiken door bij de titelpagina te beginnen en het proefschrift van voor tot achter door te lezen.

Curriculum Vitae

Nelis van Lierop was born in Eindhoven, the Netherlands, on the 11th of March in 1978. He attended secondary school at the Pastoor Aelen-mavo (MAVO) in Eersel from 1992 until 1994 and at the Rythovius College (HAVO) in Eersel from 1994 until 1996. During this period he received the third price at the "Nationale wedstrijd voor jonge onderzoekers" (a national, Dutch, contest for young researchers).

He then started studying electrical engineering in Eindhoven at the Fontys Hogescholen (HTS) in 1996. His internship at the physics department of the Eindhoven University of Technology comprised of the design of a modulator for a linear micro-bunch particle accelerator. His graduation project took place at Philips Lighting and concerned the design of a dual output power converter for a light application. He received his B.Sc.-degree in electrical engineering in 2000.

In 2000, he started studying electrical engineering at the Eindhoven University of technology. His graduation project within the control systems group took place at the physics department of the same university, and concerned "The influence of amplitude and phase variations on a resonant cavity". The research comprised of the analysis of the effect of amplitude and phase variations on the output power of a linear particle accelerator. The results of this analysis and the designed modulator (during his internship) have been successfully applied to several accelerators. He received his (Cum Laude) M.Sc.-degree in electrical engineering in 2003.

From October 2003 to Januari 2008, he pursued his Ph.D. degree in the control systems group of the department of electrical engineering at the Eindhoven University of Technology. The topic of his Ph.D. research was a "Magnetically Levitated Planar Actuator with Moving Magnets" where he focussed on the "Dynamics, Commutation and Control Design". During his Ph.D. research he also received the course certificate of the Dutch Institute of Systems and Control DISC for completing a required number of postgraduate courses.

Nelis' personal interests are art and listening to, performing and composing (piano) music. He played in several bands (e.g. GuessStation and In-Tension).